

**Planar optics with wavelength-scale
high contrast gratings**

Annett Birgit Fischer

PhD

University of York

Physics

March 2015

Für meine Familie

Abstract

In recent years, the emergence of a new type of sub-wavelength dielectric grating with a high refractive index contrast, typically referred to as high contrast grating, and its simple fabrication procedure have given rise to numerous applications in integrated photonics and optoelectronics. The on-going demand for miniaturised planar devices in the near-infrared spectral range and the compatibility with standard processing techniques motivated us to explore the intriguing resonance effects in high contrast gratings for the application as broadband mirrors, reflective lenses, and as part of static and tuneable Fabry-Pérot cavities.

We chose amorphous silicon as the high refractive index material. The characteristics of grating mirrors were analysed numerically and measured experimentally, confirming their suitability for use as focussing reflectors and cavity mirrors in a Fabry-Pérot interferometer. As a result, a new type of reflective diffractive lens incorporating multiple phase jumps was designed, fabricated, and experimentally tested, and showed improved performance in terms of numerical aperture compared to other devices in the literature. Furthermore, initial experiments by integrating arrays of such lenses with a microfluidic platform showed an application potential in the area of large-scale optical trapping. In an attempt to develop functional wavelength-selective filters utilising high contrast gratings and microelectromechanical systems, we investigated static cavities based on metals and gratings, which included simulation, development of the fabrication process, and optical characterisation. Following these proof-of-principle studies and the computational analysis of the mechanical behaviour of flexible membrane designs, the challenge in making tuneable devices was to fabricate a fully working tuneable filter and its characterisation.

Overall, this thesis contributes to the field of integrated and planar silicon photonics by addressing the design and the performance aspects of high contrast grating lenses with high numerical aperture as well as addressing key challenges in the fabrication of tuneable filters.

Contents

Abstract	V
List of figures	XI
List of tables	XVII
Acknowledgements	XIX
Author's declaration	XXI
1 Introduction	1
1.1 Motivation	1
1.2 Thesis objectives	3
1.3 Thesis organisation	5
2 Theory and state-of-the-art	7
2.1 Wavelength-scale high contrast gratings	7
2.1.1 Diffraction theory	7
2.1.2 Guided-mode resonances in wavelength-scale high contrast gratings	9
2.1.3 Rigorous coupled-wave analysis	13
2.2 Beam shaping in microoptics	18
2.2.1 General overview of microlenses	18
2.2.2 Beam shaping with diffractive microstructures	20
2.3 Wavelength-selective Fabry-Pérot filters	22
2.3.1 Fabry-Pérot resonator	22
2.3.2 State-of-the-art tuneable optical Fabry-Pérot filters	26
3 Fabrication methods	31
3.1 Material choice	31
3.1.1 Deposition methods of amorphous silicon	31
3.1.2 Silicon nitride membrane	33
3.2 Pre-treatment of sample	34

3.3	Lithography	35
3.4	Lift-off and electron-beam evaporation of metals	39
3.5	Spacer definition and adhesive bonding	40
3.6	Microfluidic channels using PDMS	41
4	Broadband grating reflector	45
4.1	Material	45
4.1.1	PECVD amorphous silicon on glass substrate (sample 1)	46
4.1.2	Sputtered amorphous silicon on silicon nitride (sample 2)	49
4.2	Fabrication of broadband mirrors	51
4.3	Characterisation of broadband mirrors	52
4.3.1	Reflectivity measurement of sample 1	52
4.3.2	Reflectivity measurement of sample 2	54
4.4	Summary	56
5	Planar diffractive lens with high numerical aperture	59
5.1	Design of high contrast grating lenses	59
5.1.1	Key criteria	60
5.1.2	Sample system and methodology	61
5.1.3	Influence of grating thickness	68
5.1.4	Investigation of numerical apertures and microlens arrays	70
5.2	Fabrication of high contrast grating lenses	71
5.2.1	General aspects	71
5.2.2	Grating lens arrays with high numerical aperture	74
5.2.3	Integrated microfluidic	75
5.3	Characterisation of high contrast grating lenses	76
5.3.1	Wavelength dependence	76
5.3.2	Angle dependence	78
5.3.3	Beam profile of the diffractive lens	80
5.3.4	Scan of different numerical apertures	84
5.3.5	Grating lens arrays with high numerical aperture for optical trapping	85
5.4	Summary	88
6	Static Fabry-Pérot filter based on high contrast gratings	91
6.1	Design of static FP filters	91
6.2	Fabrication of static FP filters	94
6.3	Characterisation of static FP filters	96
6.3.1	Metal-based Fabry-Pérot filter with polymer-filled cavity	97

6.3.2	Metal-based Fabry-Pérot filter with air-filled cavity	99
6.3.3	Grating-based Fabry-Pérot filter with air-filled cavity	100
6.4	Summary	103
7	Tuneable MEMS Fabry-Pérot filter based on high contrast gratings	105
7.1	Concept and simulation of tuneable MEMS FP filters	105
7.1.1	Design considerations	106
7.1.2	Membrane suspension designs and stress modelling	108
7.2	Fabrication details for tuneable MEMS FP filters	112
7.2.1	Silicon nitride membrane	113
7.2.2	Process flow for a tuneable MEMS FP filter	115
7.3	Characterisation of tuneable MEMS FP filters	119
7.3.1	Metal-based MEMS FP filter	120
7.3.2	Hybrid metal-grating-based MEMS FP filter	122
7.4	Summary	124
8	Conclusions and application perspectives	127
8.1	Overview of results	127
8.2	Application perspectives	131
	List of abbreviations	135
	Bibliography	137

List of figures

1.1	Optical absorption of water and absorption of deoxygenised haemoglobin with indication of the therapeutic window.	3
2.1	Incidence of a plane wave on a one-dimensionally periodic diffraction grating.	8
2.2	Schematic illustrations of the geometry of a 1D grating for the diffraction and for the near-wavelength regime.	10
2.3	A fraction of the infinitely periodic and asymmetric 1D grating geometry considered in this work and a sketch of the discretisation of the unit cell in RCWA.	14
2.4	Examples of a broadband mirror and a transmission filter for silicon-based sub-wavelength gratings.	17
2.5	Cross-sectional profiles of typical converging lenses with a ray picture of the plane waves incident from the bottom and combining at the focal spot at the top.	19
2.6	Typical half shapes of lenses with a quadratic phase relation and two phase jumps shown.	21
2.7	Geometry of a Fabry-Pérot interferometer with typical transmission characteristics for five different mirror reflectivities.	23
2.8	Several tuning mechanisms to alter the resonance condition of a Fabry-Pérot interferometer.	27
3.1	Optical constants for c-Si, sputtered a-Si, and PECVD a-Si.	32
3.2	SEM and optical images of uncoated and a-Si coated silicon nitride membranes.	34
3.3	Processing steps during lithography and pattern transfer.	36
3.4	Process flow during lift-off.	40
3.5	Process flow for making microfluidic channels on a functional sample using soft-lithography.	42

4.1	Grating geometry and parameters used in the RCWA simulation for PECVD a-Si on glass. The broadband responses in reflection are compared by taking into account the dispersion only and both the dispersion and the absorption of PECVD a-Si.	47
4.2	A parameter scan for PECVD a-Si on glass using RCWA.	48
4.3	Grating geometry and parameter scan for sputtered a-Si on silicon nitride membrane using RCWA.	50
4.4	Scanning electron micrographs of the fabricated mirrors.	52
4.5	Reflection setup at Tyndall.	53
4.6	Measurement and simulation of the reflectivity spectra of PECVD a-Si gratings on glass for TM and for TE polarisation.	54
4.7	In-house reflection setup.	55
4.8	Measured and simulated reflectivity of a sputtered a-Si HCG on a silicon nitride membrane for TM polarisation.	56
5.1	RCWA maps of the magnitude and the phase of the reflection coefficient as function of the period and duty cycle of an a-Si grating with the calculated paths.	64
5.2	Parabolic phase profile along the central horizontal axis of an HCG lens with $f = 100 \mu\text{m}$ and $D = 80 \mu\text{m}$	65
5.3	Quarter view of a non-periodic HCG lens with $f = 100 \mu\text{m}$ and $D = 80 \mu\text{m}$ and full design of the lens with the corresponding phase distribution shown in the right half.	66
5.4	3D FEM simulation of an HCG with a parabolic phase profile, a focal length of $f = 5 \mu\text{m}$, and diameter $D = 8 \mu\text{m}$ for an operating wavelength of 980 nm and TM polarisation.	67
5.5	Distribution of reflectivity, period, and duty cycle over the parabolic phase path calculated for a grating thickness of 300 nm.	69
5.6	Influence of the grating thickness on the average reflectivity and the length of the calculated path.	69
5.7	Original design, proximity-corrected exposure pattern, and SEM image of a quarter of a spherical lens design with $f = 140 \mu\text{m}$ and $D = 18 \mu\text{m}$	72
5.8	Fabricated reflective grating lens with parabolic phase profile, a focal length of $100 \mu\text{m}$, and $D = 80 \mu\text{m}$ for five different exposure doses.	73
5.9	Scanning electron micrographs of fabricated focussing reflectors.	74
5.10	Optical micrograph of fabricated HCG lenses with different numerical aperture values.	75

5.11	A water-tight PDMS frame and an integrated microfluidic channel on a sample containing HCG lens arrays.	76
5.12	Influence of operating wavelength on a grating lens with focal length of $60 \mu\text{m}$ and NA of 0.64 and reflection measurements of an HCG lens with $f = 100 \mu\text{m}$ and $D = 80 \mu\text{m}$ at both orthogonal polarisations. . .	77
5.13	Influence of angle of incidence on the focussing performance.	79
5.14	Experimental setup for the characterisation of the HCG lenses.	81
5.15	Lateral intensity profiles of a reflective HCG lens with a cylindrical phase profile and with a spherical phase profile.	82
5.16	Measured beam profile of a reflective HCG lens with $f=100 \mu\text{m}$, $D=80 \mu\text{m}$, and a parabolic phase profile.	83
5.17	Measured intensity profiles of the reflected and transmitted spots for the lens in Figure 5.16.	84
5.18	Comparison between measured and calculated numerical apertures for different fabricated grating lenses.	85
5.19	Schematic sketch of the optical trapping setup at St Andrews to test the performance of flat reflective HCG lens arrays.	86
5.20	Focussing image of the lens array measured with a fibre laser at 1064 nm , TM polarisation, normal incidence, and SEM images with deteriorated lens shapes.	87
5.21	Close-up view of a lens with designed NA of 0.7, but keeping the design period equal throughout the structure.	87
6.1	Plot of the reflection, transmission, and absorption as function of the film thickness of gold deposited on a glass substrate.	92
6.2	Schematics of different FP filter geometries and their responses using RCWA for cavity lengths of $10 \mu\text{m}$ and TM-polarised plane-wave incidence.	93
6.3	Influence of a 5-nm layer of chromium between gold and glass substrate on the FP response.	94
6.4	Workflow of fabrication of a static FP filter based on either metal reflectors or a-Si HCG reflectors.	95
6.5	Transmission setup for characterising the resonances of a Fabry-Pérot filter.	96
6.6	Measured transmittance and calculated response by RCWA and analytical FP theory of a fabricated FPI consisting of a cavity filled with the polymer SU-8 and two gold reflectors on glass substrates. . .	97

6.7	Measured transmittance and calculated response by RCWA and analytical FP theory of a fabricated FPI consisting of an air-filled cavity and two gold reflectors on glass substrates.	99
6.8	Measured and calculated transmittances of a FP filter consisting of an air-filled cavity and two periodic grating mirrors based on evaporated amorphous silicon on glass substrate.	100
6.9	Images of two grating reflectors based on PECVD amorphous silicon on glass substrates prior adhesive bonding and their measured and calculated transmittances after bonding.	102
7.1	Layout and photograph of the silicon nitride membrane samples purchased from Norcada Inc.	107
7.2	Schematics of the tuneable MEMS FP filters produced in this work. Left: Metal-based filter. Right: Hybrid metal-grating filter.	108
7.3	FEM simulation procedure of a silicon nitride membrane with four anchoring arms.	110
7.4	FEM simulation results of six different membrane suspension designs for a silicon nitride membrane with a thickness of 100 nm.	111
7.5	Membrane deflection across the central area of all six simulated designs along x axis and y axis.	111
7.6	Scanning electron micrographs of differently etched anchor designs of the membrane.	114
7.7	Released membrane suspension exhibiting cracks at the corners of the design and improved design with rounded corners.	115
7.8	Workflow for fabrication of a tuneable MEMS FP filter based on a-Si high contrast gratings and metal reflector on a silicon nitride membrane.	116
7.9	Optical micrographs during fabrication of the tuneable hybrid metal-grating-based MEMS filter.	118
7.10	Final assembly of a fabricated metal-based tuneable MEMS FP filter with FP response and tuning behaviour.	120
7.11	Optical image of the gold-coated silicon nitride membrane and static analysis of the flatness of the processed membrane.	121
7.12	Dynamic analysis of the FP filter containing the gold-coated silicon nitride membrane.	122
7.13	Measured and calculated transmittances of a MEMS filter incorporating a gold-coated silicon nitride membrane and a periodic HCG on a glass substrate optimised for broadband reflection around $1 \mu\text{m}$	123

8.1	Summary of the results with reference to the corresponding thesis chapters.	128
8.2	Possible applications for high contrast grating lenses.	132

List of tables

3.1	Overview of the resists and the fabrication recipes used.	38
3.2	Parameters for dry etching amorphous silicon and silicon nitride. . . .	39
5.1	Formulae and visualisations of the phase profile for typical flat and curved mirrors.	63
6.1	Summary of all fabricated static Fabry-Pérot filter types.	103
7.1	Summary of the results of the tuneable MEMS filters attained in this project.	125

Acknowledgements

I commenced my PhD research at the School of Physics & Astronomy in the University of St Andrews and conducted the second half of my studies at the Department of Physics in the University of York - I would like to express my gratitude to many people in both places, who have contributed to the success of this work.

In the first place, I would like to thank my supervisor Prof. Thomas F. Krauss for giving me the opportunity to be part of his research group, for his continuous support and guidance as well as for helpful suggestions and discussions throughout the whole of my PhD. His enormous experience and lively, motivating, and positive attitude have to a large extent influenced both my professional and personal development. A very special thanks to Dr William Whelan-Curtin (Liam O'Faolain) for his role as a day-to-day supervisor and his invaluable support in the first half of my PhD, for teaching me most of the fabrication processing, and for all the advice he has given to me. Also, I thank Dr Christopher Reardon and Dr Emiliano R. Martins for innumerable suggestions for my work and for being great colleagues since my time as a master student in St Andrews. Particularly in York, a special thank goes to my colleague Daan Stellinga for the constructive collaboration, the composition of the numerical code, and his help with theoretical aspects on the grating lens project. Overall, a big thank you to my friends and former colleagues from the University of St Andrews and the members of the Photonics group at York for the support and the friendly atmosphere both on and off the work. My special thanks to my colleagues at St Andrews for the opportunity to continue my fabrication during the relocation period while always having the support of the cleanroom technicians Steve Balfour, Callum Smith, and George Robb. I also thank Kishan Dholakia's research group for the collaborative efforts. I also would like to thank all staff of the workshop, electronics, and stores in both universities for their help.

I would like to thank our collaborators at Tyndall National Institute in Cork, Ireland, in particular to Dr Liam Lewis, Dr Steve Hegarty, Dr Tomasz Piwonski, for providing many silicon samples, assistance in measurements during my secondment visit in Cork, and helpful discussions. Thanks also go to Dr Maria Miritello for the sputtering of amorphous silicon and to researchers at the University of Pavia, Italy,

and to Dr Yue Wang for the refractive index modelling. Furthermore, I would like to thank Prof. Heidi Ottevaere and Dr Deborah O'Connell for agreeing to examine my work.

I am thankful for my funding from the European Union under the PROPHET project, which not only provided me with the financial support, but also with a wide range of multi-disciplinary skills obtained during regular workshops at interesting places within Europe.

On a more personal note, I thank all my friends, who supported and encouraged me on my way through the PhD. I would like to say my heartfelt thanks to my parents and my brother for their continuous support throughout my PhD. Finally, I am deeply indebted to my husband Matthias for his endless love, his never ceasing support, and belief in me at all times.

Author's declaration

I, Annett B. Fischer, declare that this thesis is a presentation of original work and I am the sole author. This work has not previously been presented for an award at this, or any other, University. All sources are acknowledged as References. Selected material from this thesis has been published in peer-reviewed journals and presented at conferences and workshops, detailed in the appendix, and listed below:

Wang, Y., Stellinga, D., **Klemm, A. B.**, Reardon, C. P., and Krauss, T. F. (2014). Tunable optical filters based on silicon nitride high contrast gratings. *Journal of Selected Topics in Quantum Electronics*, 21(4):2700706. DOI: 10.1109/JSTQE.2014.2377656

Klemm, A. B., Stellinga, D., Martins, E. R., Lewis, L., O'Faolain, L., and Krauss, T. F. (2014). Focusing with planar microlenses made of two-dimensionally varying high contrast gratings. *Optical Engineering*, 53(9):095104-1-095104-6. DOI: 10.1117/1.OE.53.9.095104

Klemm, A. B., Stellinga, D., Martins, E. R., Lewis, Huyet, G., L., O'Faolain, L., and Krauss, T. F. (2013). Experimental high numerical aperture focusing with high contrast gratings. *Optics Letters*, 38(17):3410-3413. DOI: 10.1364/OL.38.003410

Klemm, A. B., Stellinga, D., Martins, E. R., Lewis, L., O'Faolain, L., and Krauss, T. F. (2014). Characterization of planar microlenses based on high contrast gratings. *SPIE Photonics West, OPTO*, San Francisco, USA, 1-6 February. - Invited talk.

Klemm, A. B., Stellinga, D., Martins, E. R., Lewis, L., Huyet, G., O'Faolain, L., and Krauss, T. F. (2013). Optical focus with high aperture lens based on high contrast gratings. *18th Microoptics Conference (MOC'13)*, Tokyo, Japan, 27-30 October. - Contributed talk.

Klemm, A. B., Stellinga, D., Martins, E. R., Lewis, L., Huyet, G., O'Faolain, L., and Krauss, T. F. (2013). Focussing with high aperture lens based on high contrast gratings. *International Nano-Optoelectronics Workshop 2013 (iNOW)*, Cargèse, France, 19-30 August. - Poster presentation with first prize won.

1 Introduction

1.1 Motivation

Optical phenomena associated with diffraction gratings have attracted scientists since the first documentation of the occurrence of diffraction orders in 1786 [Hopkinson and Rittenhouse, 1786]. The understanding of the diffraction behaviour in terms of the wave propagation in these periodic structures has since been studied extensively to analyse the spectrum of light. Furthermore, the advances in computers, lasers, and communications technology have enabled numerous applications in which diffraction gratings are the key optical element, e.g., in optical interconnect systems [Harris et al., 1972, Katzir et al., 1977], optical sensing [Suhara et al., 1995, Ura et al., 1994], and fibre optical communications [Breer and Buse, 1998, Meltz et al., 1989, Rakuljic and Leyva, 1993]. A key material, especially during more recent developments, has been silicon due to its high refractive index and low loss in the near-infrared and telecommunication band. The use of silicon as a photonic material was mainly driven by the optical communications sector and the integrated circuit industry. In particular, a great deal of research interest has been directed at periodic structures with feature sizes smaller or close to the incident wavelength, as they offer a way to generate an artificial material with controllable optical properties. This has led to the introduction of the concept of photonic crystals in the late 1980's [Yablonovitch, 1987], the notion of the guided-mode resonance effect in sub-wavelength gratings [Hessel and Oliner, 1965, Wang et al., 1990], and the establishment of powerful electromagnetic design tools (rigorous coupled-wave analysis [Moharam and Gaylord, 1981] and modal approaches [Chu and Kong, 1977, Li, 1993, Peng et al., 1975]) to describe and obtain the full and effective control of light. Driven by highly sophisticated fabrication methods, new related fields have emerged, such as nano- and microphotronics, silicon photonics, integrated optics, binary and planar optics. The key advantages of these fields are a reduction in size, weight, and cost in conjunction with an improved system performance compared to bulk optical setups. As a result, a variety of interesting optical devices based on the guided-mode resonance effect have been demonstrated

experimentally and still present an active field of research to date. Among these are anti-reflection coatings [Motamedi et al., 1992, Raguin and Morris, 1993, Wilson and Hutley, 1982], narrowband filters [Brundrett et al., 1998, Hernandez et al., 2007], polarisers [Poutous et al., 2010], wave plates [Mutlu et al., 2012a], broadband reflectors [Mateus et al., 2004, Ricciardi et al., 2010, Yang et al., 2012b], focussing lenses [Fattal et al., 2010, Lu et al., 2010], and other diffractive optical elements [Genevet et al., 2012, Kikuta et al., 2003, Reader-Harris et al., 2013].

Amongst these developments, a class of devices based on sub-wavelength gratings made of high refractive index materials has emerged, which are referred to as wavelength-scale high contrast gratings. Their intriguing features, such as broadband reflectivity close to 100% and the ability to focus light by imparting a deterministic phase profile across the structure have been analysed in great detail [Chang-Hasnain and Yang, 2012, Karagodsky and Chang-Hasnain, 2012, Karagodsky et al., 2010b, Magnusson and Shokooch-Saremi, 2008]. While non-planar surfaces such as conventional microlenses may impede efficient integration on a micron scale, the single-layer nature of high contrast gratings, with thicknesses much smaller than half of the incident wavelength, enables us to realise optical functions on a planar substrate. Thus, they can be thought of as flat optical elements that can be fabricated in a single lithographic step and therefore offer the prospect of monolithic integration. As such, high contrast grating lenses have the potential to improve existing lens systems while eventually offering new functionalities in areas such as on-chip technologies and optical sensing.

The success of wavelength-scale high contrast gratings has also been demonstrated in compact wavelength-tuneable sources in the area of microelectromechanical systems (MEMS) [Chung et al., 2010, Zhou et al., 2008]. HCGs have been integrated in a vertical-cavity surface-emitting laser (VCSEL) to act as an outcoupling mirror. The use of an HCG, which is a lightweight planar film, significantly increases the tuning speed compared to conventional systems using distributed Bragg reflectors. Generally, MEMS-based devices have had significant commercial success (e.g., digital micromirror device (DMD) from Texas Instruments [Van Kessel et al., 1998], thin-film micromirror array (TMA) from Daewoo [Kim and Hwang, 2000], grating light valve from Silicon Light Machines [Apte et al., 1993]) and correspondingly, tuneable MEMS Fabry-Pérot (FP) filters are an active field of research, especially in telecommunications [Irmer et al., 2003, Lipson and Yeatman, 2007, Milne et al., 2009, Wu et al., 1995] and spectroscopy [Lackner et al., 2006]. In addition, there is a demand for MEMS filters in applications such

as biosensing and spectroscopy of relevant biomolecules, which usually operate at near-infrared wavelengths. The focus on the near-infrared spectral range for bio-related applications is due to the relatively low absorption of water in this wavelength range, also referred to as the “therapeutic window“ (Figure 1.1).

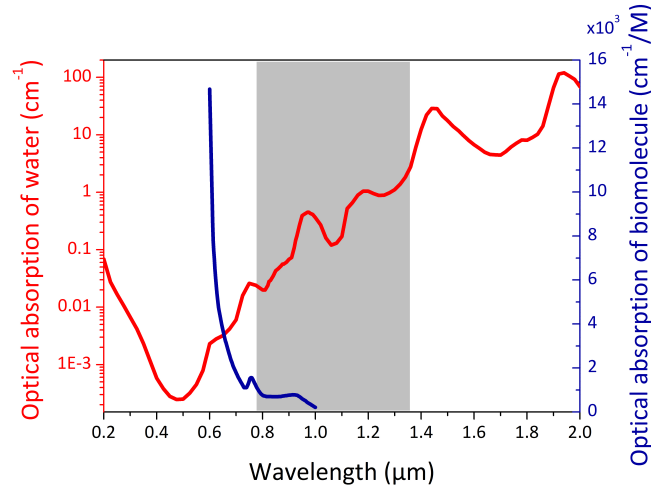


Figure 1.1: Optical absorption of water in the spectral range 200 nm - 2 μm [Hale and Querry, 1973] and absorption of a biomolecule, here deoxygenised haemoglobin [Prahl, 2002]. The grey-shaded area highlights the typical operating wavelength range for applications in biosensing and tissue-relevant optics, and is commonly referred to as the therapeutic window.

Any spectroscopy application requires wavelength-resolving instruments, i.e., spectrometers, which tend to be bulky (with dimensions on a centimetre scale or larger) and expensive. Alternatively, microspectrometers based on MEMS devices [Antoszewski et al., 2002, Wolffenbuttel, 2004], offer more cost-effective, portable, and miniaturised versions of the heavy laboratory equipment. Such miniaturised instrumentation is particularly interesting for field studies and remote sensing, be it for environmental, healthcare, or even space applications.

1.2 Thesis objectives

My work is placed in the general field of microoptics with wavelength-scale structures and, in particular, it explores wavelength-scale high contrast grating across disciplines such as integrated optics and spectroscopy with a focus on the near-infrared wavelength range. While the majority of work in silicon-based micro-optics and silicon photonics has been performed with crystalline silicon (c-Si), we investigated

amorphous silicon (a-Si) for three reasons. Firstly, a-Si has a higher band gap than c-Si, thus enabling operation down to 800 nm wavelength, as opposed to >1000 nm wavelength for c-Si. Secondly, the ability of depositing a-Si on almost any planar substrate opens up a large freedom in design without being bound to common wafer structures, such as silicon-on-insulator, with pre-set thickness values. Thirdly, a-Si can be processed with all existing standard silicon fabrication facilities. In order to keep the possibility of transmission-type applications open, we chose to use glass as substrate material. Regarding structural control, the ability to impart a certain phase profile onto a corrugated structure was previously demonstrated by Fattal et al. [2010], with the phase varying between 0 and 2π . The novelty here is to thoroughly analyse the properties of amorphous silicon to incorporate multiple phase jumps into a high contrast grating lens, and to explore the limits of such a lens both in terms of fabrication and in terms of the achievable numerical aperture. The major focus of my work is on reflective grating lenses with a parabolic phase profile. In addition, new applications of high contrast grating lenses are being identified.

Tuneable MEMS FP filters have been widely used at visible [Blomberg et al., 2009, Correia et al., 1999, Gupta et al., 2012], telecom [Domash et al., 2004, Lipson and Yeatman, 2007, Masson et al., 2010], and mid-infrared wavelengths [Antoszewski et al., 2002, 2011, Meinig et al., 2011, Xu et al., 2011] for use in spectroscopy, in communications and in gas sensing. Far fewer devices have been demonstrated at near-infrared wavelengths [Chang-Hasnain, 2000, Shao et al., 2005]. One of my objectives was therefore to develop a tuneable FP filter that operates in the near-infrared range (around $1 \mu\text{m}$) to fill this gap. The target applications for such a filter ranges from biosensing, e.g., biomolecule detection on functionalised surfaces, to many other fields in the life sciences such as near-infrared spectroscopy and biomedical optics, e.g., optical coherence tomography (OCT). The idea of developing a tuneable optical MEMS filter based on HCGs was put forward by the collaborative European Union project “PROPHET” (Postgraduate Research On PHotonics as an Enabling Technology). The partners involved in this project were Tyndall National Institute Cork in Ireland, Nicolaus Copernicus University of Torun in Poland, Technical University of Berlin in Germany, and the company Superlum in Ireland. One of the long-term targets of the collaboration was to explore a tuneable filter based on high contrast gratings that could eventually become the wavelength-selecting element of a swept-source laser for optical coherence tomography applications.

In summary, the main goals of my work were:

- Design, fabrication, and characterisation of broadband reflectors and flat diffractive lenses with high numerical aperture using amorphous silicon high contrast gratings
- Explore the performance of flat grating lenses and identify possible applications
- Design, fabrication, and characterisation of static and tuneable MEMS-based optical filters using amorphous silicon high contrast gratings

1.3 Thesis organisation

This thesis is divided into several units, which all revolve around the topic of wavelength-scale high contrast gratings. Following the introduction and thesis outline, the next two chapters provide the general theoretical background of diffraction gratings together with an overview of the state-of-the-art in the field of micro-optics and tuneable MEMS Fabry-Pérot resonators (Chapter 2), and the relevant processing steps needed to realise such devices (Chapter 3). In the next four chapters, my original results are presented. Chapter 4 shows the design, fabrication, and experimental verification of spectrally broadband reflectors based on wavelength-scale gratings with a large index contrast in the near-infrared wavelength range. By adding the functionality of wave front shaping to the reflector, the development of flat focussing grating lenses with a high numerical aperture in amorphous silicon is presented in Chapter 5 in conjunction with a detailed characterisation of the device and an application example. Chapter 6 presents the design, fabrication, and evaluation of metal-based and grating-based static Fabry-Pérot cavities as a primary stage to facilitate filters with a good optical performance. Chapter 7 puts the prior findings together to make up a tuneable filter based on microelectromechanical systems including an extensive study of the deformation of different suspension designs and the fabrication challenges involved. Finally, the results are concluded and a general outlook is given in Chapter 8.

2 Theory and state-of-the-art

2.1 Wavelength-scale high contrast gratings

Diffraction gratings play a major role in optics whenever light has to be spectrally separated, redirected or coupled into a structure. Gratings can have a large size with grooves on a macroscale, but they also can have features sizes comparable to the incident wavelength in which case they are called wavelength-scale gratings. In fact, a wavelength-scale grating gives rise to interesting optical properties, because there is typically only a single diffracted order. Gratings of this type are referred to as photonic crystals or high contrast gratings (HCGs). Depending on the spatial distribution of the index modulation, they are classified into one (1D), two (2D) or three dimensional (3D) photonic crystals (PhCs) [Joannopoulos et al., 2008]. Three dimensional photonic crystals with index alterations in all three spatial dimensions are very challenging to realise in practise, especially if they require functional defects, hence this work concentrates on planar high contrast gratings with one-dimensional periodicity. The physical mechanisms behind ordinary diffraction gratings are explained in the following, leading over to guided-mode resonances [Wang et al., 1990] and high contrast gratings [Karagodsky and Chang-Hasnain, 2012] in the near-wavelength regime.

2.1.1 Diffraction theory

In general, plane waves that interact with periodic structures will form an electromagnetic field pattern within the structure that can be understood as an interference pattern between the incoming plane wave and the structure [Norton et al., 1997]. The field pattern can then be analysed by expanding it to a Fourier series. The resulting field \vec{E} , with \vec{r} being the vector spanning the 3D spatial coordinates of the field, is described by the Bloch theorem [Born and Wolf, 1999]:

$$\vec{E} = \vec{A} \cdot \exp(-j\vec{k}_0 \cdot \vec{r}) \quad (2.1)$$

The electromagnetic field within the periodic structure comprises two parts: a) the exponential term with \vec{k}_0 , the incident wave vector, which describes the plane wave propagation, and b) the term \vec{A} which represents the envelope function of the field, and takes into account the periodicity of the structure; $j = \sqrt{-1}$. The periodicity is usually denoted by the grating vector \vec{G} , which is inversely related to the periodicity a of the structure $|\vec{G}| = 2\pi/a$. The situation of an incident plane wave impinging on a one-dimensional diffraction grating with effective refractive index n_{eff} (specified in Equations 2.5 and 2.6) at an angle of incidence θ_0 is shown in Figure 2.1.

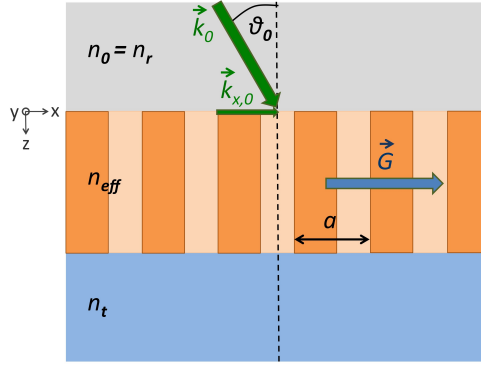


Figure 2.1: Incidence of a plane wave on a one-dimensionally periodic diffraction grating.

As the boundary conditions dictate the tangential component of the wave vector be continuous, the lateral components of the incident wave vectors $\vec{k}_{x,0}$ and the resulting diffracted wave vectors $\vec{k}_{x,p}$ have to be phase-matched. This phase-matching process, i.e., specifying the diffracted modes with order p or spatial harmonics $\vec{k}_{x,p}$ of the structure in the lateral direction, is also called the Floquet condition [Gaylord and Moharam, 1985]:

$$\vec{k}_{x,p} = \vec{k}_{x,0} - p\vec{G} \quad (2.2)$$

In contrast to the calculation of the lateral wave vector components, the resulting vertical wave vectors of the Bloch modes $\vec{k}_{z,p}$ supported by the structure are then obtained from the dispersion relation of the periodic structure:

$$\vec{k}_{z,p}^2 = (\vec{k}_0 n_{eff})^2 - \vec{k}_{x,p}^2 \quad (2.3)$$

Starting from the Floquet condition (Equation 2.2) and after some mathematical treatment, we arrive at the well-known grating equation (for unslanted gratings):

$$n_{eff/r/t} \sin \theta_p = n_0 \sin \theta_0 - p \frac{\lambda_0}{a} \quad (2.4)$$

In the grating equation, $n_{eff/r/t}$ is the refractive index inside the grating n_{eff} or on either the reflected $n_r = n_0$ or the transmitted n_t side of the grating, θ_p is the angle of the p^{th} diffracted beam, and λ_0 the free space wavelength. It should be noted that the grating equation provides information about the angle of the diffracted modes, but not the distribution of power among them.

2.1.2 Guided-mode resonances in wavelength-scale high contrast gratings

The common diffraction phenomena occur in a regime where the period of the grating is much larger than the wavelength of the incident electromagnetic radiation. If, however, the period is much smaller than the incident wavelength, the light cannot “resolve“ the small structure. In that case, the grating operates in the deep sub-wavelength regime [Karagodsky and Chang-Hasnain, 2012] and the light behaves as if it was impinging on a medium with a homogeneous index of refraction [Lalanne and Lemercier-Lalanne, 1997]. Such gratings can be analysed by effective medium theory [Lalanne and Lemercier-Lalanne, 1996], which approximates the electromagnetic field solutions within the grating and predicts their spectral properties rather precisely. For these so-called sub-wavelength gratings, physically, only the zeroth order of the diffracted waves is real and propagating, whereas all higher order modes are imaginary and hence evanescent, which brings about very interesting phenomena. In the past decades diffraction gratings with sub-wavelength features have attracted much attention as the phenomenon of Wood’s anomalies [Wood, 1902] rendered it possible to make optical devices, which are not obtainable outside that regime. The Wood anomaly typically occurs for the case of the grating period being smaller or close to the wavelength. In this case, the incident wave resonantly couples to guided modes [Wang and Magnusson, 1993] supported by the grating. These guided modes, as they propagate, may re-couple to free-space

modes [Fan and Joannopoulos, 2002] and are therefore leaky [Tamir, 1975], which upon interference with the incident wave leads to pronounced spectral features in transmission or reflection [Wang and Magnusson, 1993]. These features are also called guided-mode resonances (GMRs) or resonant waveguide-grating effects [Rosenblatt et al., 1997, Wang et al., 1990]. Away from resonance, the optical response is simply that of an ordinary multi-layer with typical Fabry-Pérot fringes. Figure 2.2 illustrates the geometries and the parameters of a grating with one-dimensional index modulation for the diffraction regime (Figure 2.2a) and regime when the periodicity is on the order of the incident wavelength [Karagodsky and Chang-Hasnain, 2012] (Figure 2.2b).

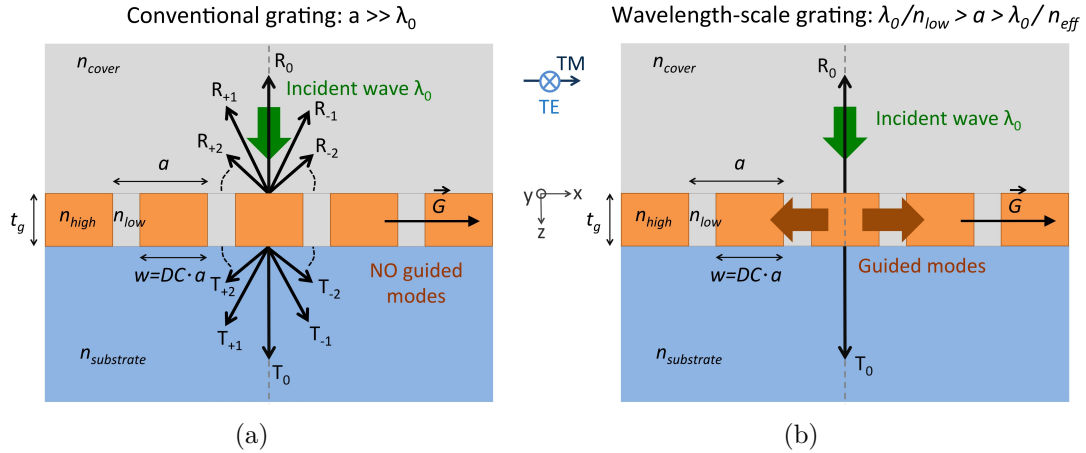


Figure 2.2: Schematic illustrations of the geometry of a 1D grating with thickness t_g , high n_{high} and low n_{low} refractive index, and grating vector \vec{G} for (a) the diffraction regime and for (b) the near-wavelength regime [Karagodsky and Chang-Hasnain, 2012]. The grating geometry is invariant in the y direction, extends to infinity in the x and y directions, and is polarisation-sensitive. (a) The normally incident wave with vector \vec{k}_0 and the zeroth (R_0 , T_0) and first two diffraction orders ($R_{\pm 1}$, $T_{\pm 1}$, $R_{\pm 2}$, $T_{\pm 2}$) on the reflected and the transmitted side are shown. (b) Only the zeroth-order modes exist and the two counter-propagating quasi-guided modes are shown inside the grating region.

The grating consists of alternating regions of high and low indices of refraction (n_{high} and n_{low} , respectively) with a layer thickness t_g , period a and duty cycle DC , which is defined as the ratio of the width w of the high index region to the period. In principle, the grating can take any shape, but for convenience, a rectangular profile is chosen here. Above and below the grating are the cover n_{cover} and the substrate index of refraction $n_{substrate}$, whereas the refractive index of the cover region often coincides with the index in between the grating ridges ($n_{cover} = n_{low}$). Sometimes, an additional lower index layer is used underneath the grating layer

to act as the waveguide layer, whereas the grating has mainly the function of the phase-matching layer between cover and waveguide layer [Sun et al., 2009]. For reflective wavelength-scale gratings this lower index layer is a critical parameter [Mateus et al., 2004] and can contribute to enhancements in the reflection band [Shokooh-Saremi and Magnusson, 2008b]. The grating is assumed to extend infinitely into the x and y direction. Due to the artificial anisotropy of the grating structure, birefringence occurs, which means that the effective indices for TM and TE polarised waves are different [Born and Wolf, 1999]:

$$n_{eff}(\text{TM}) = \frac{1}{\sqrt{\frac{DC}{n_{high}^2} + \frac{1-DC}{n_{low}^2}}} \quad (2.5)$$

$$n_{eff}(\text{TE}) = \sqrt{DC \cdot n_{high}^2 + (1 - DC) \cdot n_{low}^2} \quad (2.6)$$

A conventional diffraction grating with a large feature size generates several diffraction orders both on the reflected and transmitted side of the grating, highlighted as $R_{\pm p}$ and $T_{\pm p}$ (with p being an integer) in the figure. For the wavelength-scale gratings considered in this work, the feature sizes are such that only the zeroth-order diffracted mode (i.e., R_0 or T_0) will carry energy and propagate away from the grating structure.

In the following, the physical effects occurring in the grating region will be elucidated further. The wave vector \vec{k}_0 of an incident plane wave can be decomposed into lateral or in-plane wave vectors \vec{k}_x as well as vertical wave vector components \vec{k}_z . Also, we are dealing with two mode categories in GMR structures:

- the diffracted modes p governed by the diffraction grating,
- and the allowed guided modes ν of the equivalent waveguide structure,

which both can be thought of as certain directions or angles into which the electromagnetic power is transferred.

For the guided-mode resonance to occur, several conditions have to be met. Firstly, the effective index of refraction n_{eff} of the grating region must be larger than the indices of the adjacent media n_{cover} , $n_{substrate}$ to form an equivalent waveguide, which can support guided modes. Secondly, the incident wave must be

able to excite these guided modes through phase matching the in-plane wave vector components of the ± 1 diffracted orders with the grating vector \vec{G} (Floquet condition, see Equation 2.2) [Brundrett et al., 1998, Collin, 1960, Wang and Magnusson, 1993], which is achieved by choosing the grating period as to satisfy the inequality $\lambda_0/n_{low} > a > \lambda_0/n_{eff}$ at normal incidence [Ye et al., 2006]. Since the guided modes are not true waveguide modes due to their leaky nature, they possess a finite lifetime and can couple to external radiation modes [Ding and Magnusson, 2007, Fan and Joannopoulos, 2002]. Lastly, the grating thickness t_g must be chosen so that the propagation constant within the effective waveguide structure equals the in-plane wave vector components of the ± 1 diffracted orders, thereby satisfying the transverse resonance condition of these orders [Brundrett et al., 1998, Ye et al., 2006].

For weakly modulated gratings, which can be regarded as a perturbation of an unmodulated slab waveguide [Brundrett et al., 2000], classical waveguide theory can be applied to predict the locations of the GMRs rather precisely [Wang and Magnusson, 1993]. As the grating modulation increases, the prediction of the GMRs becomes less precise and more rigorous theories such as RCWA [Moharam and Gaylord, 1981], which is outlined next, or modal methods [Chu and Kong, 1977, Peng et al., 1975]) have to be used.

The intriguing properties of GMRs have been utilised for a variety of optical devices. Besides the realisation of optical filters with either very sharp transmission [Magnusson and Wang, 1995, Tibuleac and Magnusson, 1997] or reflection features [Wang and Magnusson, 1995], modulators [Rosenblatt et al., 1997], ultrathin mirrors with a high and spectrally broad reflection band [Mateus et al., 2004], wave plates [Mutlu et al., 2012a], anti-reflection layers [Kanamori and Hane, 2002], gratings for beam splitting operation [Wu et al., 2009] and polarisation sensitivity [Mutlu et al., 2012b] or independence [Wu et al., 2010] as well as focussing lenses and reflectors [Fattal et al., 2010, Lu et al., 2010] have been demonstrated. Gratings with sub-wavelength feature sizes and a very strong refractive index modulation (typically $\Delta n > 1.8$ [Karagodsky et al., 2010b]) are typically referred to as wavelength-scale high contrast gratings (HCGs) [Chang-Hasnain, 2011]. The geometry of a typical high contrast grating with a normally incident wave is shown in Figure 2.2b. It contains regions of high refractive index n_{high} and lower index n_{low} of which the lower index region is often the same as the cover medium (typically air). For wave incidence at wavelength λ_0 and an appropriate grating geometry, some modes (the two counter-propagating fundamental waveguide modes are indicated in the figure) are eventually excited in the grating region and form a standing wave pattern at

resonance, and re-radiate leaky waves back into the cover medium in the case of reflection (or into the substrate in the case of transmission). Depending on the relative phases, nearly 100% reflection (or 100% transmission) can be achieved by the resulting interference [Karagodsky and Chang-Hasnain, 2012]. The operation of HCGs lies in the intermediate, wavelength-scale, region in between the common diffraction $a \gg \lambda_0$ and deep-sub-wavelength regime $a \ll \lambda_0$; the grating period is typically smaller than the incident wavelength λ_0 , but larger than the wavelength inside the grating λ_0/n_{eff} [Karagodsky and Chang-Hasnain, 2012]. If several guided-mode resonances are in close spectral proximity, then these resonances can combine to give rise to a broad resonance in reflection [Shokooh-Saremi and Magnusson, 2008b], which is of main interest in my thesis.

2.1.3 Rigorous coupled-wave analysis

In 1981, Magnusson and Gaylord demonstrated a rigorous and easy-to-implement algorithm, which they called the rigorous coupled-wave analysis, to analyse the diffraction from planar gratings surrounded by two different homogeneous media [Moharam and Gaylord, 1981]. Compared to earlier descriptions that incorporated a number of approximations [Kogelnik, 1975, Magnusson and Gaylord, 1977], this exact analysis took higher order waves, boundary diffraction, and the second-order derivatives of the field amplitudes into account. The basic principle of RCWA is the Floquet theorem as described in Section 2.1.1. The algorithm calculates the electromagnetic fields in transmission and in reflection, from which all diffraction efficiencies of transmitted and reflected orders can then be deduced. It can be applied to any arbitrarily shaped periodic grating and is easily implemented in digital codes due its formulation in matrix form. The “exact“ description of the electromagnetic fields involved in the optical diffraction problem is strictly valid only for infinite grating structures. Since then, RCWA has been applied to many optical diffraction problems dealing with periodic structures for applications such as grating filters, distributed feedback lasers, and grating couplers. Most of the literature on RCWA covers the wave propagation in one-dimensionally periodically stratified media, i.e., structures in which the refractive index is modulated in one direction of space [Lalanne and Hugonin, 1998, Li and Haggans, 1993, Moharam and Gaylord, 1986, Peng and Morris, 1995]. Implementations of RCWA for structures with periodicity in two dimensions of space exist [Lalanne, 1997, Liscidini et al., 2008, Sakai et al., 2007], but they are more complicated and mathematically more intense. As all mathematical details of the RCWA calculations are well described in the literature [Moharam and

Gaylord, 1981] and are not subject of this thesis, I will only outline the main principles with reference to the corresponding literature.

Our research group has already established a numerical code based on one-dimensional RCWA based on the thesis of Harper [2003], which is implemented in MATLAB (Mathworks). Figure 2.3a shows the general grating geometry considered in this work.

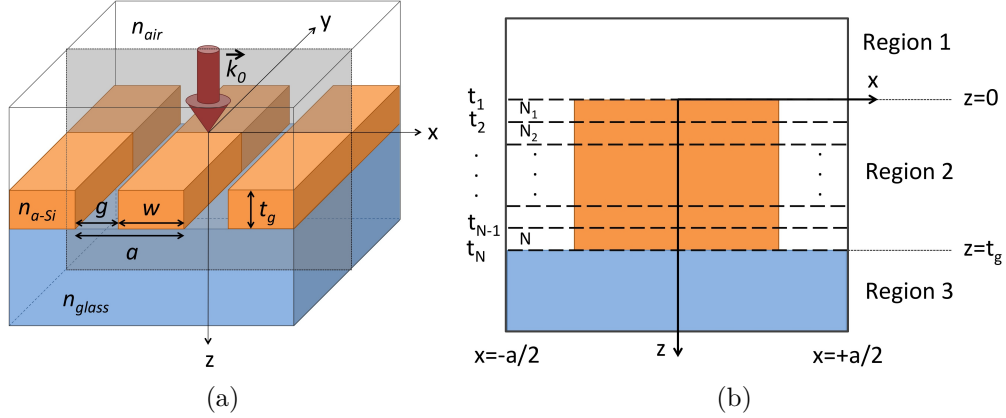


Figure 2.3: (a) A fraction of the infinitely periodic and asymmetric 1D grating geometry considered in this work with the parameters n_{air} , n_{a-Si} , n_{glass} , g , w , a , and t_g as described in the text. The grey-shaded area depicts the plane of incidence with the wave vector \vec{k}_0 . (b) Discretisation of the unit cell of the periodic structure into N thin grating slices, which are computed separately by RCWA.

The grating has a finite thickness t_g in the z direction and extends infinitely along the x and y coordinates. Both the cover and the substrate have a lower index of refraction than the grating bars and the effective refractive index of the grating (n_{cover} , $n_{substrate}$, $< n_{eff} < n_{a-Si}$) and are stretching out to infinity into all three directions of space. We typically use air as the cover medium and a substrate of glass, so the structure is asymmetric. The grating bars are composed of amorphous silicon with width w and are separated by the gap width g at a periodic interval a . Hence the structure is only one-dimensionally periodic in x direction and the periodicity is on the scale of the vacuum wavelength or even smaller. The duty cycle DC , which describes the filling fraction of the grating with the high index material n_{a-Si} is given by the ratio of the grating bar width w and the periodicity a . The incident wave with wave vector \vec{k}_0 is taken to propagate in the xz plane; its polarisation has to be discriminated in the simulation depending on whether the electric field is oriented perpendicular to the grating (TM polarisation) or parallel to the grating (TE polarisation). For the analysis, it is helpful to divide the geometry into three different

regions: region 1 represents the cover medium, region 2 the grating structure, and region 3 the medium of the substrate. In these regions, the electromagnetic fields for each diffracted order p are considered separately; region 1 contains the sum of the incident and reflected (diffracted) fields:

$$\vec{E}_1 = \exp(j\vec{k}_1 \cdot \vec{r}) + \sum_{p=-\infty}^{\infty} R_p \exp(-j\vec{k}_{1,p} \cdot \vec{r}) \quad (2.7)$$

whereas region 3 contains the transmitted fields with \hat{z} , the unit vector in the z direction:

$$\vec{E}_3 = \sum_{p=-\infty}^{\infty} T_p \exp[-j\vec{k}_{3,p} \cdot (\vec{r} - d\hat{z})] \quad (2.8)$$

Region 2 is the modulated region involving more elaborate steps to describe the fields:

$$\vec{E}_{2,N} = \sum_{p=-\infty}^{\infty} S_p(z) \exp(-j\vec{k}_{2,p,N} \cdot \vec{r}) \quad (2.9)$$

R_p , T_p , and $S_p(z)$ are the complex amplitudes of the reflected, transmitted and of the fields within the grating, respectively, and $\vec{k}_{2,p,N}$ the wave vectors for the diffracted waves of the N^{th} slab. The goal of the simulation is to determine the amplitudes of the reflected and the transmitted waves for each diffracted order in regions 1 and 3 and the amplitude of the waves with that order in the modulated region 2. The grating in region 2 is divided into N thin planar grating slices (Figure 2.3b), where the amplitudes of the diffracted wave are worked out by solving the wave equation in each slice. The thinner the slices are made, i.e., the higher the discretisation, the more accurate the final results will be. In each slice, the electric field is represented by coupled-wave equations and is expanded in terms of the diffraction orders of this field. The total field representation then contains the sum of all field amplitudes in each slice for the diffracted orders in the grating with the wave vectors resulting from the Floquet theorem, as stated in Section 2.1.1; hence these waves are also called Floquet waves. The next step includes the phase matching of all diffracted orders in all regions to fulfil the boundary conditions; this phase matching happens sequentially from region 1 to slice 1 of the grating, then from slice 1 to slice

2 of the grating, and so forth, until the last slice N will be phase-matched with region 3. Through this procedure a matrix of equations is built, which is solved numerically for the target field amplitudes of the diffracted orders in region 1 and 3. Having obtained the amplitudes, the diffraction efficiency of the reflected waves DE_{refl} and of the transmitted waves DE_{trans} can be computed for each diffraction order p by using the following relations:

$$DE_{refl,p} = \frac{I_{refl,p}}{I_0} \quad (2.10)$$

and

$$DE_{trans,p} = \frac{I_{trans,p}}{I_0} \quad (2.11)$$

Here, I_0 is the intensity of the incident wave and I_{refl} and I_{trans} are the intensities of the reflected and transmitted waves, respectively, for the diffraction order m considered. In other words, the diffraction efficiency gives a measure of how much power of the reflected or transmitted waves is concentrated in a specific order of diffraction. Examples of a spectrally narrow GMR band pass filter and a broadband mirror using silicon-based sub-wavelength gratings at near-infrared wavelengths are shown in Figure 2.4 together with their index profiles. These designs were calculated with RCWA, taking into account the refractive index of crystalline silicon [Filmetrics, 2014].

In my work, I focus on wavelength-scale high contrast gratings that operate in the zeroth diffraction order and their realisation as broadband mirrors and as focussing elements. The main assumptions for the calculations are the following:

- The gratings are either based on amorphous silicon deposited on a glass substrate (sample 1) or on amorphous silicon on a thin silicon nitride membrane (sample 2).
- The grating has a single-level binary profile with periods at the scale or smaller than the incident vacuum wavelength.
- All media are homogeneous, linear, and isotropic.
- Unless stated otherwise, the waves impinging on the grating are normally incident plane waves and the grating extends infinitely in the lateral dimensions.

- I define the transverse magnetic (TM) polarisation such that the electric field is oriented within the plane of incidence and perpendicular to the grating lines (xz plane). The transverse electric (TE) polarisation occurs if the electric field vector is parallel to the grating lines and lies perpendicular to the plane of incidence (xy plane).

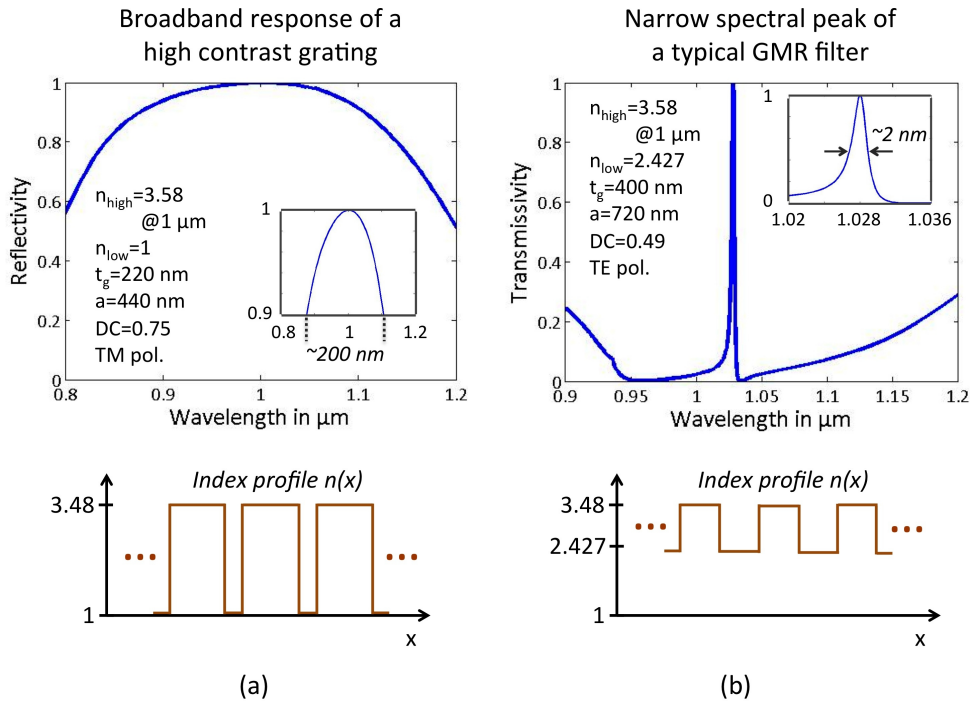


Figure 2.4: (a) Example of a broadband silicon mirror with reflectivity above 90% centred on a wavelength of $1 \mu\text{m}$ with a spectral range $>200 \text{ nm}$ (inset) and index profile. (b) Example of a sharp resonance in transmission close to $1 \mu\text{m}$ for a silicon-based sub-wavelength grating; the FWHM of the peak is approximately 2 nm (inset); the index profile is given below. Design parameters are given in the graphs; dispersion and absorption losses of crystalline silicon [Filmetrics, 2014] are included in the simulation.

An important performance measure for the RCWA is the number of orders retained in the simulation. According to the Floquet theorem, the number of Floquet waves inside the grating is infinite. However, in numerical calculations, this number has to be truncated to a finite number; a common method of verification is a convergence test, which reveals the minimum number of orders required to obtain a stable and an accurate solution.

2.2 Beam shaping in microoptics

The general trend in technology to shrink devices to ever smaller sizes does not exclude optical devices, and shaping optical beams in the sub-millimetre range has opened a range of opportunities. Crucial application areas are integrated silicon photonic and imaging systems as well as biophotonic and medical applications, the latter targeting the study of cells in lab-on-chip systems. Besides conventional components based on refractive optics, such as microlenses, diffractive optical elements, particularly based on high refractive index semiconductors, are becoming increasingly attractive due to their rich optical properties. At the same time, such elements conform to the processing standards of the semiconductor industry and can be mass-produced, an essential requirement for low-cost manufacture. Prominent candidates of such diffractive optical elements are the wavelength-scale high contrast gratings (HCGs) utilising the guided-mode resonances introduced in Section 2.1.1.

2.2.1 General overview of microlenses

There are numerous ways of controlling electromagnetic waves to converge at an intense focal point, which yields one of the main building blocks in optics: the lens element. When electromagnetic plane waves pass through a lens, ideally, each point on the lens changes the optical path of the wavefront in such a way that all waves interfere constructively in the focal region, and hence form a bright spot [Hecht, 2002]. The absolute phases imprinted on the wavefront by the different regions of the lens do not matter, as long as they are correct with modulo 2π and the waves add coherently in the focal spot. In the focussing process, the lens transforms the incident plane waves to spherical waves, which have their virtual origin in the focal spot. The lens effect can either be based on refractive or diffractive phenomena. Figure 2.5 shows the cross-sections of typical converging lenses based on these effects.

A related refractive-type element with focusing ability, operating in reflection, is the curved mirror. From a geometrical point of view, the spherically shaped profile of the refractive-type lens determines the optical path with which each ray contributes to the coherent summation in the focal spot (Figure 2.5a). The optical path of each ray is determined by the refractive index and the physical distance travelled by the light ray within the lens material and in the surrounding medium, which is usually air. Due to its smooth spherical surface, each point on the lens provides the correct phase delay. As the lens material depends on the wavelength, dispersion causes

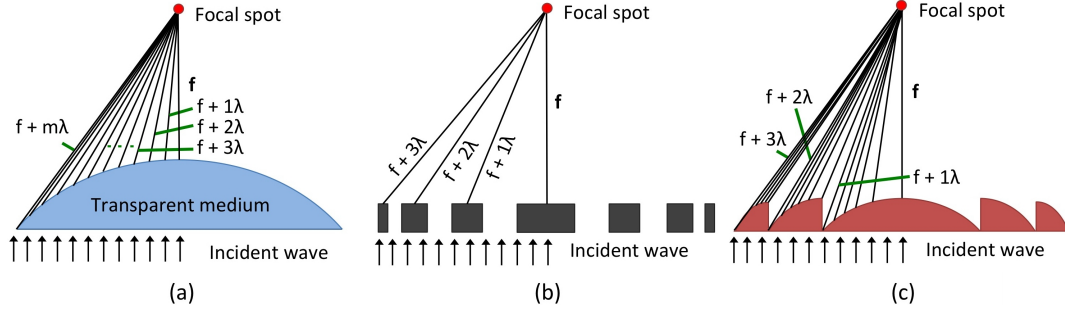


Figure 2.5: Cross-sectional profiles of typical converging lenses with a ray picture of the plane waves incident from the bottom and combining at the focal spot at the top. (a) Plano-convex transmissive lens based on refraction. (b) Amplitude-type Fresnel zone plate based on diffraction. (c) Multi-level Fresnel lens. The solid black lines indicate the coherent optical rays emanating from the lens and contributing to the focal spot.

chromatic aberration. While sophisticated lenses such as microscope objectives can reach numerical apertures of >1 , the simpler fabrication methods used for microlenses tend to limit their numerical apertures achieved in practice to values <0.6 or otherwise incur higher spherical aberrations [Ottevaere et al., 2006]. These fabrication methods include microjet printing [Chen et al., 2002], photoresist reflow techniques [Popovic et al., 1988], and direct laser writing [Gale, 1997]. Generally, microlenses based on polymers tend to have a higher index than glass, e.g., $n_{SU-8} \sim 1.57$, $n_{glass} \sim 1.44$ at a wavelength of $1 \mu\text{m}$. Additionally, the dependency on transparent materials limits their spectral range mainly to the visible so that it is more challenging to make lenses in the near-infrared wavelength range or beyond.

Classical diffractive-type lenses are the Fresnel zone plate (FZP) and the Fresnel lens. The Fresnel zone plate has a binary topography and is an arrangement of alternating concentric rings, which either absorb or transmit electromagnetic radiation. As shown in Figure 2.5b, each zone adds an integer multiple of the wavelength to the optical path [Beynon and Strange, 2000]. The numerical aperture of the FZP depends on the smallest zone width of the outermost zone. The diffraction efficiency of the FZP is limited by the fact that the phases are only correct at specific points; for all other points, phases partially interfere destructively, which limits the throughput. For amplitude-type zone plates, there is additional absorption loss, as only half of the light is transmitted, which limits the theoretical efficiency to approximately 10% [Bass et al., 2000]. For rectangular phase-type zone plates, the maximum efficiency is 40%. Including the right thickness in each zone ultimately leads to a Fresnel lens with a continuously varying phase shift, which therefore

may reach near 100% efficiency [Bass et al., 2000]. An ideal Fresnel lens consists of concentric rings of spherically shaped surfaces with increasingly steeper slopes towards the outermost ring (Figure 2.5c). Along each concentric ring, the optical pathlength of the emanating waves increases by one wavelength and hence the optical phase by 2π . But the difficulty with these lenses is to obtain a smooth spherical relief on a microscale in terms of fabrication using staircase lithography.

In diffractive optics, microstructures based on index-modulated dielectric materials (e.g., photonic crystals) or metals (plasmonic metastructures) have long been known to shape light beams in a controllable manner [Notomi, 2010, Rayleigh, 1887, Yablonovitch, 1993, Yeh, 1988], which will be presented next.

2.2.2 Beam shaping with diffractive microstructures

In 1975, Tamir [1975] already discussed the control of light beams utilising “structures with variable leaky-wave characteristics“ in the lateral direction by changing either the periodicity or the thickness of the grating, or both parameters. Such early work forms the basis of more recently developed diffractive optical beam shaping elements based on one- or two-dimensional photonic crystals and plasmonic microstructures.

Following the trend of ever decreasing structural sizes, a relatively new field within microstructured optics is the field of planar or flat optics [Yu and Capasso, 2014]. Planar designs are advantageous because they are compatible with standard lithographic methods, but more importantly, they offer new functionality that may not be readily achievable with conventional microoptical elements. For diffraction gratings, beam shaping has been performed by varying either the duty cycle with constant lattice period [Levy et al., 2005, Stork et al., 1991, Vo et al., 2014], or by altering both the duty cycle and the period, or by altering only the period [Fattal et al., 2010]. Another possibility is the modulation of the thickness [Qiaoqiang et al., 2008]. All these methods establish a defined spatially varying distribution of the refractive index across the structure in order to produce a desired variation in the optical pathlength. For example, a gradual change of the index distribution produces a linear phase profile and is utilised to make mirrors or other beam steering devices. Examples of 1D and 2D binary gratings with such beam steering abilities are listed in reference [Farn, 1992]. A radial index modulation with a quadratic phase variation creates a lens effect. Figure 2.6 serves as an overview for the realisation of lens-like microstructures (wave incidence from top or bottom of the structure).

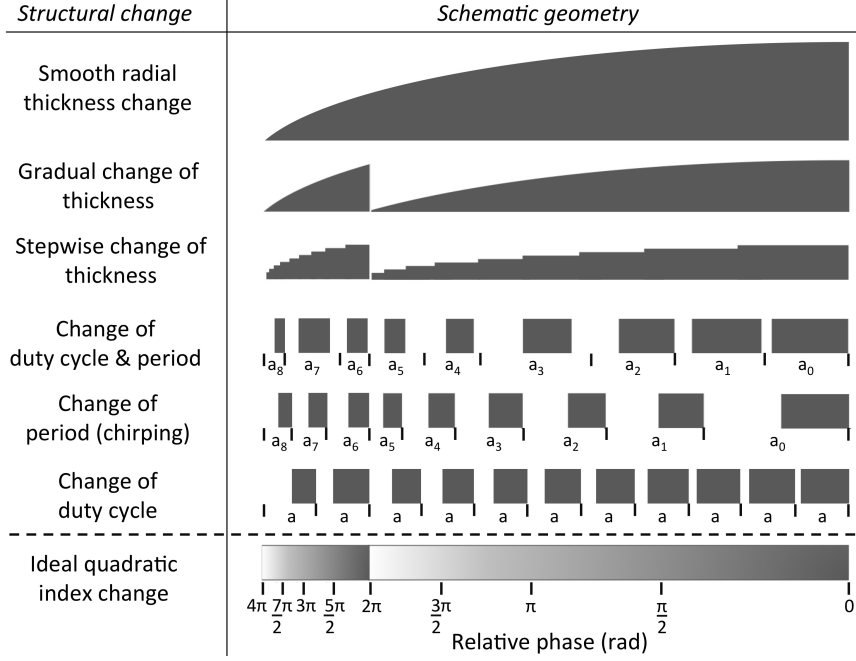


Figure 2.6: Typical half shapes of lenses with a quadratic phase relation and two phase jumps shown. The bottom geometry illustrates the ideal index profile. a denotes the periodicity and a_n with a subscript index n a varying period.

For sub-wavelength grating-based structures and guided-mode resonance devices, it is known that the variation in filling fraction (or duty cycle) of a wavelength-scale grating induces a change in the coupling conditions between the external waves and the guided modes within the structure on a localised scale [Srinivasan et al., 2009]. This leads to so-called localised resonances [Brongersma et al., 2014], which several research groups have utilised to imprint a local modulation of the phase onto gratings to obtain a microstructured lens. Fattal et al. [2010] and Lu et al. [2010] have utilised this effect to show experimentally how a non-periodic patterning of a silicon grating enables full control over the reflected wave front at telecom wavelengths. Numerical simulations have shown the possibility of creating a 2D grating lens [Chen et al., 2008, Lu et al., 2010]. The lens design is based on the fact that for wavelength-scale high contrast gratings, the quasi-guided modes within the grating have a very short in-plane propagation length, which causes the light to leak or scatter out very rapidly [Fattal et al., 2010]. Consequently, the optical properties can be adjusted on the length scale of a few grating periods.

An alternative method of exercising in-plane phase control is to use plasmonic resonances and vary them across the plane. For example, the group of Capasso [Yu

et al., 2011] has demonstrated focussing lenses based on this effect. Each plasmonic element can be considered an antenna that individually controls the phase of an incoming wave; hence the phase can be controlled almost at will at every point. Accordingly, they have designed an array of antennas with sub-wavelength spacing to demonstrate planar lenses and axicons free of monochromatic aberrations such as astigmatism, spherical aberrations, and coma [Aieta et al., 2012]. The downside of plasmonic resonances, however, is that they are intrinsically lossy, which is why we followed up the beam shaping approach with a dielectric functional material (amorphous silicon). The design, construction, and testing of a new type of flat diffractive lens are described in Chapter 5.

2.3 Wavelength-selective Fabry-Pérot filters

One of the applications of HCG mirrors that motivated my research is as to serve as mirrors in a Fabry-Pérot cavity. Hence, I will look at Fabry-Pérot cavities next, i.e., both at static cavities and at tuneable ones.

2.3.1 Fabry-Pérot resonator

The operation of a Fabry-Pérot interferometer (FPI) is based on interference between multiply reflected beams in a cavity made of two reflecting surfaces with reflectivities R_1 and R_2 and possible absorptions or scattering losses A_1 and A_2 (Figure 2.7a). If the mirror reflectivities are different, $R_1 \neq R_2$, the device is called an asymmetric FPI; if they are same, $R_1 = R_2 = R$, it is called symmetric. In the case of a plane-parallel and symmetric FPI, at the resonant wavelength and assuming no absorption losses, the incoming beam reflected from the first surface (ray r_1 in Figure 2.7a) undergoes destructive interference with the beam coupling out of the cavity (rays r_2, r_3, r_4 in Figure 2.7a), so the cavity reflectivity I_r is zero and the transmission I_t is unity on resonance. The transmission as a function of wavelength consists of a set of peaks that are equally spaced in frequency according to their interference (or fringe or mode) order m , which is an integer value.

The predominant cases in the experimental part of this work are symmetrical FPIs eventually exhibiting the dissipative losses A_1 and A_2 given by the linear absorption $A_q = \exp(-\alpha_q \cdot z)$, with α being the absorption coefficient, q an integer,

and z the distance over which the attenuation acts. For symmetric FPIs containing no loss mechanisms, the intensity transmittance function $I_t(\delta)$ is given by Airy's formula [Born and Wolf, 1999, Yariv and Yeh, 2007]:

$$I_t(\delta) = I_0 \frac{(1 - R)^2}{(1 - R)^2 + 4R \cdot \sin^2(\frac{\delta}{2})} \quad (2.12)$$

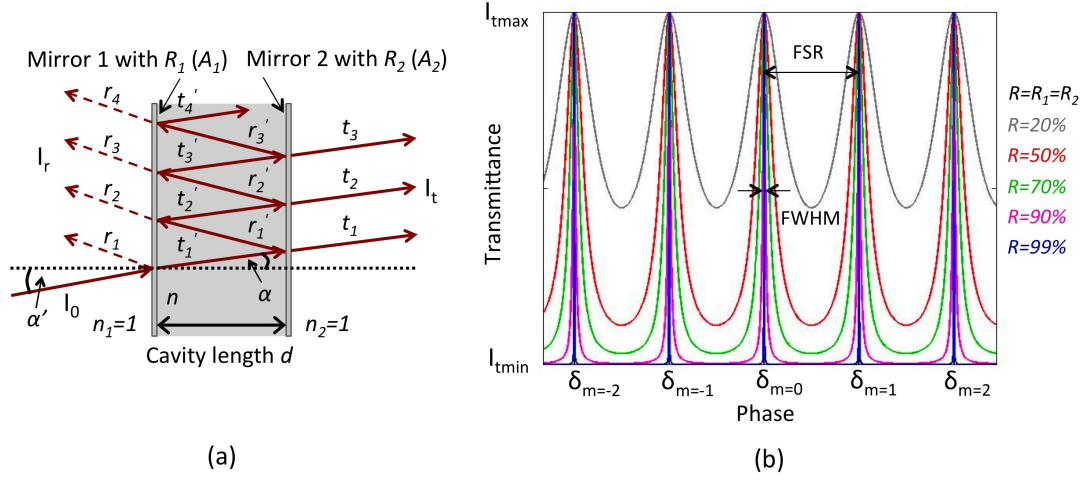


Figure 2.7: (a) Geometry of a Fabry-Pérot interferometer with the incidence angle α' , the cavity spacing d , the refractive index within the cavity n , R_1 and R_2 the reflectivities of the cavity mirrors, and I_t the transmittance function. I_r denotes the back-reflected waves. (b) Typical transmission characteristics for a symmetric FPI ($R = R_1 = R_2$) showing a series of pass bands with linewidth $FWHM$ and spectral separation FSR for five different mirror reflectivities. The target transmitted wavelength was $1 \mu\text{m}$, the spacing $d = 5 \mu\text{m}$, and the incidence angle $\alpha' = 5^\circ$. (c) Table showing the corresponding values of the reflection finesse and the spectral linewidth of the reflectivities considered in b).

When taking different mirror reflectivities and absorptions into account, i.e., treating asymmetric FPIs with dissipative losses, the corresponding functional dependence is given in a more generalised form (adapted from [Born and Wolf, 1999, Mielke et al., 1997]):

$$I_t(\delta) = I_0 \left(1 - \frac{\sqrt{A_1 A_2}}{1 - \sqrt{R_1 R_2}} \right)^2 \frac{(1 - \sqrt{R_1 R_2})^2}{(1 - \sqrt{R_1 R_2})^2 + 4\sqrt{R_1 R_2} \cdot \sin^2(\frac{\delta}{2})} \quad (2.13)$$

with the phase retardation δ given by the phase difference between successive transmitted rays

$$\delta = 2 \cdot \frac{2\pi \cdot n \cdot d \cdot \cos(\alpha)}{\lambda} + \Psi_1 + \Psi_2 = m \cdot 2\pi \quad (2.14)$$

The adjacent media to the FP cavity n_1 and n_2 are assumed to be air $n_1 = n_2 = 1$, n is the refractive index within the resonator, d the cavity spacing, I_0 the incident intensity, λ the resonance wavelength, and α the angle after passing through the first partial reflector upon incidence with an angle α' . Both reflectors eventually contribute a phase change Ψ_1 , Ψ_2 to the phase term δ , occurring at the external surfaces of the mirrors due to Fresnel reflection; however, if the dispersion of these phases is not significant they are often omitted. These equations are valid for a pair of infinite plane-parallel cavity mirrors and maintain their validity as long as a very large number of reflected waves within the cavity exists [Born and Wolf, 1999], which is the case for FPIs with large ratios of mirror size to cavity length. They are applied for metal- and grating-based FP cavities in Chapters 6 and 7. Whenever the phase difference between consecutive transmitted waves is an integer multiple of 2π (i.e., $\delta = m \cdot 2\pi$), the FPI is on resonance and the transmitted waves are constructively interfering at the resonance wavelength and result in an intensity maximum $I_{t_{max}}$. If the phase term $\delta = (m + \frac{1}{2}) \cdot 2\pi$, i.e., the cavity is off resonance, the transmitted intensity has a minimum $I_{t_{min}}$. From Equation 2.14, it follows that at resonance the peak wavelength of mode m is given by:

$$\lambda_m = \frac{2 \cdot n \cdot d \cdot \cos(\alpha)}{m} \quad (2.15)$$

For small cavity spacing, the spectral distance between consecutive transmission peaks is described by the free spectral range (FSR), usually expressed either in terms of the wavelength FSR_λ or the frequency FSR_ν (adapted from [Chung et al., 2010, Ebermann et al., 2010, Peatross and Ware, 2013]):

$$FSR_\lambda = \lambda_m - \lambda_{m+1} = \frac{2 \cdot n \cdot d \cdot \cos(\alpha)}{m(m+1)} = \frac{\lambda_m \cdot \lambda_{m+1}}{2 \cdot n \cdot d \cdot \cos(\alpha)} \quad (2.16)$$

$$FSR_\nu = \nu_m - \nu_{m+1} = \left| \frac{c}{2 \cdot n \cdot d \cdot \cos(\alpha)} \right| \quad (2.17)$$

The calculation for the FSR in terms of frequency results in a negative value, which is why the absolute value is stated. The so-called Airy peaks have a Lorentzian lineshape and are given by the linewidth FWHM (full width at half maximum) (adapted from [Tran et al., 1996]):

$$FWHM_\lambda = \frac{\lambda_m(1 - \sqrt{R_1 R_2})}{m \cdot \pi \cdot \sqrt[4]{R_1 R_2}} = \frac{2 \cdot n \cdot d \cdot \cos(\alpha)(1 - \sqrt{R_1 R_2})}{m^2 \pi \cdot \sqrt[4]{R_1 R_2}} \quad (2.18)$$

For simplicity, the Airy peaks resulting from several plane-parallel, symmetric Fabry-Pérot interferometers with a cavity spacing of $5 \mu\text{m}$, an angle of incidence of 5° , and a wavelength varied from 0.8 to $1.3 \mu\text{m}$ are shown in Figure 2.7b together with the resulting values of reflection finesse and peak linewidth for each cavity in Figure 2.7c. The higher the reflectivity of the cavity mirrors, the sharper the resonance pass bands and the higher the reflection finesse can be obtained. Due to the resonance property, the Fabry-Pérot interferometer can be applied as a narrow band pass filter for a fixed cavity spacing or as an optical spectrum analyser by scanning the cavity length (first demonstrated by Jacquinot and Dufour [1950]). An important quantity of the FPI is the reflective finesse F_R , given by the following equation [Benisty et al., 1998]:

$$F_R = \frac{m}{m+1} \cdot \frac{\pi \sqrt[4]{R_1 R_2}}{1 - \sqrt{R_1 R_2}} \quad (2.19)$$

As can be seen from the above formula, in the limit of very high interference orders, the pre-factor $\frac{m}{(m+1)}$ becomes unity and the reflection finesse is solely defined by the mirror reflectances. For low-order FPI, though, the pre-factor cannot be omitted. The total finesse, or effective finesse F_{eff} is a figure of merit for the optical performance of the FPI and is defined by the ratio of the FSR and the linewidth $FWHM$ of the resonant transmission peak:

$$F_{eff} = \frac{FSR}{FWHM} \quad (2.20)$$

In the ideal case of perfect parallelism between the mirrors, no surface irregularities, and plane wave incidence, the effective finesse equals the reflective finesse [Roychoudhuri and Hercher, 1977]. In practice, surface roughness and angular dispersion impact on the final finesse as will be dealt with in Chapter 6. Another important quality measure of an FPI is provided by the quality factor Q , describing the amount of energy stored within the cavity as per the amount of energy lost per optical cycle:

$$Q = \frac{2\pi \cdot E_{stored}}{\frac{E_{lost}}{cycle}} \quad (2.21)$$

This quantity can be extracted from the resonance peak width at the centre wavelength λ_c ($Q = \frac{\lambda_c}{FWHM_\lambda}$) and is useful to analyse properties such as the optical losses of the optical resonator.

2.3.2 State-of-the-art tuneable optical Fabry-Pérot filters

Many applications in optics require a tuneable source, be it optical networking, spectroscopy, sensing, or imaging. At the same time, one often requires narrow linewidth that is tuneable over a large spectral range, and in case of a laser source, for it to operate in a single mode. Due to their small size, efficiency, possibility for integration, and unique spectral properties, semiconductor lasers are often superior to other radiation sources [Osinski and Buus, 1987], while an external, wavelength-tuneable element provides the feedback.

There are three ways to obtain a wavelength-selective optical element. Historically, the most prominent candidate is a glass prism that disperses the light into different angles through the physical effect of refraction. Secondly, one may use the diffraction of light at a grating to disperse the different wavelengths, while thirdly, one may use interferometers and rely on interference effects. Interferometers, in particular Fabry-Pérot interferometers, combine the high throughput of prisms with the compactness of gratings and are very suitable for integration, which is why they were chosen in this project.

Changing the resonance conditions of a Fabry-Pérot resonator causes the output wavelength to shift. Equation 2.15 shows how either the cavity spacing d (Figure 2.8c), the refractive index in the cavity n (Figure 2.8a), or the angle of incidence α' (Figure 2.8b) can be adjusted for the spectral change to occur. These tuning mechanisms change the optical path in the cavity and are summarised in the top row of Figure 2.8.

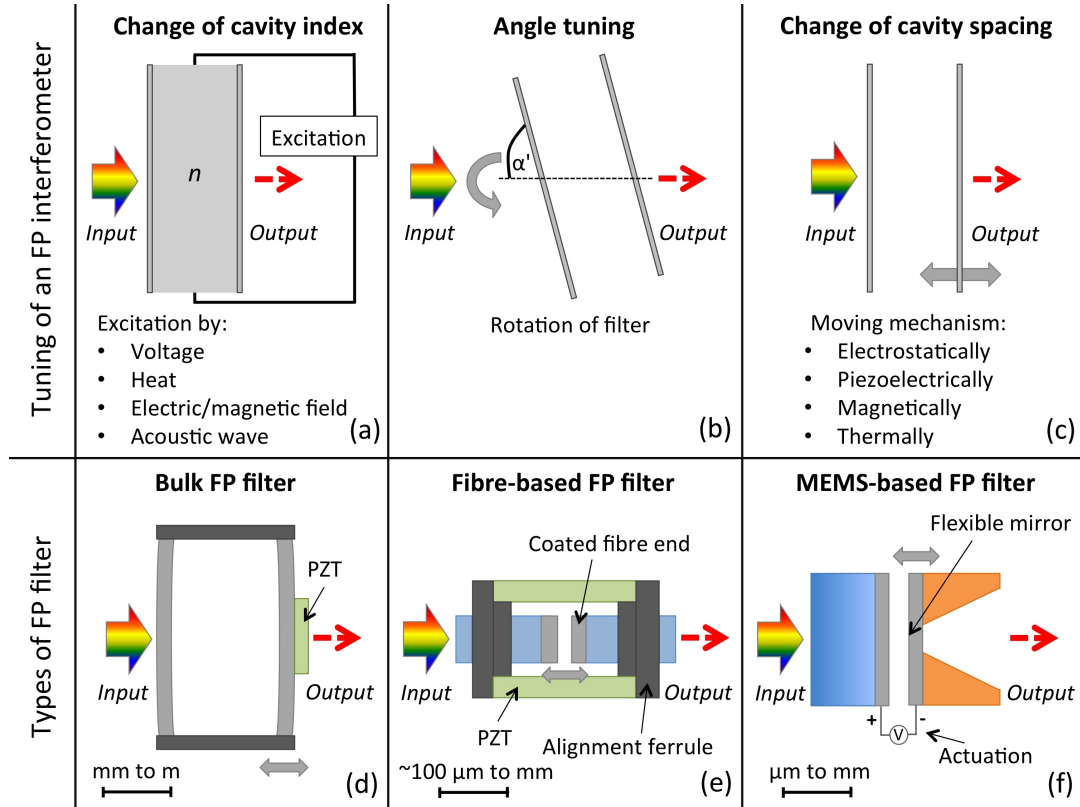


Figure 2.8: Top: Several tuning mechanisms to alter the resonance condition of a Fabry-Pérot interferometer. (a) Tuning of the cavity length. (b) Angle tuning. (c) Tuning of the cavity index. Bottom: Schematics of different types of Fabry-Pérot filters. (d) Bulk FP filter. (e) Fibre-based FP filter (adapted from Micron Optics, Inc.). (f) MEMS-based FP filter. PZT (lead zirconium titanate) is a typical material used for piezoelectric actuation.

One may change the refractive index of a material contained in the cavity by applying a voltage, an acoustic wave, or heat, thereby utilising electro-optic or acousto-optic effects (Figure 2.8a). Tuning the refractive index is very elegant, as there are no moving parts, but the tuning range is typically limited to a few nanometres in the near-IR [Larson et al., 1995]. Alternatively, a very simple method for tuning the wavelength is to rotate the filter element itself (Figure 2.8b), but the

polarisation dependence make a straightforward evaluation of the results difficult. Thirdly, in order to change the optical path via the cavity length, at least one of the two cavity mirrors needs to be moveable (Figure 2.8c). This is a widely used method due to the wide tuning capability and the relatively mature fabrication technology, which is why we adopted it for our purposes (Chapter 7).

Actuation principles for moving the mirror rely either on the piezoelectric effect, the electrostatic potential using parallel plates or comb drives, the thermo-optic, or the magnetic effect [Mroziewicz, 2008]. Due to the straightforward implementation of an electrostatic potential by using metallised plates while using low to moderate driving voltages, we chose electrostatic tuning for the development of our tuneable FP filter.

Another key criterion for FP filters is the final size; accordingly, tuneable FP filters can be classified into three types: bulk, fibre-based, and MEMS FP filters (Figure 2.8d-f). Owing to their handiness and ease of implementation, bulk FP devices (Figure 2.8d) are popular pieces of equipment in optical physics laboratory settings. Despite their smaller dimensions, challenges with fibre-based FP filters (Figure 2.8e) might be the deposition of the highly reflective optical coating directly onto the tip of the optical fibre as well as the alignment of both fibre ends. Some devices also require moderate to high voltage levels for actuation (e.g., the tuneable filter FFP-TF2 of Micron Optics, Inc.). Moving toward further miniaturisation and less power consumption, we decided to explore MEMS-based Fabry-Pérot filters (Figure 2.8f), which offer the advantages of a small footprint, a low mass, and compatibility with standard silicon fabrication while enabling new optical functionalities such as miniaturised spectrometers and sensing platforms.

Initially driven by the optical communications sector followed by great commercial successes in projection displays (DMD from Texas Instruments [Van Kessel et al., 1998], TMA from Daewoo [Kim and Hwang, 2000], grating light valve from Silicon Light Machines [Apte et al., 1993]) and other domains [Dangel and Lukosz, 1998, Hung and Senturia, 1999, Lee et al., 1999] as well as the advancements of vertical cavity surface emitting laser (VCSEL) technology [Wu et al., 1995], optical MEMS-based tuneable Fabry-Pérot filters have been investigated widely in the last decade [Hays et al., 2010, Mateus et al., 2005, Yu and Park, 2005]. The most prominent and commercially available designs utilise partially moveable multiple thin films with an air gap in between [Tayebati et al., 1998]. Optical FP filters based on MEMS technology offer a large tuneability due to the short cavity lengths involved;

for instance, a cavity spacing of $5\ \mu\text{m}$ results in a tuning range of approximately $110\ \text{nm}$ at the resonance wavelength of $1050\ \mu\text{m}$ (a crucial regime in the imaging of tissue). With the emergence of wavelength-scale high contrast gratings (HCGs) as the filter's optical core element [Zhou et al., 2008], attributes such as tuning speed, material consumption, and scalability have been advanced compared to the devices based on thicker distributed Bragg reflectors. Up to date, most of the HCG-based MEMS FP filters demonstrate operation at telecom [Boutami et al., 2006, Lipson and Yeatman, 2007], or at higher wavelength ranges [Kurth et al., 2010] while only a few are available at near-infrared wavelengths [Chang-Hasnain, 2000, Chung et al., 2010]. While in-plane FP designs have been demonstrated [Lipson and Yeatman, 2007, Masson et al., 2010], this work focusses exclusively on FP filters operating out-of-plane. When targeting applications like medical imaging and analysis of biomolecules, MEMS devices operating in the near-IR could potentially shrink the complex sizes and costs of existing bulky optical systems.

Due to the availability, design freedom, and feasibility to work at near-IR wavelengths, our choice was to use amorphous silicon high contrast gratings on a glass substrate in conjunction with a flexible membrane structure (thin silicon nitride windows from Norcada Inc.) to facilitate the tuning. The glass substrate enables the operation of the FP filter in transmission mode. The experimental results follow in Chapters 6 and 7.

3 Fabrication methods

The realisation of planar microoptical devices is carried out using microstructuring technologies established by the semiconductor industry and is usually taking place inside a cleanroom. Surface micromachining involves a combination of deposition and etching processes with the patterns being generated by lithographic methods such as photolithography or electron-beam lithography. All microfabrication processes presented in this thesis were carried out in a class 10,000 cleanroom. Most of the sample processing was taking place in the cleanroom of the University of St Andrews, while the remaining work was done in the cleanroom facilities of the University of York following relocation of the group. An optical microscope (Olympus BH2) was used for quick visual checks of the samples. The quality and geometrical characterisation was assessed with a surface profilometer (Veeco DekTak 150 at St Andrews) and a scanning electron microscope (SEM, Hitachi S-4800 at St Andrews, FEI Sirion S-FEG at York).

3.1 Material choice

I mainly used amorphous silicon (a-Si) as the grating material and silicon nitride membranes as the carrier. As deposition instruments for amorphous silicon were not available in-house, collaborators from Italy and Ireland performed the thin film deposition. The membrane windows were purchased commercially from Norcada Inc. Both material platforms are described in the following paragraphs.

3.1.1 Deposition methods of amorphous silicon

A thin film of amorphous silicon was deposited on microscope glass slides by three different methods: sputtering, electron-beam (e-beam) evaporation, and plasma-enhanced chemical vapour deposition (PECVD). At the start of my project,

I obtained sputtered a-Si samples from collaborators at CNR-IMM Catania, Italy. Later on, colleagues at Tyndall National Institute Cork, Ireland, provided a-Si samples deposited either by electron-beam evaporation or plasma-enhanced chemical vapour deposition. Amorphous silicon has an energy band gap larger than 1.7 eV [Bakr et al., 2011] compared to crystalline silicon (c-Si), whose band gap is at 1.12 eV [Tiedje et al., 1984]. The dielectric functions of c-Si and a-Si are also different and depend on the deposition technique and the resulting hydrogen content [Bakr et al., 2011, Lin et al., 1999]. For instance, it was found that, a-Si which was deposited with nearly double the flow rate of pure silane (SiH_4) had an index of refraction of $2.77 - j \cdot 0.01$ at a wavelength of $1 \mu\text{m}$, while the other had an index of $2.96 - j \cdot 0.01$ [Bakr et al., 2011]. For example, Figure 3.1 compares the dispersion and absorption of crystalline silicon (taken from reference [Filmetrics, 2014]) with that of amorphous silicon, which was characterised by spectroscopic ellipsometry by my colleague Dr Yue Wang (sputtered a-Si) and by collaborators at the University of Pavia, Italy (PECVD a-Si).

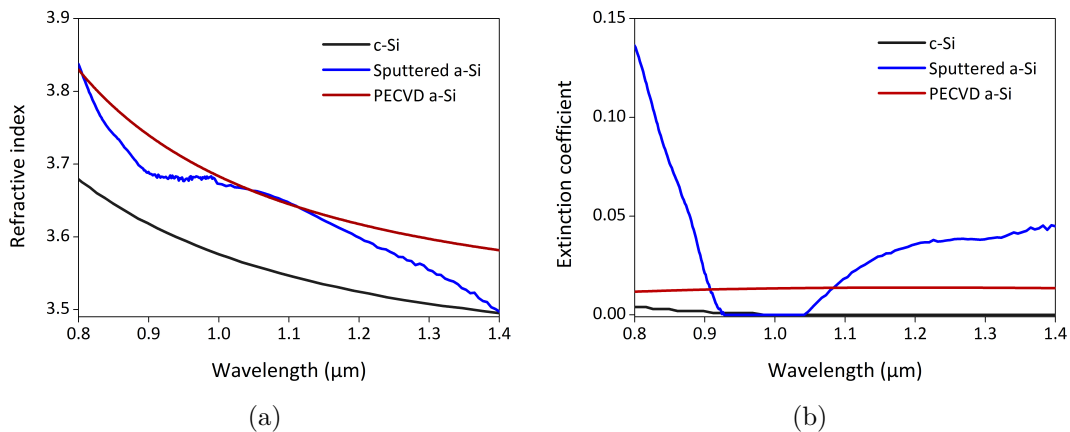


Figure 3.1: Refractive index n (a) and extinction coefficient k (b) for crystalline silicon (black lines) [Filmetrics, 2014] and amorphous silicon, deposited either by sputtering (red lines) or PECVD (blue lines), in the near-infrared spectral range.

The refractive index of a-Si is slightly higher than for c-Si. In particular, the index of a-Si deposited by PECVD is approximately 4% higher across the near-infrared wavelength range, which is in good agreement with values from the WVase database, while the agreement with the sputtered version is less satisfying. Similarly, the extinction coefficient is uniformly larger for PECVD a-Si than for c-Si; sputtered a-Si shows again larger deviations. We understand that these variations stem from a significant defect density on the surface of the material (see Figure 3.2c), thereby making the literature data less applicable. In addition, the different

process parameters involved in sputtering, e-beam evaporation, or PECVD contribute to significant fluctuations in the refractive index data due to the incorporation of different types of impurities. For example, sputtering is performed at temperatures below 100°C in an argon flow, while PECVD involves a mixture of argon and silane (and hence hydrogen) as the process gas, at temperatures of 200°C. In contrast, no external gases are used for e-beam evaporation while temperatures were at 80°C. My conclusion from this discussion is that the deposition techniques and their parameters have a large impact on the material parameters of the a-Si material.

3.1.2 Silicon nitride membrane

One of my goals was to build a tuneable optical MEMS Fabry-Pérot (FP) filter (see Chapter 7) that incorporates wavelength-scale high contrast gratings. The moveable part of the MEMS device is realised by a thin membrane, which forms one of the two reflectors of the FP cavity. We chose to apply the electrostatic attraction of both mirrors as tuning mechanism for simplicity and speed. Due to its combined advantages of robustness, flexibility, and compatibility with MEMS fabrication [Kurth et al., 2010], we chose a silicon nitride (SiN_x) membrane as the carrier. We used commercially available transmission electron microscopy windows from Norcada Inc. containing a square membrane area of $500 \times 500 \mu\text{m}^2$ on a total chip size of $7.5 \times 7.5 \text{mm}^2$. The substrate material was 750- μm thick silicon coated with a silicon nitride layer with a thickness of 100 μm , which was processed by liquid-phase chemical vapour deposition. Such a small thickness makes the membrane very vulnerable to stresses induced by processing and handling [Ekkels et al., 2003]. The index of refraction of silicon nitride n_{SiN_x} is moderately low in the near-infrared spectral range ($n_{\text{SiN}_x} \sim 2$). For usage as a broadband grating reflector, the membrane layer is too thin to provide coupling to guided-mode resonances. We therefore decided to coat the membrane with an amorphous silicon layer to act as the broadband reflector (see Section 4.1.2 of Chapter 4). Prior the deposition, several membranes were glued to a microscope slide carrier using polymethylmethacrylat (PMMA) and baked at 180°C on a hotplate for a few minutes. As mentioned above, our collaborators performed the deposition of amorphous silicon by sputtering (CNR-IMM Catania), electron-beam evaporation (Tyndall National Institute Cork), and PECVD (Tyndall National Institute Cork). A comparison between the uncoated membrane and the results of the different deposition methods is shown in Figure 3.2. The SEM image of the uncoated chip (Figure 3.2a) shows a smooth and very flat membrane window. Compared to that, the membrane samples that were deposited by electron-beam

evaporation (Figure 3.2b) and PECVD (Figure 3.2d) exhibited buckling and wrinkling effects as typically encountered under thermal stress conditions [Kim et al., 2004, Ziebart et al., 1999]. This is understandable for the case of the PECVD, where the chamber is heated to about 200°C, eventually leading to locally varying surfaces. As the temperature is only around 80°C for the electron-beam evaporation, however, the reason for the membrane deterioration could not be identified. Although the membrane area remained flat upon sputtering of a-Si (Figure 3.2c), the level of contamination in the a-Si material was very high leading to significant variations of the actual refractive index data (Figure 3.1). Due to all these uncertainties, we dropped the idea of coating the SiN_x membrane with a-Si at a later stage; instead, the flexible membrane side of the FP resonator was coated with metal to act as a mirror, while the inflexible side was coated with a-Si and patterned.

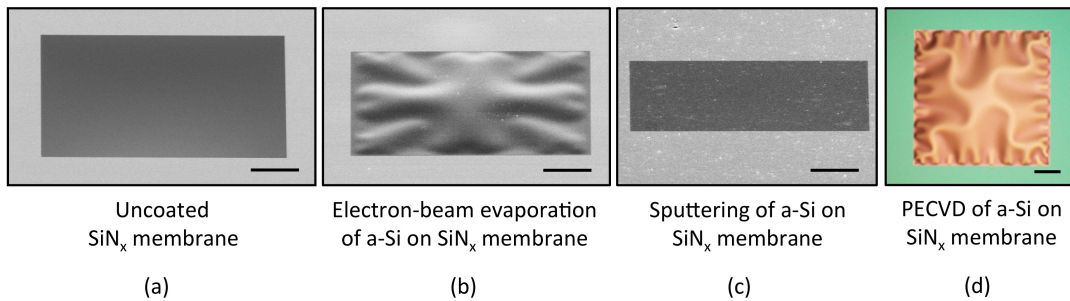


Figure 3.2: (a) SEM image of the uncoated silicon nitride membrane window (viewed at 60°). (b) SEM image of the buckled membrane after deposition of a-Si via electron-beam evaporation (viewed at 65°). (c) SEM image of the membrane window after deposition of a-Si via sputtering (viewed at 75°). (d) Optical image of the buckled membrane after PECVD of a-Si (top view). The black scale bar is 100 μm long.

3.2 Pre-treatment of sample

A crucial step prior to any processing and lithography is the cleaning of the sample, which in our case has typical dimensions of $1 \times 1 \text{ cm}^2$. In order to remove any organic or inorganic contaminants on the surface, the samples were treated with the chemicals acetone and isopropanol alcohol (IPA), if feasible with ultrasonic agitation, for a few minutes. In addition, organic residuals were removed with a so-called “Piranha etch” constituting a mixture of sulphuric acid (H_2SO_4) and hydrogen peroxide (H_2O_2) in a ratio of 3:1 for five minutes. After that, the samples were rinsed in acetone and isopropanol, blow-dried with nitrogen, and were ready for processing.

3.3 Lithography

The technique of transferring a pattern from a carrier onto the surface of a solid substrate is called lithography. Optical or photolithography was invented at the turn of the 18th/19th century and is the most widely used lithographic process for fabricating integrated circuits. Besides conventional photolithographic systems operating with ultraviolet (UV) radiation with resolutions in the sub-micron range, high-end extreme ultraviolet, x-ray or charged-particle beam lithographic instruments achieve accuracies well below 10 nm [Manfrinato et al., 2013]. The methods applied in this work were UV photolithography and the more complex electron-beam lithography (EBL). A typical lithographic procedure is illustrated in Figure 3.3 and explained in the following; it involves the steps of resist application, exposure using a mask containing the desired pattern, development, pattern transfer (etching), and removal of the resist.

Photolithography makes use of light-sensitive organic polymers, so-called photoresists, which are applied on the surface of the sample and can either be of the type “positive“ or “negative“, depending on their solubility in a solvent after exposure. EBL operates similarly and uses resists that are sensitive to electrons rather than electromagnetic radiation. In case of a positive resist, the radiation splits the polymer chains rendering them soluble when the developer solution is applied, i.e., exposed areas are removed and unexposed areas remain. The opposite chemical reaction happens for the negative resist whose polymer chains cross-link in regions exposed to the radiation; hence they remain insoluble when applying the developer whereas the unexposed polymer is washed away.

Photoresists and electron-sensitive resists can be applied on the surface of the sample by different methods. The most widely used technique, which was also used within this work, is spin coating (step 2 of Figure 3.3). The sample is placed on a rotatable vacuum-controlled chuck in a resist spinner and the resist is dispensed with a pipette onto the surface of the sample, which is then spun at a certain speed for a certain time. The resist fluid spreads out and thins down to a controllable and uniform film thickness. It is important to note that the ambient environmental conditions such as temperature, humidity, and air pressure have a large impact on the final result such as film thickness, uniformity, and general quality.

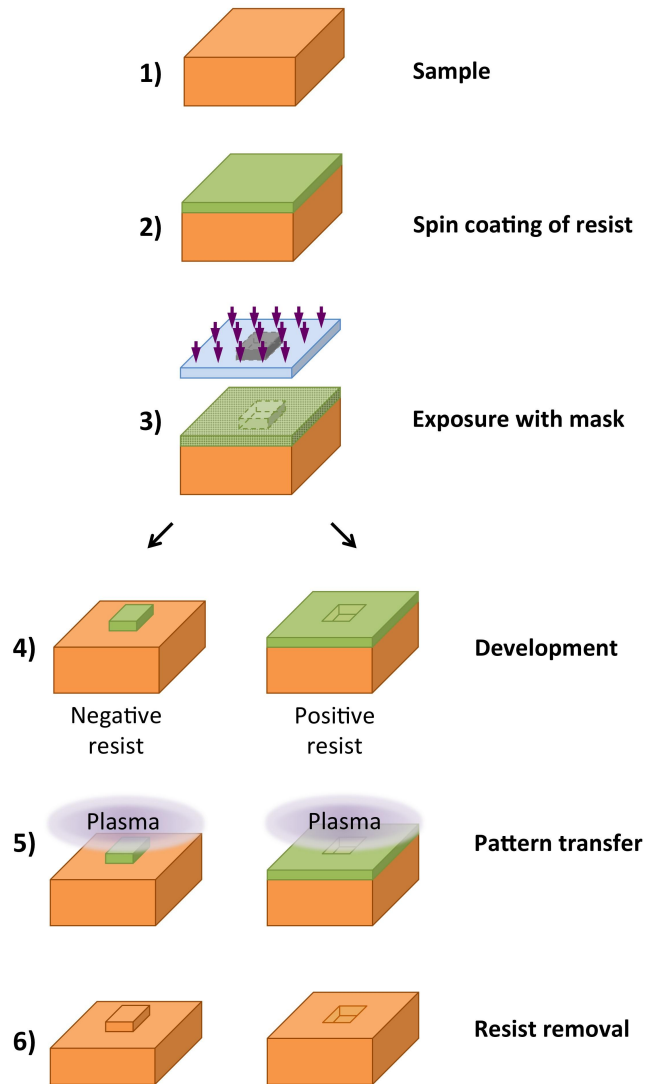


Figure 3.3: Processing steps during lithography and pattern transfer as explained in the text.

After spinning, soft-baking (or pre-exposure baking) is performed on a hotplate to evaporate any remaining traces of solvent. Then, the sample is positioned in the exposure system so that the image of the mask is transferred onto the resist (step 3 of Figure 3.3). In our case, the photolithographic system was a contact mask aligner system from Karl Süss (MJB-3, at St Andrews) with a mercury lamp operating at the near UV (around 365 nm) or a home-made UV tool (at York) utilising a UV-LED. Practically, with our photolithographic system we were able to resolve features of a few microns. The more complex exposure system and working horse used within this work was a 30 kV direct-write EBL instrument (LEO Gemini 1530 SEM/Raith

Elphy Plus at the University of St Andrews) with attainable resolutions well below 100 nm. Some final results were also obtained with a brand-new 50 kV EBL system (Raith Voyager at the University of York). I mainly used the electron-sensitive resists ZEP 520A (Zeon Chemicals) and PMMA 950K (MicroChem Inc.). Compared to the physical photomasks used in optical lithography, EBL uses a “software mask“ defined by a computer aided design software embedded in the EBL system. Furthermore, the electron beam, which is generated in a column and held in vacuum, is precisely shaped by complex electronics and focussed to a spot (few tens of nanometre in size) exposing the resist in a sequential (raster scan) rather than a parallel manner as in photolithography. Due to the shorter wavelengths of accelerated electrons, patterns with feature sizes well below the diffraction limit of light are possible. These advantages, however, come with some detrimental effects caused by scattering inside the resist and the substrate. In particular, forward scattered electrons produce a broadening of the beam inside the resist, while backscattering from the substrate into the resist causes an undesired exposure of the surrounding resist and hence a widening of the scanned area, which is commonly referred to as “proximity effect“. This undesirable effect gives rise to variations of the feature sizes in a pattern. We applied a software algorithm (NanoPECSTM) to perform a correction of the proximity effect. An example of a pattern with the corrected exposure doses used in this work is shown in Figure 5.7 of Chapter 5. Additionally, for the fabrication of a Fabry-Pérot filter as described in Chapters 6 and 7, multiple exposures were performed on the same chip while keeping an alignment precision of a few microns between them; therefore multilayer exposures with appropriate adjustments (three-point alignment) were carried out.

After exposure, a post-exposure bake is often used to complete the photochemical reactions. The next step is then the development of the resist, which selectively dissolves the resist (step 4 of Figure 3.3). The table below (Table 3.1) lists the relevant resists and their respective fabrication recipes used in this work.

Table 3.1: Overview of the resists and the fabrication recipes used.

Resist type	Photoresist	Ebeam	
	SU-8 (negative)	ZEP 520A (positive)	PMMA 950K (positive)
Spin-coating			
Speed (rpm)	Step 1: 750, step 2: 1500 step 3: 3000	3200	5000
Time (s)	Step 1: 10, step 2: 10 step 3: 60	60	60
Soft-baking			
Temp. (°C)	Step 1: 65, step 2: 95	180	180
Time (min)	Step 1: 2, step 2: 6	10	5
Exposure			
Dose	1) Mask aligner <70 mJ/cm ² 2) UV tool <30 mJ/cm ²	52 $\mu\text{C}/\text{cm}^2$	40 $\mu\text{C}/\text{cm}^2$
Time (s)	1) 45, 2) 960	Size dependent	Size dependent
Post-exposure baking			
Temp. (°C)	Step 1: 65, step 2: 95	-	-
Time (min)	Step 1: 1, step 2: 5	-	-
Development			
Developer solution	EC solvent	Xylene	3:7 DiH ₂ O:IPA
Time (s)	1) 10, 2) 240	45	45
Rinse solution	IPA	IPA	IPA
Hard-baking			
Temp. (°C)	180	-	-
Time (min)	5	-	-
Resist thickness			
Thickness (μm)	1) 7-13 2) 100	0.3-0.4	0.5-0.6
Resist stripping			
Solution method	1165 @60°C or O ₂ plasma etch	1165 @60°C or TCE or DMF	Acetone

The resist pattern then serves as a mask for the subsequent etching process that transfers the pattern into the solid substrate (step 5 of Figure 3.3). Our silicon-based materials are dry-etched using reactive ion-beam etching (RIE) with fluorine chemistry, i.e., trifluoromethane (CHF_3), sulfur hexafluoride (SF_6), sometimes diluted with oxygen (O_2). A reactive ion etcher uses a parallel-plate capacitor configuration, where a radio frequency (RF) field is applied between two electrodes to ionise the gases and generate plasma. A negative direct current (DC) voltage bias establishes due to the different mobility of the positively charged ions and the electrons, which results in a net acceleration of the ions towards the sample. The resist protects the areas of the sample that are not meant to be etched, but it needs to be thick enough and have sufficient etch resistance not to erode during the etching process. Our etching recipes for amorphous silicon and silicon nitride were optimised for perpendicular sidewalls and low roughness and are summarised in Table 3.2.

Table 3.2: Parameters for dry etching amorphous silicon and silicon nitride.

Material	Gas	Gas flow (sccm)	Pressure (mbar)	DC bias (V)	RF power (W)	Pre-conditioning (min)	Time (min)
a-Si	CHF_3	100	5×10^{-2}	-210	19	10	~ 2
	SF_6	100					
SiN_x	CHF_3	100	5×10^{-2}	-590	90	10	5
	O_2	25					

In the final step, the resist is stripped off the substrate by using commercial stripping solutions such as 1165 (MicroChem Inc.), acetone, trichlorethylen (TCE), dimethylformaldehyd (DMF), oxygen plasma, or a combination of these techniques for at least ten minutes up to one hour. For further fabrication details, the reader is referred to the comprehensive book about microfabrication by Madou [2012].

3.4 Lift-off and electron-beam evaporation of metals

An alternative method to etching is the “lift-off“ process, which is used if direct patterning is not as straightforward as in the case of metals. The patterning of metal was required for the realisation of the tuneable filter described in Chapter 7 as a means to perform both electrical conduction and optical reflection. The crucial feature in a

lift-off process is to achieve an undercut profile of the resist after the exposure (Figure 3.4b) and to generate a discontinuity in the thin film thereby allowing access of the solvent to the resist sidewall (Figure 3.4c). In this way, metal is coated in desired places between the resist walls while all remaining metal is lifted off during resist removal (Figure 3.4d).

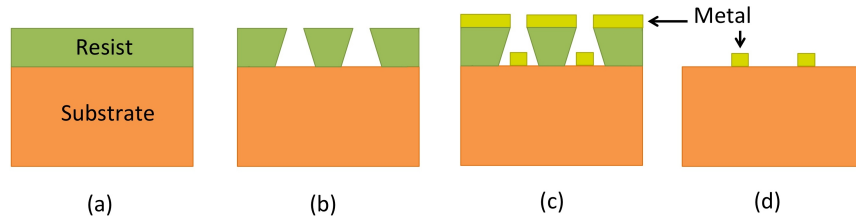


Figure 3.4: Process flow during lift-off. (a) Spin-coating of resist onto substrate. (b) Resist pattern after EBL performed at reduced acceleration voltage and subsequent development. (c) Evaporation of metal onto the sample. (d) Patterned metal structure after resist removal.

A rule of thumb identifies a 3:1 ratio of the resist and metal thickness as a successful setting for lift-off to take place. In our case, the feature sizes of the gold pattern varied between a few microns for thin wiring and hundreds of microns for contact pads and reflective areas, while thicknesses were between 10-100 nm. In addition, a 5-nm thin chromium layer was deposited prior to the gold coating to act as adhesion promoter between the gold and the substrate [Aouani et al., 2009]. The lift-off procedure was carried out with the EBL system using the electron-sensitive resist PMMA 950K. The undercut in the PMMA resist was achieved by reducing the acceleration voltage and the exposure dose of the EBL by one third to 10 kV and $18 \mu\text{C}/\text{cm}^2$, respectively, in order to enhance the electron scattering process. The deposition method I used to coat the patterned sample with gold was electron-beam evaporation (Edwards Auto 306 FL 400). In this process, an electron beam is focussed in vacuum on the target material (e.g., gold), which is melted and then condensed on the surface of the rotating sample while a quartz crystal monitor measures and displays the thickness and rate of the evaporating material.

3.5 Spacer definition and adhesive bonding

One aim of my work was to fabricate Fabry-Pérot filters containing high contrast gratings as their core elements. For the definition of the cavity length of the devices, bars or a frame of SU-8 (MicroChem Inc.) with an exactly specified thickness were

defined by photolithography (see Figure 6.9a in Chapter 6). Hereby, a ratio of 2:1 of a solution of the thicker SU-8 2050 to the thinner SU-8 2000.5 was spin-coated on one of the mirror samples of the filter. Due to the high viscosity of the SU-8 solution and the required layer thickness of around $10\ \mu\text{m}$, spin coating was performed in three consecutive steps with the speed and time being ramped up in each step to obtain a uniform spinning result. The low spin speed (750 rpm for 10 s) in the first step ensured a uniform spread of the viscous resist over the surface of the silicon chip, while the second spin step (1500 rpm for 10 s) removed any excess SU-8. The final distribution of the resist was performed in the third step (3000 rpm for 1 min). Similarly, pre- and post-exposure-baking were performed slowly at two different temperatures (60°C and 95°C) to avoid the formation of stress in the resist layer during the evaporation of the solvent. The processing steps are noted in Table 3.1. For simplicity, we used adhesive bonding [Niklaus et al., 2006] to mechanically connect two patterned substrates to build a Fabry-Pérot device, using tiny drops of thin SU-8 2000.5 as a glue. Depending on the alignment need, the two samples were either manually connected to each other or brought into contact in a controllable manner using the mask aligner. Thereafter, the sample baked on a hotplate at 60°C for 2 minutes while applying a small pressure using weights on top of the bonded elements. Next, the temperature was ramped up to 95°C and the sample block baked for another 5 minutes followed by the actual hard-bake at 180°C for 10 minutes. Finally, the heat was slowly decreased to avoid abrupt temperature changes (leading to cracks in the resist). The finished chip was then mounted on a printed circuit board (see Figure 7.10a in Chapter 7) for easier wiring and mechanical stability during subsequent measurements.

3.6 Microfluidic channels using PDMS

In some of my later work, I combined silicon-based optical elements with microfluidic devices. In order to create the microfluidic circuitry, I used soft-lithography methods [Xia and Whitesides, 1998], whereby a patterned structure is transferred to an elastomeric material by means of a mould [Duffy et al., 1998]. The most widely used elastomer in this process is polydimethylsiloxane (PDMS); PDMS is a well-established material for making microfluidic channels that has previously been developed by other students [Ashok, 2012, Scullion, 2013]. In particular, I used PDMS to provide a microfluidic channel above an array of high- NA diffractive lenses to trap micron-scale particles in an optical tweezer setup (see Figure 5.20 in Chapter 5). All microfluidic devices were fabricated in the cleanroom facilities at York and contained the following

steps as shown in Figure 3.5: a) generation of the mould using photolithography, b) silanisation of the sample, c) soft-lithography using PDMS, d) cutting to final size and punching of access holes, e) bonding of the PDMS block to the sample under study and attachment of tubes.

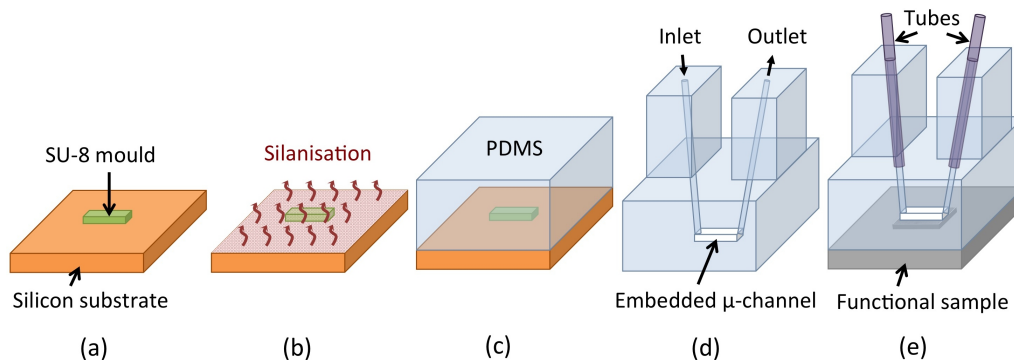


Figure 3.5: Process flow for making microfluidic channels on a functional sample using soft-lithography. (a) UV-patterned SU-8 mould on a cleaved silicon sample. (b) Silanisation of the surface of the patterned sample. (c) Curing of PDMS on top of the mould. (d) Attaching additional PDMS blocks and punching access holes to the PDMS microchannel system. (e) Bonding the PDMS system on top of a functional sample and adding tubes.

In the first step, a master mould made of the highly viscous negative resist SU-8 2050 was fabricated on a $4 \times 4 \text{ cm}^2$ cleaved and cleaned (in acetone and IPA) piece of silicon wafer by UV photolithography (Figure 3.5a). The resist was poured onto the silicon chip and spin-coated at 1500 rpm for 1 minute to obtain a thickness around $100 \mu\text{m}$. A two-step pre-exposure bake on a hotplate followed for 5 min at 65°C and for 25 min at 95°C . After a 5 min cool-down of the sample, it was exposed for 16 min with the UV tool using a printed mask with a transmissive window of size $10 \times 5 \text{ mm}$, which defined the cross-sectional dimensions of the microchannel. During the exposure, the printed mask was kept flat by temporarily bonding it to a quartz plate using a drop of water. Thereafter, the exposed resist was post-baked for 3 min at 65°C , for 15 min at 95°C , and cooled down. At this time, the desired channel pattern was already recognisable and was fully developed after applying EC solvent for 4 min and rinsing it in IPA. The SU-8 stamp was finalised by a 2 min bake at 95°C on a hotplate and by hard-baking it for at least 4 hours at 180°C in a convection oven. The cooled silicon chip containing the SU-8 mould was silanised (Figure 3.5b) for 1 h using a drop of trichlorsilane (FluorChem) in a desiccator to provide a non-sticky layer on the sample making it easier to peel off the elastomer from the mould. Now the actual soft-lithographical procedure commenced. A 10:1.3 PDMS mixture of a base and a curing agent (Dow Corning Corporation) was prepared by volume. A de-gassing

procedure for at least 30 min in the desiccator ensured that any remaining bubbles in the PDMS were removed. In a next step, the PDMS mixture was carefully poured onto the SU-8 mould, which was placed inside a Petri dish until its thickness was set to about 5 mm (Figure 3.5c); at this stage another degassing step was not necessary. The whole setting was then cured for 3 h in an oven at 60°C. After the silanisation process, the PDMS could easily be peeled off from the mould. The PDMS base piece was cut to size with a sharp knife to match the size of the sample. As the base piece would be too thin to hold any inlet/outlet tubes in place, its thickness was increased by glueing two PDMS blocks on top on either sides of the embedded microfluidic channel by using some liquid PDMS and baking the whole sample at 100°C for 2 min on a hotplate. Punching holes through both the bonded PDMS blocks and the PDMS base piece using a micro-punch (Harris) with a diameter of 2 mm created the access ports to the microchannel (Figure 3.5d). Finally, the PDMS microchannel system was bonded to a sample containing the desired optical function (e.g., a microlens focussing light into the microfluidic channel, see Chapter 5 for details) and the tubes were attached (Figure 3.5e). For the bonding process of the PDMS chunk to the functional sample, a mixture of two parts of curing agent and one part of base agent was used as a glue and spun at 3000 rpm for 1 min onto a clean glass cover slip. The PDMS chunk with the microchannel facing down was dipped into the spun layer and subsequently glued onto the functional sample, thereby positioning the channel manually on the optical structure of the sample. A last bake of the bonded device at 60°C for at least 1 h and the attachment of the tubes into the holes completed the procedure. A liquid could then be fed into the tubes with a syringe to establish a flow through the microchannel.

4 Broadband grating reflector

This chapter describes the design, fabrication, and experimental analysis of broadband mirrors based on wavelength-scale high contrast gratings made of amorphous silicon (a-Si). The gratings are one-dimensionally periodic. Section 4.1 presents the material aspects and explains the rigorous coupled-wave simulation used for the design, while Section 4.2 describes the fabrication details, and Section 4.3 the optical characterisation. Some of the characterisation was conducted in-house and some was conducted by our collaborators at Tyndall National Institute, Cork, Ireland as part of a project secondment.

4.1 Material

High contrast gratings have been proposed by a number of groups [Mateus et al., 2004, Shokooh-Saremi and Magnusson, 2008a] to complement or replace multilayer Bragg mirrors. In particular, the group of C. J. Chang-Hasnain at Berkeley, USA, has experimentally demonstrated the use of high contrast gratings in VCSELs at 850 nm [Chang-Hasnain, 2011, Zhou et al., 2008] and at 1.55 μm [Karagodsky et al., 2010a]. The motivation behind using broadband mirrors based on HCGs is their lightweight nature, as they only require a single layer thin film, which reduces the mirror mass and increases the resonance frequency for high-speed tuneability. Silicon is widely used for HCG mirrors because of its high refractive index, high optical quality, and its mature technology. We use amorphous silicon, because it can be deposited relatively easily to a given thickness. Some of the material used here was deposited at the Tyndall National Institute in Cork, Ireland in the framework of the PROPHET collaboration, while the other was coated at CNR-IMM Matis in Catania, Italy. I used two types of samples in my experiments; sample 1 consisted of amorphous silicon deposited on glass, while sample 2 consisted of amorphous silicon deposited on a 100 nm thin silicon nitride membrane. As both samples were fabricated in a different time frame, the deposition methods for them were also varying. Sample 1

was deposited by plasma-enhanced chemical vapour deposition (PECVD, at Cork) on a glass substrate and sample 2 was deposited by sputtering (at Catania) onto a silicon nitride membrane (see Figure 3.2c in Chapter 3). From a design and a fabrication point of view, a thickness around 300 nm of a-Si was identified as being both straightforward to etch and very suitable for HCG reflector operation, for operation around 1 μm wavelength. Depending on the deposition method and fluctuations during the deposition process, however, the thickness of the a-Si layer varied between 260 nm and 360 nm. The details relating to the different deposition methods have already been described in the fabrication chapter (Chapter 3).

4.1.1 PECVD amorphous silicon on glass substrate (sample 1)

An important part of the investigation is to establish the practical limitations of amorphous silicon as a reflector because of its low but non-negligible absorption around a wavelength of 1 μm as obtained from the ellipsometry measurements of PECVD a-Si on glass, which are shown here again for reference (Figure 4.1b). In addition to the grating geometry (Figure 4.1a), Figures 4.1c-f show the diffraction efficiency of the zeroth reflected order (in the following also referred to as “normalised reflectivity”) for a grating with a 285 nm thick layer of PECVD a-Si designed for broadband reflection in the near-infrared range, normal incidence, and TM polarisation. The grating period was 470 nm and the duty cycle 0.75. In Figures 4.1c and 4.1e, only the refractive index variation with wavelength was included, while Figures 4.1d and 4.1f include both refractive index and absorption variation of PECVD a-Si. Altogether, the calculations converged quickly after 12 iterations. Without considering absorption, the grating mirror reaches a reflectivity above 0.985 over a spectral bandwidth of 330 nm and a reflectivity above 0.95 over 429 nm around a wavelength of 1 μm (Figure 4.1c), which is quite remarkable. Numerous contributions [Almuneau et al., 2011, Chung et al., 2010, Ricciardi et al., 2010] indicate such a near-unity reflectivity for silicon in this spectral range. When adding absorption, which clearly exists in the PECVD a-Si material, this value drops to around 113 nm for reflectivities higher than 0.95 (Figure 4.1d). To illustrate the origin of the broadband reflectivity, Figures 4.1e and 4.1f show the spectral response of the amorphous silicon-based periodic grating on glass by taking into account the dispersion only and both the dispersion and absorption of the PECVD a-Si material, respectively.

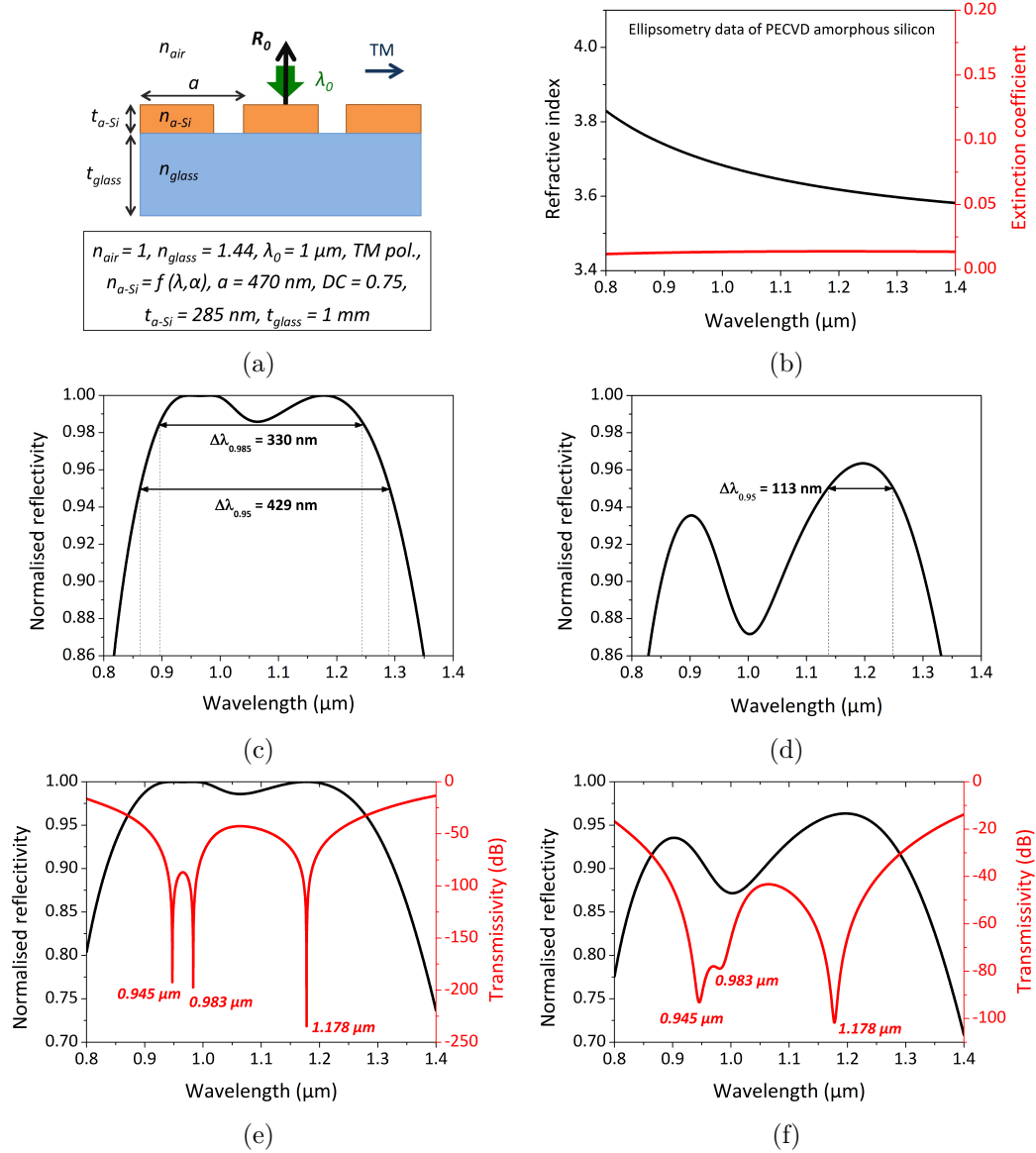


Figure 4.1: (a) Grating geometry and parameters used in the RCWA simulation for high and broadband reflectivity; n_{a-Si} was taken as a function of wavelength λ and absorption α . (b) Refractive index and extinction coefficient of PECVD a-Si obtained by ellipsometry. (c) Diffraction efficiency of the zeroth order of a broadband mirror made of a high contrast grating with parameters as stated in (a), which was optimised for normal incidence operation without including absorption. The reflectivity remains above 0.985 across a bandwidth of 330 nm and above 0.95 across 429 nm. (d) Same simulation as in (c) with absorption included. The spectral band above a reflectivity of 0.95 is 113 nm. (e) and (f) Spectral responses and origin of the broadband resonance effect of the grating by showing three guided-mode resonances in close proximity to each other around the target wavelength of 1 μm and taking into account (e) only the dispersion of a-Si and (f) both the dispersion and absorption of a-Si.

There are three guided-mode resonances at 0.947, 0.983, and 1.178 μm at which the diffraction efficiency is unity, which can clearly be identified as transmission dips in the logarithmic transmission plot (green lines). Owing to their spectral proximity, the three resonances merge to give a broadband response in reflection. Due to absorption, the resonance dips are broadened, which is clearly evident by comparing both graphs. In the discussion that follows, the absorption of the amorphous silicon is always taken into account. A parameter scan around the optimum grating parameters of $a=470$ nm, $DC=0.75$ and $t_{a-Si}=285$ nm is shown in Figure 4.2. The white dashed line in each of the plots marks the cross section as shown in Figure 4.1d.

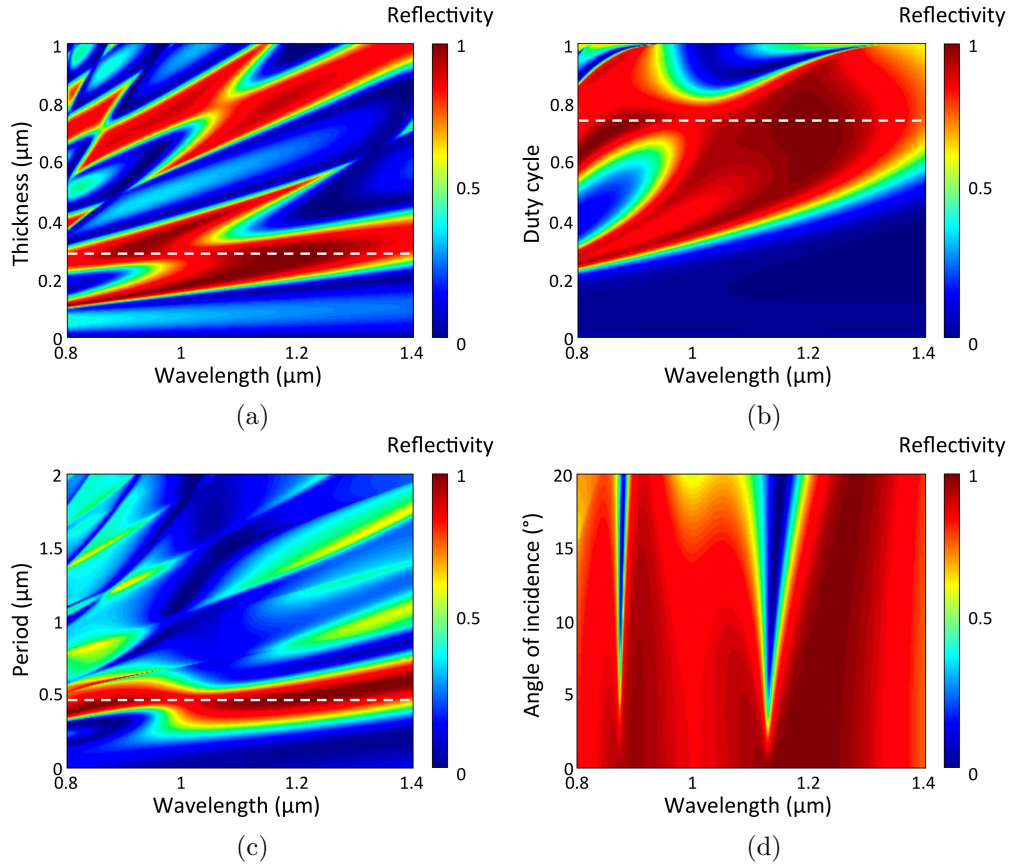


Figure 4.2: (a) Reflectivity vs. silicon thickness and wavelength. (b) Reflectivity vs. duty cycle and wavelength. (c) Reflectivity vs. periodicity and wavelength. (d) Reflectivity as function of the angle of incidence and the wavelength. The white dashed lines in (a)-(c) denote the respective design parameter for which the reflectivity is maximised.

The white dashed lines in Figures 4.2a-c indicate the parameters for which the reflectivity is maximal and broadband. The wide spectral band for the thickness of 285 nm is caused by the close proximity of three guided-mode resonances at 0.947,

0.983, and 1.178 μm , as highlighted in Figure 4.1. From the reflection map as a function of thickness and wavelength (Figure 4.2a), another wide reflective band is apparent at a grating thickness of approximately 780 nm. Its spectral width of about 300 nm is smaller and the reflectivity reduced compared to that at 285 nm. The variation of the duty cycle (Figure 4.2b) shows a high reflective band at around 1.2 μm for which a large fabrication tolerance exists. Less tolerance is expected from a change in the periodicity (Figure 4.2c). In fact, the wavelength of interest can be lithographically tuned by variation of the grating period while keeping all other grating parameters the same. The angular tolerance of the 1D grating is limited to near-normal incidence ($\sim 2^\circ$), after which the grating response changes significantly with steadily increasing transmission dips across the reflection band (Figure 4.2d). These sharp dips are due to odd and high-Q Bloch modes propagating in the grating plane that cannot be excited at normal incidence for symmetry reasons [Lalanne et al., 2006]. In conclusion, although the absorption of PECVD amorphous silicon in the near-infrared region is considered very low, it has a significant effect on the practically achievable reflectivity and spectral bandwidth - even under optimum fabrication conditions (i.e., every simulated grating parameter is exactly reproduced) the maximum reflectivity is above 95% for a moderate bandwidth of 113 nm.

4.1.2 Sputtered amorphous silicon on silicon nitride (sample 2)

An amorphous silicon grating on a silicon nitride membrane (Figure 4.3a) is of interest for MEMS applications as will be discussed in Chapter 7. As sputtered a-Si was used here, the ellipsometry data obtained by Dr Yue Wang were applied in the RCWA simulation and are shown here again for reference (Figure 4.3b). The tolerance in the design of the structure is shown next by modifying one of the grating parameters, while keeping the others constant (Figures 4.3c-f). Although the design parameters are different in this grating and an additional lower index layer exists below the grating, the RCWA graphs show similar reflectivities and grating tolerances as for the PECVD a-Si on glass substrate. In Figure 4.3c, at the optimal grating thickness of 330 nm a flat section is apparent, where the reflectivity stays above 97% across a bandwidth of almost 100 nm. If lower reflectivities $>90\%$ were allowed for a specific application, the band could be increased to 151 nm. A change in duty cycle results in a few high reflective bands around 1 μm , whereby the tolerance is highest for a duty cycle around 0.65 (Figure 4.3d).

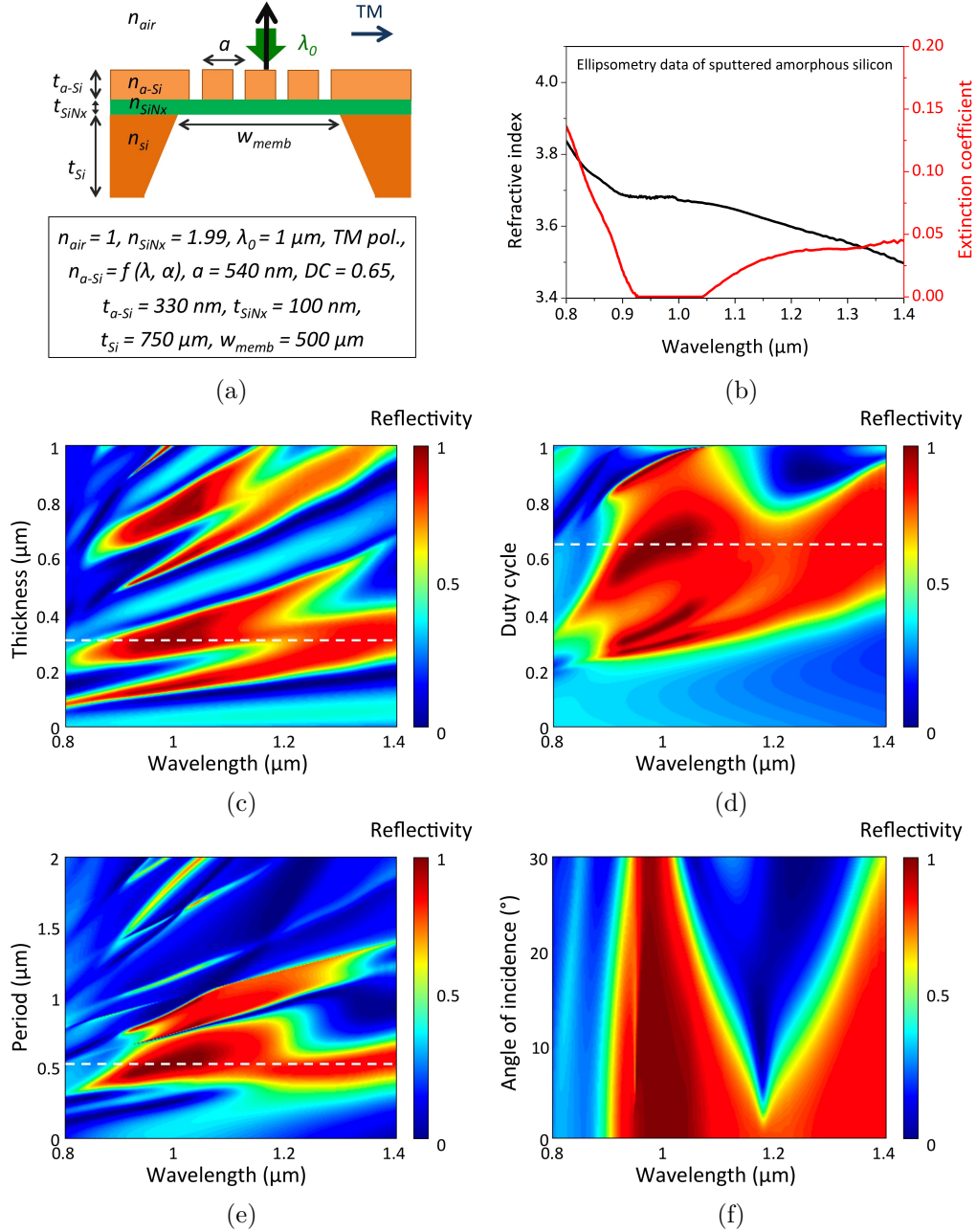


Figure 4.3: (a) Grating geometry with the optimal parameters for normal TM-polarised incidence at 1 μm . (b) Refractive index and extinction coefficient of sputtered a-Si obtained by ellipsometry. (c) Reflectivity vs. grating thickness and wavelength. (d) Reflectivity vs. duty cycle and wavelength. (e) Reflectivity vs. periodicity and wavelength. (f) Reflectivity vs. angle of incidence and wavelength. The white dashed lines in (c)-(e) denote the respective design parameter for which the reflectivity is maximised.

Similarly, a broad reflectivity band is also apparent from Figure 4.3e, and a second narrower section develops at grating periodicities around 900 nm. In opposition to the angular limitation to about 2° for the a-Si/glass sample, the a-Si/SiN_x grating geometry allows for incidence angles up to 20° until the bandwidth has dropped by half without significantly decreasing the reflectivity below 97% (4.3f). Due to absence of absorption at wavelengths between 0.93 and 1.05 μm , we expect to attain ultra-high reflectivities experimentally in that range.

4.2 Fabrication of broadband mirrors

The grating mirror design was simulated using RCWA and the resulting parameters transferred via the embedded CAD tool into the electron-beam lithography (EBL) software. The key technology steps for making grating mirrors are electron beam lithography and dry etching. The samples were cleaved to size and cleaned in acetone and isopropanol in a very low power ultrasonic bath, followed by a Piranha clean for 5 min. The electron-sensitive resist ZEP 520A was spun at 3000 rpm and hard-baked for 10 min at 180°C , resulting in a film thickness of 340-370 nm. The optimal exposure dose during e-beam lithography was $44.2 \mu\text{C}/\text{cm}^2$ with the 30 kV EBL system at St Andrews. Following a developing step of 45 s in Xylene and a dip-rinse in IPA, the pattern transfer into the amorphous silicon layer is performed by reactive ion etching using the etching parameters as stated in Section 3.3 of Chapter 3. The etching time varied between 1 min 45 s and 2 min 15 s depending on the actual thickness after a deposition batch. In the final step, the remaining resist is stripped off with the removing solvent 1165. Figure 4.4 shows the scanning electron microscope images of both types of fabricated broadband mirrors, either PECVD a-Si on the glass substrate or sputtered a-Si on the silicon nitride membrane. On inspection, we note that the period was within 5 nm of the design value, while the duty cycle varied by 5%, i.e., the widths of the silicon ridges deviated by approximately 20 nm. This larger deviation is due to the nature of electron-beam lithography, where the period is accurately determined by the positioning of the beam while duty cycle depends on exposure dose, resist thickness, and development conditions. We also note the larger roughness in the sputtered material as compared to the PECVD a-Si.

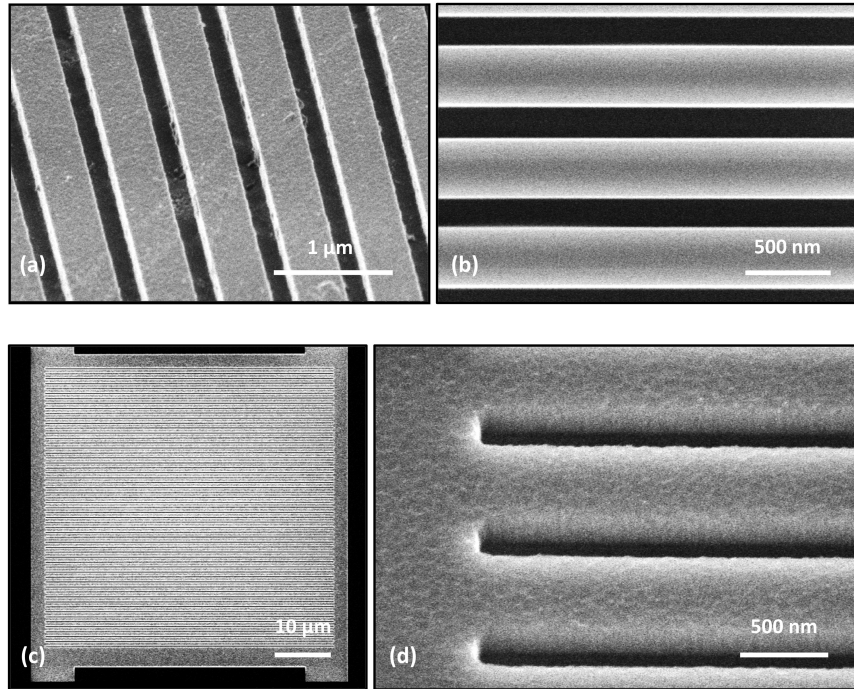


Figure 4.4: Scanning electron micrographs of the fabricated mirrors. (a) Uniform broadband mirror of a-Si on glass (sample 1) viewed at 60°. (b) Top view of the mirror in (a). (c) Periodic reflector of sputtered a-Si on silicon nitride membrane (sample 2). (d) The mirror in (c) viewed at an angle of 45°.

4.3 Characterisation of broadband mirrors

The reflectivity of the two types of broadband mirrors is measured next using two different optical setups.

4.3.1 Reflectivity measurement of sample 1

Through the collaboration and a secondment with our project partner Tyndall National Institute at Cork, Ireland, I characterised broadband mirrors based on evaporated amorphous silicon on glass in their reflection setup. The setup was built by Dr Tomasz Piwonski, who also assisted me in the measurements. A silver mirror (Thorlabs, PF07-03-P01) was used for reference. The gratings' reflectivity was studied both in TM and TE polarisation. The setup made use of a lock-in amplifier (Signal Recovery 7265) for better noise filtering. The setup is sketched in Figure 4.5.

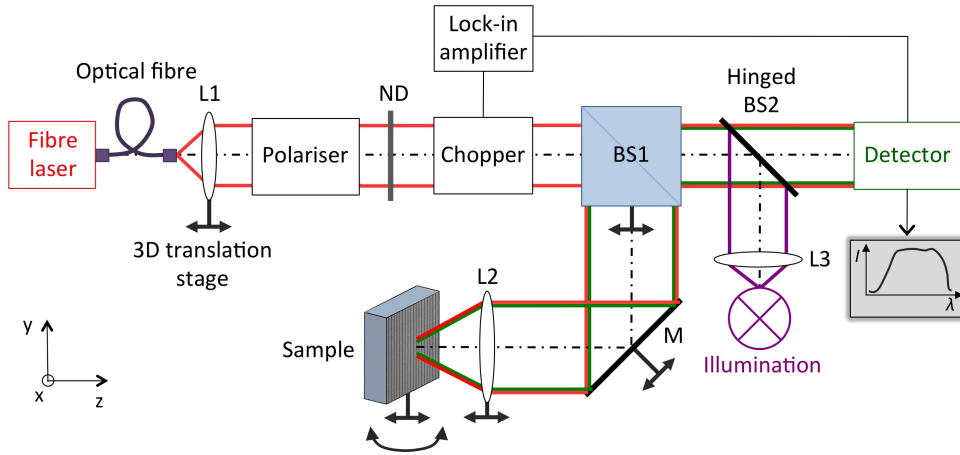


Figure 4.5: Reflection setup at Tyndall. L = lens, ND = neutral density filter, BS = beam splitter, M = mirror, ray traces in red denote incoming radiation, rays in green mark reflected radiation as recorded by the detector, purple rays show ray traces of the illumination light. The dashed black line through the optical components indicates the optical axis.

Here, the light source was a polarised fibre laser (Fianium) emitting a band from 650 to 1000 nm. The polarisation state was found by maximising the optical power with the help of a reference polariser. The beam was collimated by a lens (L1) and passed through a neutral density (ND) filter, a chopper (Stanford Research Systems Inc.), which was connected to the lock-in amplifier, a first beam splitter (BS1), a mirror (M), and a converging lens (L2) before hitting the sample. The sample was mounted on a rotation stage, which also allowed for three-dimensional positioning, and was adjusted such that the incoming polarisation was either TM or TE polarised radiation. Generally, most optical elements were mounted on 3D translation stages for convenience of alignment. A home-made detector recorded the back-reflected signal. All signal acquisition using the lock-in amplifier and the detector was controlled by a LabVIEW interface. The possibility to open an illumination path (via the hinged beam splitter BS2) and replace the detector with a CCD camera (Infinity 2) was an additional feature to check the location and shape of the beam on the sample. The measurements including the actual fabrication values are shown in Figure 4.6.

The experimental curves deviate from the theoretical graphs shown in Figure 4.1 due to a different grating thickness and slight changes in the period and duty cycle; SEM inspections of the fabricated gratings provided the actual parameters for the RCWA simulations to approximate the measured curves. The correspondence between experimental and calculated data is good although the data were approximated with the dispersion and absorption values of PECVD a-Si. For

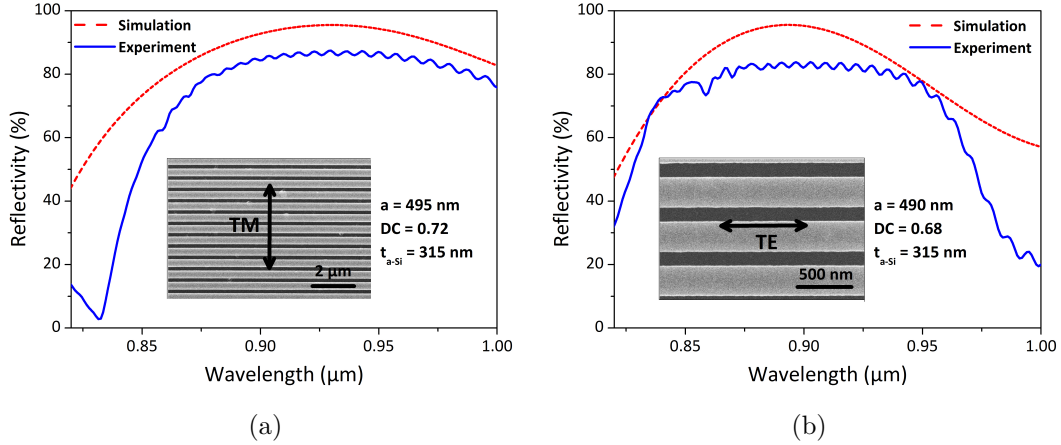


Figure 4.6: Measurement and simulation of the reflectivity spectra of an a-Si grating on glass for (a) TM polarisation and for (b) TE polarisation. The RCWA simulation was performed with the following parameters: (a) $a=495$ nm, $DC=0.72$, $t_{a-Si}=315$ nm; (b) $a=490$ nm, $DC=0.68$, $t_{a-Si}=315$ nm; both at normal incidence, $n_{glass}=1.44$, with dispersion and absorption of PECVD a-Si taken into account.

TM polarisation, we measured reflectivities $>85\%$ across a bandwidth of 80 nm, while we obtained reflectivities $>80\%$ across 110 nm for TE polarisation. The small ripples in the measurement originate from Fabry-Pérot resonances of the glass substrate. Besides the voids present in the a-Si deposited by e-beam evaporation, we believe that the limit in the achieved reflectivities is set by higher losses caused by the different deposition technique. Additionally, as the grating thickness was deviating by 10-15% in each deposition step, the initial thickness of 285 nm for which reflectivities above 90% around 900 nm were predicted was never attained.

4.3.2 Reflectivity measurement of sample 2

Sample 2 was measured with a reflection setup (Figure 4.7), which already existed in the group. It is mainly based on free-space optical elements; a fibre-coupled optical spectrum analyser (OSA, Advantest) is used to collect the signal. The beam of a broadband white light source (WLS, LEUKOS SM-30) was transmitted through an optical fibre via two microscope objectives (L1, L2), polarised, and focussed with a 20x microscope objective (L3). A gold mirror of known reflectivity (Thorlabs, PF07-03-M01) served as the reference sample for the measurement. The sample orientation was aligned with the grating ridges perpendicular to the incoming electric field vector in order to establish TM-polarised incidence; i.e., if the polariser was oriented in the x direction, the grating ridges were aligned with the y direction.

To help alignment, an auxiliary amplified spontaneous emission (ASE) source was launched from the detecting side to overlap the ray paths of incoming and detecting beam. Most of the components were mounted on three-dimensional translation stages to provide accurate adjustment. The reflected signal was recorded after passing twice through the beam splitter (BS) to a focussing lens (L4) and a fibre-coupled optical spectrum analyser (resolution 0.1 nm).

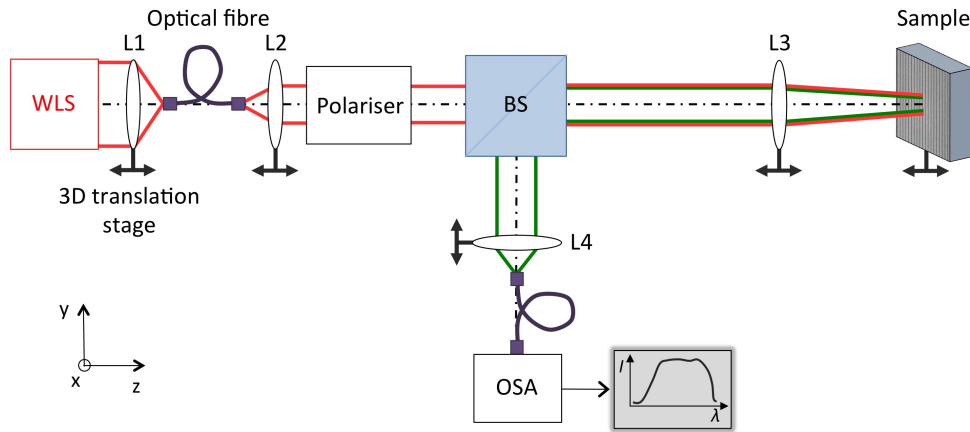


Figure 4.7: Reflection setup. WLS = white light source (supercontinuum), L = lens, OSA = optical spectrum analyser, red ray traces denote incoming radiation, green rays mark the reflected radiation as detected by the optical spectrum analyser. The dashed black line indicates the optical axis.

The high reflectivity of crystalline silicon in the near-infrared regime has been demonstrated in our group before [Ricciardi et al., 2010]. Here, the sample under study consisted of a suspended layer of approximately 330 nm of amorphous silicon sputtered onto a 100 nm thin silicon nitride membrane - an initial test sample for the development of a tuneable filter as shown in Chapter 7. The substrate of the membrane sample was silicon. The design was optimised for a wavelength of $1 \mu\text{m}$, normal incidence, and TM-polarisation (Figure 4.8). A high reflectivity $>97\%$ was recorded around the target wavelength of $1 \mu\text{m}$, specifically between 0.9 and $1.07 \mu\text{m}$. Also, a good overall agreement between measured and calculated values was found by including the actual grating dimensions after fabrication in the simulation. As small deviations in angle allow coupling to high-Q guided-mode resonances [Lalanne et al., 2006], the measured dips at around 0.95 and $1.18 \mu\text{m}$ can be attributed to angle variations within the measurement setup as verified by the two nearby dips in the simulation, taking into account an angle of incidence of 2° . The reason for the broader dips in the experiment compared to the simulated ones is the imperfect collimation of the incident beam during the measurement resulting in a higher amount of energy

concentrated near normal incidence and therefore in a slightly larger angular spectrum of incidence. A check of the extinction coefficient of the sputtered material (Figure 4.3b) reveals that the absorption is zero between $0.93 \mu\text{m}$ and $1.05 \mu\text{m}$, thereby explaining the near-unity measured reflectivity (99% at $1 \mu\text{m}$).

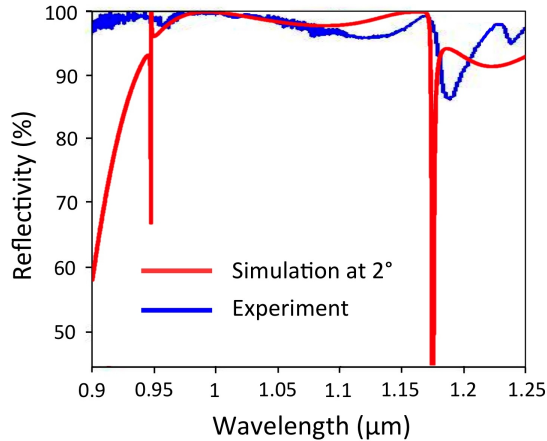


Figure 4.8: Measured and simulated reflectivity of a periodic a-Si HCG on a silicon nitride membrane for TM polarisation. The grating parameters used in the RCWA simulation were: $a=540 \text{ nm}$, $DC=0.7$, $t_{a-Si}=330 \text{ nm}$, incidence angle of 2° .

4.4 Summary

This chapter described the design of wavelength-scale high contrast gratings of amorphous silicon using RCWA simulations, their microfabrication, and experimental characterisation. Two different a-Si materials have been used, which were either sputtered or deposited by PECVD by collaborators at Catania or Cork, respectively. The best-measured reflectivity for PECVD a-Si on glass substrate was approximately 85% at a wavelength of 900 nm, which remained this value across a bandwidth of approximately 80 nm. In contrast, we demonstrated more than 97% reflectivity across 170 nm centred around a wavelength of $1 \mu\text{m}$ for sputtered a-Si on SiN_x membrane. We attribute the discrepancy in the results to the different properties in the a-Si material. In the case of sputtering, the ellipsometry data revealed zero absorption between 0.93 and $1.05 \mu\text{m}$ and a slight absorption outside that range, whereas for PECVD a non-negligible absorption persisted for the whole spectral range considered between 0.9 and $1.4 \mu\text{m}$. We conclude that the deposition method has a major influence on the quality of the amorphous silicon, which in turn eventually limits the attainable broadband reflectivity.

So far, I have considered 1D periodic high contrast gratings of infinite extent. In practice, wavelength-scale gratings have a finite size just as the incident beams, which causes some alterations near the boundaries, and reduces the efficiency of operation [Bendickson et al., 2001, Boye and Kostuk, 2000]. On the other hand, a minimum number of periods (several tens of periods) and length of the grating fingers (tens of microns) have to be maintained in order to keep reflectivity high. For instance, Faraji et al. [2006] have studied a suspended gallium arsenide grating mirror with a reflectivity of 99.9% and found that the minimum number of periods should be at least 50 and the length of the grating fingers above 20 μm to retain this reflectivity value. Similar results were obtained by Bisailon et al. [2006] with the same reflector geometry, i.e., at least 40 periods were necessary to keep reflection above 98%.

Furthermore, breaking the periodicity and chirping the grating parameters brings about new functionality, as I will explore in Chapter 5; in fact, the interplay between the guided modes of the grating layer and the radiation modes can be utilised to obtain flat focussing reflectors or flat transmissive lenses. In particular, the guided modes in the gratings with a high index contrast tend to have a very short in-plane propagation length [Fattal et al., 2010]. This means that the amplitude and phase of the reflected or transmitted waves can be controlled in a very localised region, and one can impose an almost arbitrary phase profile across the grating structure by locally changing the grating parameters such as period and filling fraction. Examples for imposing such an arbitrary phase profile for the purpose of designing lenses will be explored in the next chapter.

5 Planar diffractive lens with high numerical aperture

Upon giving the overview of existing microoptical systems in Chapter 2, this chapter explains how to engineer the wave front of a beam with a new type of flat diffractive lens based on silicon high contrast gratings with a two-dimensional spatial variation (Section 5.1). This section covers focussing reflectors composed of non-periodically sampled high contrast gratings. Furthermore, it includes a performance study of the focussing properties, considering the effect of silicon thickness, wavelength, angle of incidence, and the range of numerical apertures feasible for these reflective grating lenses. Sections 5.2 and 5.3 describe the fabrication and optical characterisation of such flat microlenses. An application example is the demonstration of optical tweezing with large-scale grating lens arrays in Section 5.3. At the end of this chapter, Section 5.4 highlights and summarises the most important findings. The results arising from this chapter have been published in references Klemm et al. [2013] and Klemm et al. [2014].

5.1 Design of high contrast grating lenses

The focus of my work is to develop planar diffractive elements with focussing capabilities on silicon. The work is concentrated on reflective and polarisation dependent components operating in the near-infrared spectral regime. Achieving a high numerical aperture is of particular interest, both for achieving a small focal spot and for realising optical trapping applications.

5.1.1 Key criteria

In order to describe the performance of a diffractive lens, I use the following parameters:

1. D is the diameter of the lens.
2. The numerical aperture NA is given by the angle between the outermost ray contributing to the focal point and the optical axis. Following simple geometrical rules, this can be described as:

$$NA = n \cdot \sin \left[\tan^{-1} \left(\frac{D}{2f} \right) \right] \quad (5.1)$$

Herein, n is the refractive index of the medium between the lens and the focal point, D the lens diameter, and f the focal length.

3. We define the axial resolution z_{ax} as:

$$z_{ax} = \frac{\lambda_0}{NA^2} \quad (5.2)$$

It depends linearly on the free space wavelength λ_0 and the inverse square of the numerical aperture NA .

4. The theoretical diffraction limit d_{lim} of an Airy pattern is given by:

$$d_{lim} = 1.22 \frac{\lambda_0}{NA} \quad (5.3)$$

5. The diffraction efficiency DE is defined as the energy in the focal spot relative to the incoming energy that passes through the surface of the lens. We define the focal spot as the region for which the intensity is down to $1/e$ of its maximum value.
6. Another parameter is the ease of fabrication of the lens, which describes complexity, cost, compatibility with standard processing techniques, and robustness. For example, planar microfabrication processes are preferred as very high optical uniformity can be achieved across the entire lens surface while avoiding critical multiple alignment steps during resist exposure.

7. For imaging applications, the modulation transfer function (MTF) of a lens is an important performance parameter. It gives a measure of the lens' ability to pass the spatial frequencies and thereby to transfer contrast from the object to the image plane and is formally defined by the following ratio of the maximum and minimum intensities:

$$MTF = \frac{I_{max} - I_{min}}{I_{max} + I_{min}} \quad (5.4)$$

In summary, our key criteria to make an efficient flat diffractive lens are:

- Providing full control over the phase
- Ease of fabrication
- Large numerical aperture
- High diffractive efficiency
- Planarity
- Diffraction-limited spot size

The following sections describe the approach and experimental methods of how to fulfil these criteria.

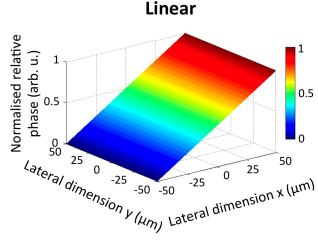
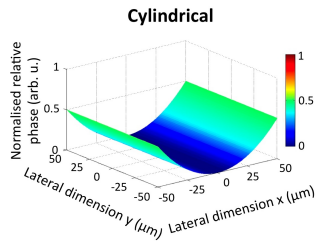
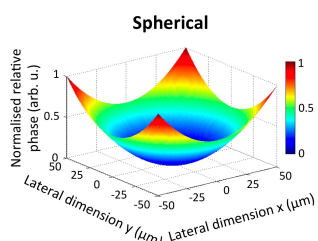
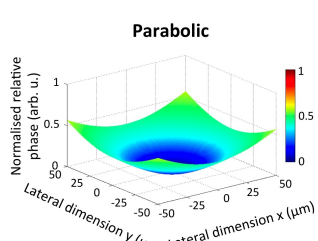
5.1.2 Sample system and methodology

The grating is based on a thin film of amorphous silicon (a-Si) as the high index material with a target thickness of 300 nm deposited on a conventional glass substrate (for a discussion of the target thickness, please see Section 5.1.3). The deposition was performed by collaborators at the Tyndall National Institute at Cork, Ireland, and was either done by electron-beam evaporation or by plasma-enhanced chemical vapour deposition (PECVD). For details of the deposition processes and a comparison, please refer back to Section 3.1 in Chapter 3. As there were fluctuations in the parameters in each deposition process, the thickness of the amorphous silicon in each batch varied between 260 to 360 nm.

The design is optimised for operation in reflection, normal incidence, and TM polarisation by including dispersion and absorption of the amorphous silicon (see Figure 4.1 of Chapter 4). As the target is to engineer a grating lens at near-infrared wavelengths, the design wavelength is either 980 nm or 1064 nm depending on the choice of light source. We designed several types of focussing lenses: cylindrical, spherical, and parabolic mirrors, all three of which were based on non-periodic patterning and different duty cycles. The focussing action of the diffractive lenses is based on the same effects as those of a curved mirror - comparable to the curvature of the mirror, which depends quadratically on the spatial dimension, the phase delay in reflection imposed by the grating on the incoming beam also depends on the square of the radius. For a cylindrical mirror, the phase profile is varied in one dimension only, while for a spherical and a parabolic mirror, it depends on both spatial dimensions. A particular attribute of a parabolic mirror is that no spherical aberrations occur; the entire wave front will be directed towards the focal spot irrespective of how far away from the optical axis the rays enter the mirror. In contrast, rays further away from the optical axis will not perfectly recombine at the focal spot in a spherical mirror and incur spherical aberrations. Similarly, we also do not have to account for spherical aberrations with the parabolic-type grating lens. The following Table 5.1 lists the respective formulae of the phase profile ϕ of these mirrors. For completeness, the linear phase profile of a mirror or prism is shown, which includes a constant factor c . The phase distribution of focussing reflectors basically depends on the operating free space wavelength λ_0 , the focal length f , and the spatial coordinates x and y with $r^2 = x^2 + y^2$.

As phase is a modulo 2π function, all phases exceeding the full phase range of 2π can be mapped to an equivalent value between 0 and 2π . I define a phase differential as the range of relative phase values in one radially symmetric zone of the lens that span values from 0 to 2π . A phase jump occurs at the interface between two successive zones when the maximum relative phase of a zone is followed by the minimum value of the next zone or vice versa. In other words, the phase jump is an abrupt change in the grating parameters that does not comply with adiabatic modifications [Johnson et al., 2002]. The implementation of a larger number of phase jumps and as such a larger lens diameter leads to a larger numerical aperture and hence higher focussing power. This is one aspect that we want to develop in this chapter. Another important fact we are testing is the broadband and angular behaviour of the grating lens at near-infrared wavelengths.

Table 5.1: Formulae and visualisations of the phase profile for typical flat and curved mirrors.

Mirror type	Equation	Phase profile
Conventional mirror / prism	$\phi(x) = cx$ (5.5)	<p style="text-align: center;">Linear</p> 
Cylindrical mirror	$\phi(x) = \frac{\pi}{\lambda_0 \cdot f} x^2$ (5.6)	<p style="text-align: center;">Cylindrical</p> 
Spherical mirror	$\phi(r) = \frac{\pi}{\lambda_0 \cdot f} r^2$ (5.7)	<p style="text-align: center;">Spherical</p> 
Parabolic mirror	$\phi(r) = \frac{2\pi}{\lambda_0} \left(\sqrt{r^2 + f^2} - f \right)$ (5.8)	<p style="text-align: center;">Parabolic</p> 

Using 1D rigorous coupled wave analysis (RCWA) [Moharam and Gaylord, 1981], the amplitude and phase of the grating reflectivity can be readily determined for a given grating thickness. Plotting these values as a function of the grating period and duty cycle yields a map that can be used as a look-up table for the target

phase profile [Fattal et al., 2010]. Having thus determined the reflection properties as a function of the period and duty cycle, we next determine a path through this phase map that connects successive grating parameters. The path is determined by the following considerations, in this order: a) Obtain a 2π phase change; b) create a continuous path to ensure that the grating parameters vary as little as possible, thereby observing adiabaticity as much as possible [Johnson et al., 2002]; c) maximise reflectivity. These considerations lead to a discrete phase profile and follow the path-finding algorithm after Dijkstra [1959].

My colleague and close collaborator Daan Stellinga programmed a design code in Matlab (MathWorks) that implements the RCWA data and the path-finding algorithm to generate a design of the grating lens, which varies in two dimensions, and which can be readily fed into the CAD software of the electron-beam lithography tool. The corresponding RCWA maps including a possible path are shown in Figure 5.1; these maps are based on the specific optical properties of amorphous silicon of thickness 300 nm.

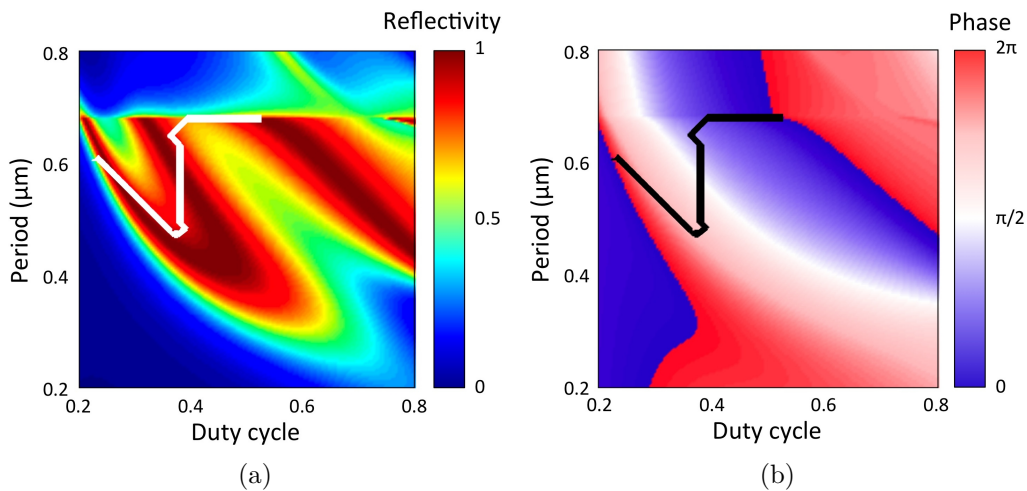


Figure 5.1: RCWA maps of (a) the magnitude and (b) the phase of the reflection coefficient as function of the period and duty cycle of an a-Si grating of thickness 300 nm operating at normally incident radiation in reflection, and for TM polarisation. The white and black lines show the path from 0 to 2π while the reflectivity is kept at a maximum. The graphs are calculated with the refractive index of PECVD amorphous silicon at a wavelength of 980 nm.

The corresponding phase profile as a function of radius, and the resulting grating, for a reflective grating with a parabolic phase profile, a focal length of $f = 100 \mu\text{m}$, and a diameter of $D = 80 \mu\text{m}$ are shown in Figure 5.2.

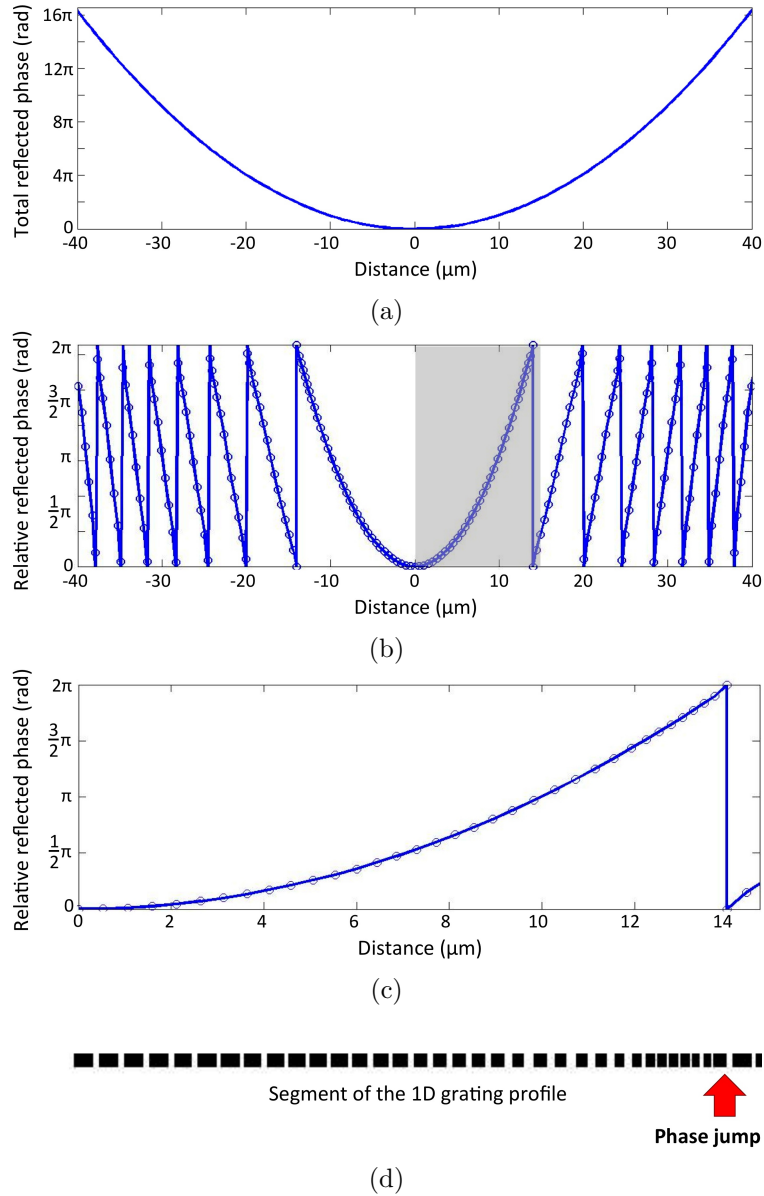


Figure 5.2: Parabolic phase profile along the central horizontal axis of an HCG lens with $f = 100 \mu\text{m}$ and $D = 80 \mu\text{m}$. (a) Full and ideal phase profile on the reflected side as function of the spatial extent of the lens. (b) Relative phase profile of the reflected light as a function of the spatial dimension of the lens; the solid line denotes the ideal phase profile and the circles denote the discrete phase values. Each circle is represented by a specific period, duty cycle, and reflectivity of the grating as taken for the fabrication. (c) Relative phase profile of the reflected light for a segment of the grating profile (grey shaded area in (b) shown) until the first phase jump occurs at around $14 \mu\text{m}$ away from the centre of the grating lens. (d) The corresponding grating ridges (black) and grooves (gaps) are shown below plot (c), with the arrow highlighting the first phase jump.

For the lens shown, we can see that eight phase jumps, i.e., eight radially symmetric zones defining each a parabolic phase profile from 0 to 2π , are necessary to obtain an NA of 0.37 . In order to obtain circular symmetry, the lens is constructed from gradually varying gratings along the horizontal and the vertical axis (x and y direction, respectively) from the centre to the edge. This construction results in the final design shown in Figure 5.3a together with the related phase distribution in Figure 5.3b.

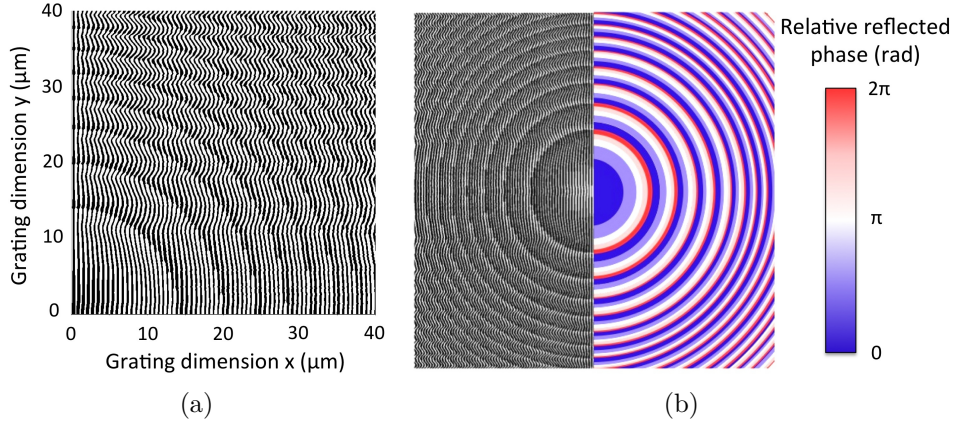


Figure 5.3: (a) Quarter view of a non-periodic HCG lens with $f = 100 \mu\text{m}$ and $D = 80 \mu\text{m}$. (b) Full design of the lens with the corresponding phase distribution shown in the right half. In both plots, the black lines represent the grating ridges and the white parts the grating grooves.

The spatial distance between two grating ridges and therefore the local period define the resolution required to make the grating lens; the HCG approach needs accuracies on a sub-micron level, which requires e-beam lithography, high performance deep UV lithography, or replication technologies such as nanoimprint lithography. On the other hand, the HCG approach allows us to define the phase accurately at any point in the plane; hence an overall diffraction efficiency of about 80% can be achieved. We observed such a high value in our FEM calculations (see Figure 5.4) and in the experimental results (Section 5.3.3). Similarly to Fresnel lenses and zone plates, the central zone is the largest one and with each new phase jump, the size of the zone decreases towards the outside of the lens. For example, in the central zone, the grating of Figure 5.2d has 34 different grating segments, each of which is composed of a different period and a duty cycle, and all of which contribute to the 2π phase profile. In the second zone, only 16 different grating segments determine the phase profile, and this number decreases the further we go.

We tested the focussing properties with the finite element COMSOL Multiphysics software. We used a computational cell consisting of a quarter grating lens with a parabolic phase profile and 330 nm amorphous silicon on glass (Figure 5.4). Due to computational limitations, it was only possible to implement a single phase jump. So the grating was designed with a radius of about $4 \mu\text{m}$ and a focal length of $5 \mu\text{m}$. Perfectly matched layers surrounded the cell to prevent unwanted reflections from the boundaries. A normally incident wave with wave vector \vec{k}_0 and a wavelength of 980 nm was modelled. Figure 5.4 shows the result of the wave reflecting from the grating.

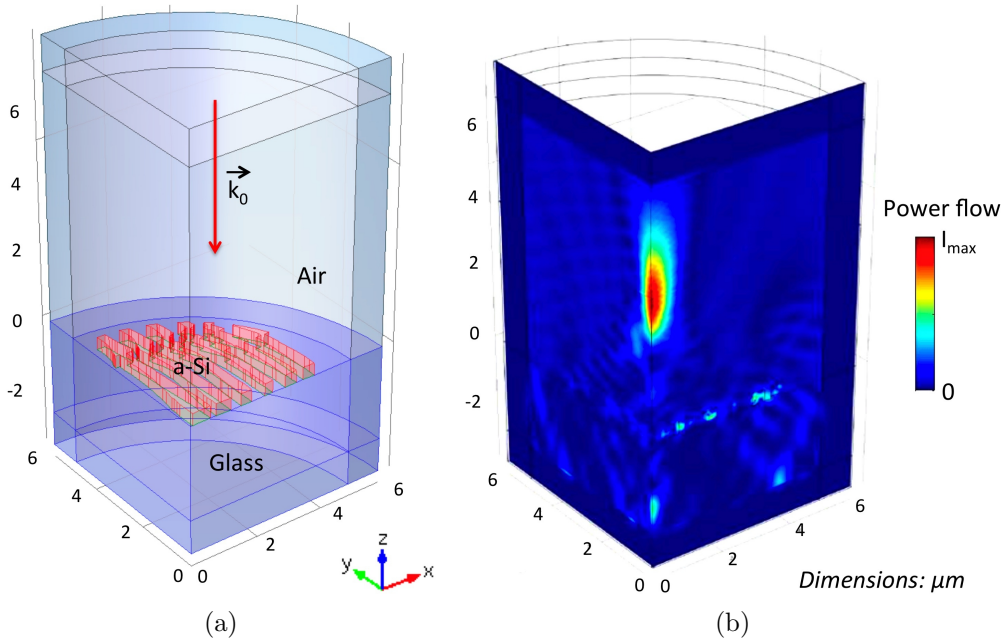


Figure 5.4: 3D FEM simulation of an HCG with a parabolic phase profile, a focal length of $f = 5 \mu\text{m}$, and diameter $D = 4 \mu\text{m}$ for an operating wavelength of 980 nm and TM polarisation. (a) Geometry of the design with the incident wave k_0 impinging normally to the structure. (b) Power flow highlighting the focal region around the desired focal length on the reflected side and a small contribution at the transmitted side (adapted from Daan Stellinga).

A focal spot at about $4 \mu\text{m}$ above the grating is apparent from this simulation and proves the design concept. Due to the limited lens size of only a few wavelengths, diffraction effects at the edges of the lens are significant and result in the spot location moving closer towards the lens (in our case: about $4 \mu\text{m}$ above the lens) compared to the target focal length (here: $5 \mu\text{m}$), which is in agreement with findings in the literature [Ruffieux et al., 2006]. According to this calculation, about 80% of the focussed radiation are concentrated in the bright spot compared to the incident

radiation, thereby referring to intensities above $1/e$. Due to the imperfect reflectivity apparent from the phase path (Figure 5.1), it is not possible to construct a path from 0 to 2π with $R = 1$ throughout, hence a fraction of the light will be focussed in transmission. The resulting spot in the back focal plane is located closer to the lens at $\sim 2 \mu\text{m}$ from the grating plane due to the higher refractive index in the glass medium. The simulation serves as a proof of principle and demonstrates the focussing capability of the approach.

5.1.3 Influence of grating thickness

The thickness of the grating is a critical parameter for achieving optimal reflectivity; it determines thin-film effects and therefore the overall interference between the vertical Fabry-Pérot modes and the lateral Bloch modes [Karagodsky and Chang-Hasnain, 2012]. The deviation from an optimum thickness will change the resonance behaviour and impact on the reflection and the spectral range over which high reflectivity is maintained, with the result that more light is transmitted. As the thickness of the amorphous silicon was slightly different for each run ($300 \text{ nm} \pm 20\%$), we investigated its influence on the grating performance numerically. The magnitude of the reflectivity is different along each phase path, which is why we introduced the average reflectivity over the entire path. In the design code, the number of investigated paths was set to 10, and then the path with the highest average reflectivity was chosen. The average reflectivity was defined as the mean value of the reflected intensities appearing across the path. In case of the lens considered in Figure 5.2 and Figure 5.3, the highest calculated average reflectivity over the full phase path is 80% and the distribution of reflectivity along the phase path is shown in Figure 5.5 together with the values of the period and the duty cycle.

Since we require full control over the wave front by incorporating several phase jumps into the lens design, there is a trade-off in the maximum reflectivity that can be achieved. This constraint is due to the fact that for certain grating parameters, i.e., a certain period and duty cycle, the grating is not exactly on resonance, which results in a lower reflectivity on a local scale [Verslegers et al., 2009]. Figure 5.6 shows the trace of the average reflectivity maintained over the calculated phase path for grating thicknesses between 140 nm and 1100 nm in steps of 10 nm combined with a comparison of the RCWA maps for the thickness of 300 nm used here and a larger thickness with similar average reflectivity.

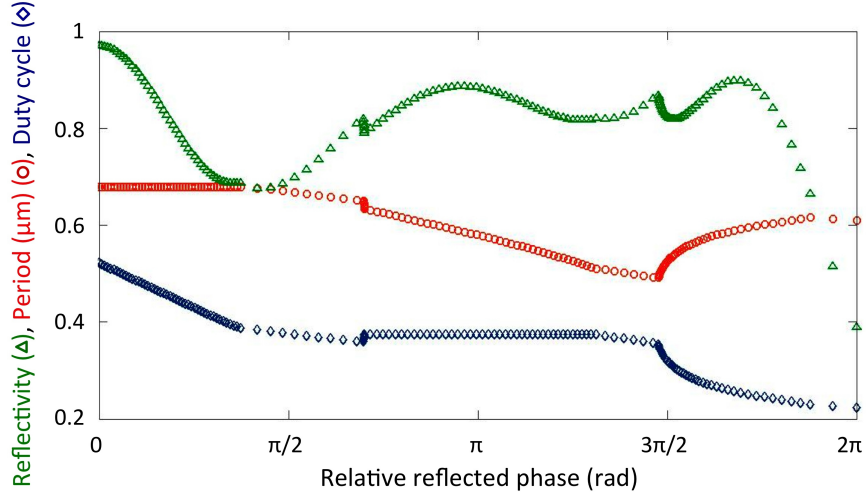


Figure 5.5: Distribution of reflectivity, period, and duty cycle over the parabolic phase path calculated for a grating thickness of 300 nm.

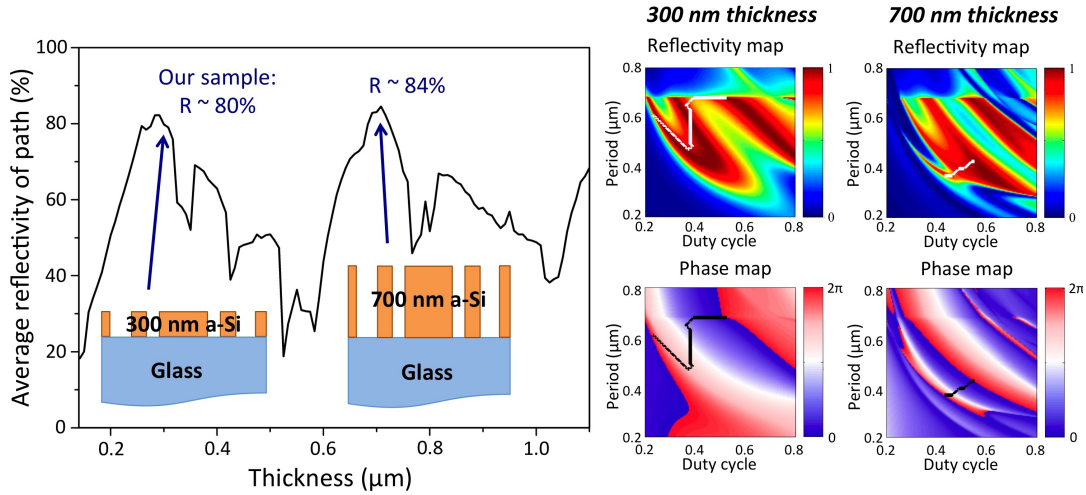


Figure 5.6: Influence of the grating thickness on the average reflectivity and the length of the calculated path. Left: Plotted average reflectivity of the calculated phase path as function of the silicon layer thickness. Arrows highlight two representative thickness values with maximum average reflectivity. Right: Region of the thickness (~ 300 nm) used in this work and region of high average reflectivity at a thickness of 700 nm with the corresponding RCWA maps and paths. Note that the non-zero absorption of amorphous silicon at a wavelength of 980 nm is included in the simulation.

Moreover, Figure 5.6 highlights several key points: First, at the lower end, e.g., for a silicon thickness of approximately 150 nm, the average reflectivity is below 20% and eventually decreases to 0 as the film thickness reduces further. For such a thin film, there is a lack of quasi-guided modes and the typical resonant behaviour of the

HCGs cannot be generated. Secondly, the graph features maxima and minima in reflectivity, which tend to occur in a periodic fashion, both in the thickness range from 300 to 700 nm and from 700 up to 1100 nm. We believe that these features are due to the FP modes of the slab, because the FP modes mainly depend on the grating thickness and less on the grating parameters. Including absorption into the model suggests that thicker layers perform worse; this is also observed as general trend even though there is a peak for 700 nm. We did not choose to operate at this point, however, due to fabrication complexity; a thicker film is more difficult to etch with high quality. Furthermore, the thicker film offers a shorter path; a shorter path means that the reflectivity changes significantly even for a small change in grating parameter. Given the tolerances of the fabrication technology, this sensitivity means that it will be difficult to follow a given path accurately. Why is the path shorter for a thicker film? Thin film interference theory tells us that a thicker slab can support more guided modes, which are more closely spaced the thicker the film gets. This phenomenon is apparent from Figure 5.6, where each arc in the phase diagram represents a quasi-guided mode. As a result, we chose to work with a 300 nm thick layer of amorphous silicon.

5.1.4 Investigation of numerical apertures and microlens arrays

The on-going trend of miniaturisation of bulky components and corresponding opportunity for large-scale integration of optical elements have a large impact on future developments in micro-optics. In particular, in imaging optics and spectroscopy applications, often involving liquid environments, arrays of optical elements are an important method for increasing image resolution and achieving higher sampling throughputs. Grating lenses may therefore find applications in lab-on-a-chip devices combined with microfluidic channels [Stone et al., 2004]. The field of optical tweezing/trapping [Ashkin et al., 1987] is another area of interest that could be advanced by using arrays of such devices, for example by generating large arrays of tweezing spots in parallel. Such arrays are typically generated by spatial light modulators [Cižmár et al., 2010], but these have the drawback that large arrays of traps are difficult to generate over a large area. Generating such arrays using micro-optics is therefore an interesting alternative. Merenda et al. [2007] have already taken this approach and have shown multiple single-beam optical traps with arrays of curved metal mirrors with a high NA of 0.96. Such curved geometries, however, impede microfluidic flow, which planar lenses do not. Accordingly, we investigated the range of numerical apertures obtainable with our approach. Lenses ranging from

5 μm to 100 μm diameter with focal lengths ranging from 5 μm up to 140 μm (NA ranging from 0.1 to 0.93) were designed and fabricated. A key concern for the optical trapping application is the numerical aperture of the lens, which needs to be a minimum of 0.7 [Merenda et al., 2007].

5.2 Fabrication of high contrast grating lenses

5.2.1 General aspects

As the RCWA code generates an ASCII file output, the design output can be directly transferred into the EBL software. Several mirrors and reflective-type lenses were fabricated: uniform periodic mirrors, cylindrical, spherical, and parabolic focussing reflectors. The typical e-beam exposure generates features that are wider than designed depending on the feature size, and therefore need to be corrected. The electron-beam resist ZEP 520A is positive, which means that exposed areas are washed away during development. Therefore, the grating grooves, i.e., the areas that will be etched away, are exposed. The problem is that for the chirped gratings used to create the lens effect, the grating period and duty cycle constantly change, so any correction was difficult to do. Initially, I performed the correction manually, by using SEM inspection and applying a correction factor depending on the duty cycle. Later, my colleague Daan Stellinga automated the process by embedding the path-algorithm in a convenient numerical code and transforming the data into an e-beam compatible file.

Another e-beam related issue is the proximity effect, which is caused by electron backscattering from the substrate into the resist. It leads to undesired exposure of the surrounding resist and thus a widening of the written area. As an example, Figure 5.7a shows a parabolic lens with $f = 140 \mu\text{m}$ and $D = 18 \mu\text{m}$ as designed. The black areas denote grating ridges (i.e., areas of semiconductor), while the white areas represent the gaps in between the ridges. The design code then inverts these areas, as groove areas have to be exposed in order to obtain correct etching. The inverted and proximity-corrected data file is shown in Figure 5.7b. The different colours represent the different doses used for the patterning procedure. As central areas receive more exposure from neighbouring features, they require a lower dose (blue colour) than those at the edge of the pattern (red). A scanning electron micrograph of the final etched and cleared sample is shown in Figure 5.7c.

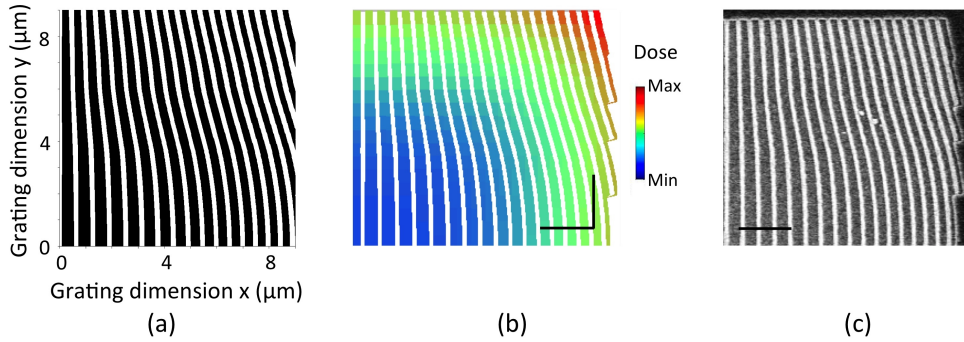
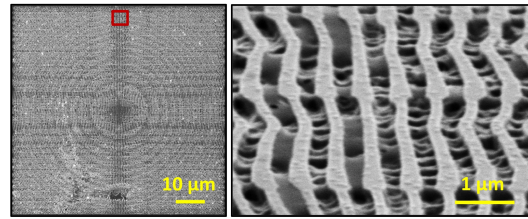


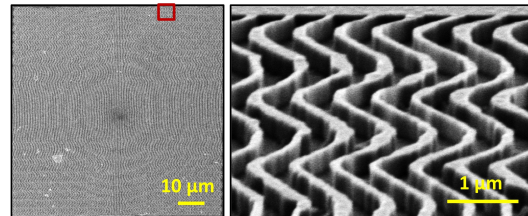
Figure 5.7: a) Quarter of a spherical lens design with $f = 140 \mu\text{m}$ and $D = 18 \mu\text{m}$. b) Proximity-corrected exposure pattern of a) with varying dose colours from the centre to the edges of the lens. c) SEM image of the fabricated lens in a). The black bar is $2 \mu\text{m}$.

The proximity error correction only provides relative dose factors, so the correct absolute exposure dose also needs to be determined. To exemplify, I show a sequence of lenses made with different exposure doses in Figure 5.8. The optimal exposure dose was $44.2 \mu\text{C}/\text{cm}^2$ with the 30 kV EBL system used at St Andrews. The structures are quite sensitive; a change of about 1% in the exposure dose already induced significant deviations from the desired structure. If the dose was lower than optimal, some grating ridges were still connected to each other after dry etching and resist removal (Figure 5.8a). For higher exposure doses, some lines started to break in areas in which the grating ridges had their sharpest bending radii and minimum ridge width (Figure 5.8c-e); these are the regions of the phase jumps. With increasing exposure dose, this damage extended further across the lens.

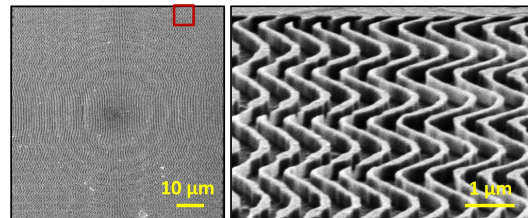
Figure 5.9 shows an overview of different reflective lens types that were fabricated successfully. The next step after a 45 s development in Xylene, followed by a dip-rinse in IPA, is dry etching using the same parameters as shown in Table 3.2 of Chapter 3. The high quality of fabrication I was able to achieve can be noted from the ultra-high resolution images (Figure 5.9), emphasising the sharp vertical side walls after etching and the smooth curvature of the grating ridges of the spherical and parabolic mirrors at the optimal exposure dose and etching time.



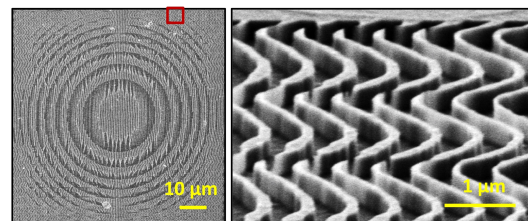
(a) Dose factor: $41.6 \mu\text{C}/\text{cm}^2$



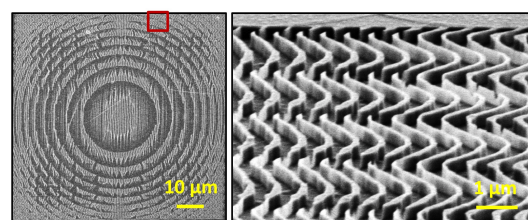
(b) Dose factor: $44.2 \mu\text{C}/\text{cm}^2$



(c) Dose factor: $46.8 \mu\text{C}/\text{cm}^2$



(d) Dose factor: $49.4 \mu\text{C}/\text{cm}^2$



(e) Dose factor: $52.0 \mu\text{C}/\text{cm}^2$

Figure 5.8: Fabricated reflective grating lens with parabolic phase profile, a focal length of $100 \mu\text{m}$, and $D = 80 \mu\text{m}$ using the following exposure doses: (a) $41.6 \mu\text{C}/\text{cm}^2$; (b) $44.2 \mu\text{C}/\text{cm}^2$; (c) $46.8 \mu\text{C}/\text{cm}^2$; (d) $49.4 \mu\text{C}/\text{cm}^2$; (e) $52.0 \mu\text{C}/\text{cm}^2$. The left image shows the entire lens, while the right figure shows a 30° (a) and a 45° (b-e) angled close-up view.

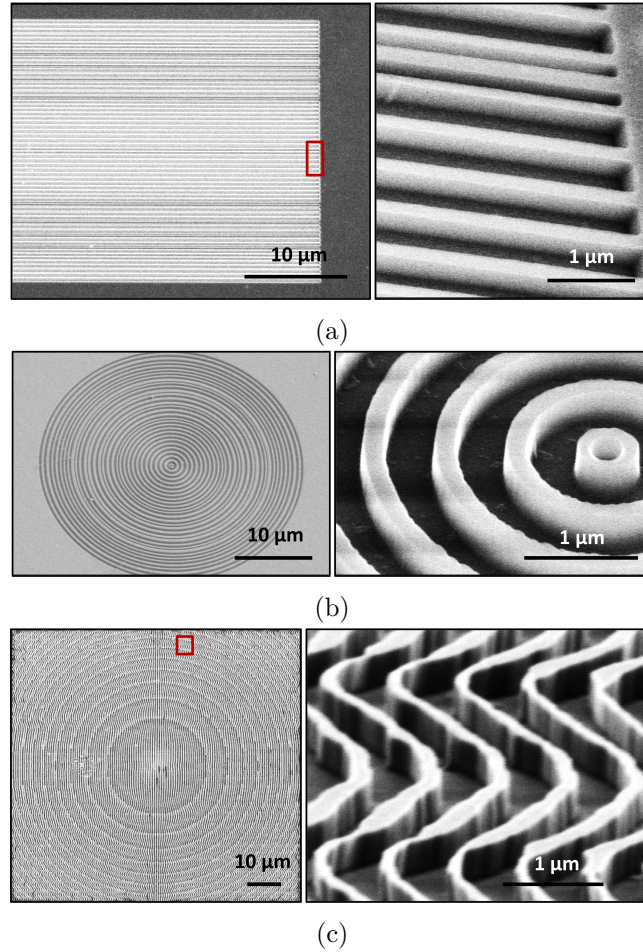


Figure 5.9: Scanning electron micrographs of fabricated focussing reflectors. (a) Cylindrical focussing mirror with $f = 100 \mu\text{m}$ and spatial extent of $36 \mu\text{m} \times 200 \mu\text{m}$; left: top view; right: close-up view at 45° . (b) Spherical focussing mirror with $f = 100 \mu\text{m}$ and $D = 36 \mu\text{m}$; left: viewed at 30° ; right: close-up view around the centre. (c) Parabolic focussing mirror with $f = 100 \mu\text{m}$ and $D = 80 \mu\text{m}$; left: top view; right: close-up view at 60° showing two phase jumps.

5.2.2 Grating lens arrays with high numerical aperture

Prior to fabricating grating lens arrays, I investigated the range of attainable numerical apertures considering that the medium above the lenses is water. Using the design approach presented in Section 5.1, I modelled parabolic focussing mirrors with diameters between 5 and $100 \mu\text{m}$ and focal lengths between 5 and $140 \mu\text{m}$, thereby covering a range of numerical apertures between 0.1 and 0.93 . These samples were written on the 50 kV system at York. Due to the higher acceleration voltage, the

proximity effect was much less noticeable and proximity correction was therefore not applied. The exposure dose was $130 \mu\text{C}/\text{cm}^2$, the development time 1 min at 23°C in Xylene and the etch time 2 min. The optical micrograph shown in Figure 5.10a illustrates the large range of lenses realised on a single chip. Moreover, an optical image of a grating lens array of size $1 \times 1 \text{ mm}^2$ depicts 65×65 lenslets each having an NA of 0.7 (Figure 5.10b).

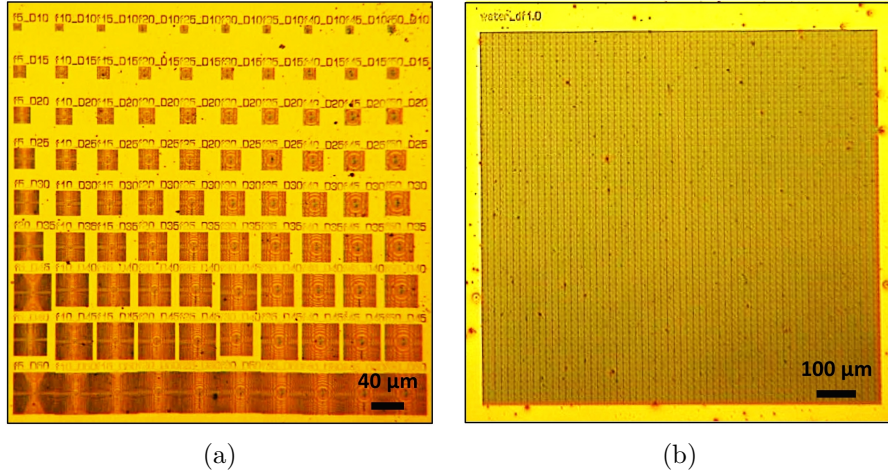


Figure 5.10: (a) Optical micrograph of fabricated HCG lenses with different numerical aperture values. (b) $1 \times 1 \text{ mm}^2$ grating lens array with 65×65 lenslets with $NA = 0.7$.

5.2.3 Integrated microfluidic

The organic polymer polydimethylsiloxane (PDMS) is widely used for the fabrication of microfluidic components. Over the years, our group has gained significant expertise in the integration of microfluidic channels made of PDMS with silicon-based devices, mainly driven by my colleague Dr Mark Scullion, who has taught me the relevant processing steps. For initial tests with water as the covering medium, I cut a thin PDMS layer ($<0.4 \text{ mm}$) into a rectangular frame, placed it around the structures on the silicon chip, filled it with a drop of de-ionised water and closed the reservoir with a glass cover slip (Figure 5.11a). In this form, I placed the sample into the optical characterisation setup and recorded the reflected focal lengths with water as the medium above the lenses. For optical trapping tests, which require a microfluidic flow of micron-sized particles such as glass or polymer beads, I built a PDMS device incorporating a microchannel above the grating lenslets onto the silicon chip. Following the fabrication recipe as described in Section 3.6 of Chapter 3, a PDMS layer with in- and outlets to the channel was bonded to the chip (Figure 5.11b) and

was ready to be measured in the optical trapping setup of our collaborators at St Andrews. The flow of liquid was controlled and the test solution was water, which contained polymer particles of sizes 1 and 3 μm .

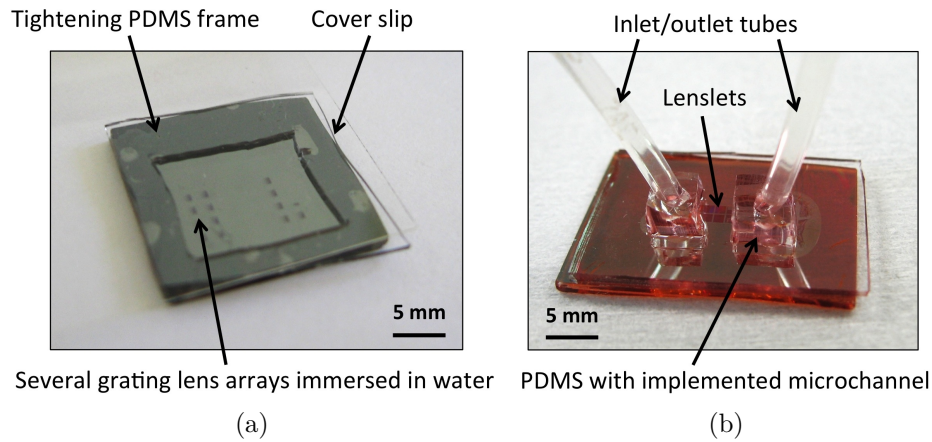


Figure 5.11: (a) Water-tight PDMS frame on a sample containing lens arrays covered by a cover slip. (b) Sample with HCG lens arrays bonded to a microfluidic channel made of PDMS with inlet and outlet tubes.

5.3 Characterisation of high contrast grating lenses

5.3.1 Wavelength dependence

A study of the influence of the incident wavelength serves as another parameter of the performance of the high contrast grating lens. As described above, the lens is optimised for an operating wavelength around 1 μm ; however, due to the broadband character of HCGs, we expect the lens to work over a wide spectral range. We used a 1D non-periodic reflective grating structure designed for a normally incident, TM-polarised wave at 980 nm to simulate the response of various incident wavelengths between 830 and 1130 nm, using the RF module of COMSOL Multiphysics. The grating had a thickness of 330 nm, assuming amorphous silicon as the high index layer with glass as the substrate. The grating was designed for a focal length of 60 μm and an NA of 0.64. The resulting optical response is the time-averaged power flow normalised to an incident power on the grating of 1 W and is shown in Figure 5.12 as a function of the distance from the grating along the optical axis. We estimate that about 80% of the total power is focussed.

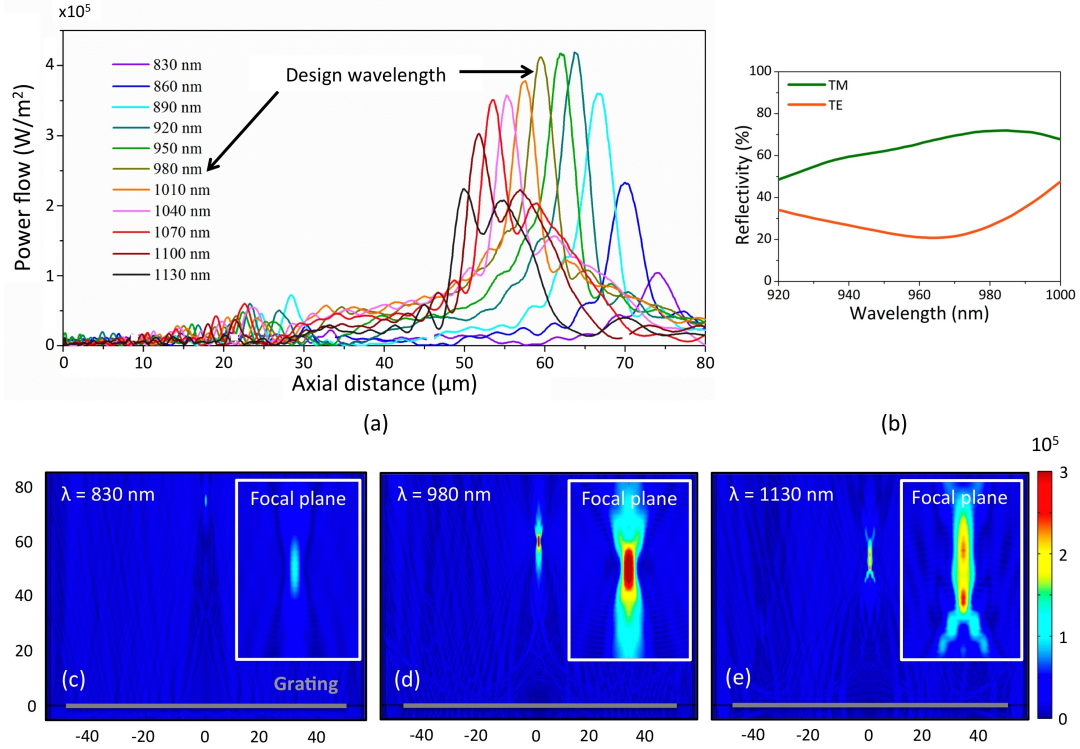


Figure 5.12: (a) Influence of operating wavelength (here at 980 nm) on a grating lens with focal length of 60 μm and NA of 0.64. (b) Reflection measurements of an HCG lens with $f = 100 \mu\text{m}$ and $D = 80 \mu\text{m}$ at both orthogonal polarisations. The three plots (c)-(e) show the power flow at the reflected side for three different incident wavelengths; the colour bar denotes the power flow in W/m^2 and the x and y axes are the lateral and axial coordinates, respectively (Figures (a),(c)-(e) adapted from simulations by Daan Stellingma).

Illumination at the design wavelength of 980 nm establishes the target axial location of the focal spot at 60 μm ; however, smaller wavelengths down to 920 nm reach slightly higher maximum intensities in the focal region despite their deviation from 60 μm . We believe that this difference is caused by uncertainties in the optical constants of amorphous silicon. We note that while testing for different incident wavelengths, the intensity in the focal spot remains quite high, and even 120 nm away from the design wavelength, only a 3 dB drop-off occurs on either side. This large spectral tolerance corresponds directly to the wideband response of the HCG as described in Chapter 4. Furthermore, if we look at the actual paths in the reflectivity and phase map, we see that the path is very long, which indicates a large fabrication tolerance. For shorter incident wavelengths, the focal spot is situated further away from the lens, while longer wavelengths shift it closer. The variation in focal length with wavelength is due to the change in optical path lengths in the medium above the

lens (air). Focussing occurs at the point where all the rays from the grating arrive with the same phase, and since the physical distance over which the phase changes depends on the wavelength, the focal distance does as well. Regarding the shape of the focus, we observe an axial shift in the focal spot (Figures 5.12b,c,d), whereby the lateral extent of the spot is generally maintained. In general, an elongated focal spot is observed in the axial direction, which occurs for Fresnel numbers near unity or smaller and is also called “focal shift“ in the literature [Li and Platzter, 1983, Vokinger et al., 1998]. The shape arises from the difference between the geometrically defined location of the focal spot and the position of the spot with the highest intensity [Vokinger et al., 1998]. At the design wavelength, the focal spot has an axial dimension of approximately $5\ \mu\text{m}$. For longer incident wavelength, e.g., 1130 nm (Figure 5.12d), the elongation increases such that the focal spot becomes separated into two spots. At smaller incident wavelengths, the axial extent of the spot decreases.

Furthermore, Figure 5.12b shows an experiment carried out with a grating lens with the reflectivity setup at our collaborators’ in Cork (see Figure 4.5 in Chapter 4) to investigate its broadband behaviour. The spectral properties of a fabricated focussing lens with a grating thickness of 320 nm, a focal length of $100\ \mu\text{m}$, and a diameter of $80\ \mu\text{m}$ were studied for both orthogonal polarisations. The lens was designed for operation in reflection at a wavelength of 980 nm, normal incidence, and TM polarisation. Apart from the rather low reflectivity of about 72% achieved around 980 nm for this sample, we can clearly see the broadband effect of the grating lens with only 10% intensity drop-off 20 nm away on either side.

5.3.2 Angle dependence

Another important performance parameter for a lens is the dependence on the incident angle. We used a grating lens with a focal length of $60\ \mu\text{m}$, NA of 0.32, thickness of 330 nm, and tested the spectral response in reflection along the axial direction for incidence angles θ from 0° up to 12° and for TM polarisation (Figure 5.13). For normal incidence, the power flow into the focal spot is maximal and the axial spot elongation is about $15\ \mu\text{m}$. For small angles up to 6° or 8° , the intensity in the focal spot drops but still remains significant. But beyond 8° , the intensity vanishes quickly. The location of the focal spot follows the input axis, as expected. This angular behaviour is very different compared to refractive lenses, which usually exhibit a large angular tolerance. For a grating lens, however, the angular dependence is governed by the Bragg effect of the individual gratings contained in the lens, which

is k-vector dependent, i.e., it depends on a specific angle. Hence, the grating lens is very angle-selective.

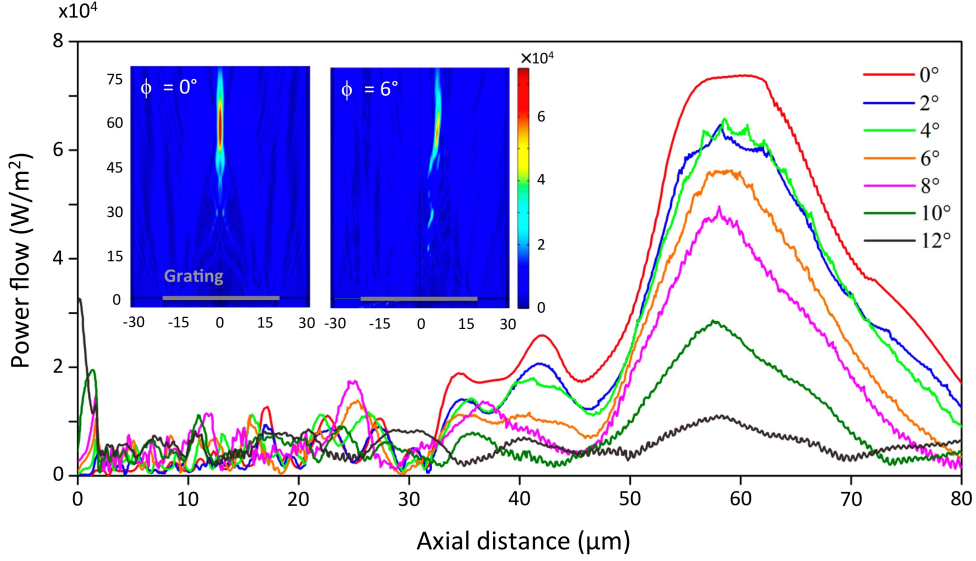


Figure 5.13: Influence of angle of incidence on the focussing performance. The HCG lens exhibits a small tolerance against varying angles. The two inset plots show the power flow at the reflected side for normal incidence and for an angle of 6° (picture modified after simulation by Daan Stellingma).

Looking at the wave vector dependence in more detail proves to be instructive: For periodic resonant structures with periodicity a , a change of incidence angle usually corresponds to a change in wavelength because of the relation:

$$|\vec{k}| = |\vec{k}_{\parallel} + p \cdot \vec{G}|, \quad (5.9)$$

in which \vec{k} is the wave vector of the incident light, \vec{k}_{\parallel} the component of the incident wave vector in the plane of the grating, p an integer and \vec{G} the grating vector, whose magnitude corresponds to $2\pi/a$. Substituting the wavelength and angular dependence into Equation 5.9, it becomes:

$$\frac{2\pi}{\lambda} = \sin(\theta) \cdot \frac{2\pi}{\lambda} + p \frac{2\pi}{a} \quad (5.10)$$

or

$$\frac{2\pi}{\lambda_{eff}} = |p \cdot \vec{G}|, \quad (5.11)$$

where

$$\lambda_{eff} = \frac{\lambda}{1 - \sin(\theta)} \quad (5.12)$$

We would therefore expect a change of angle to affect our grating lenses in much the same way as an increase in wavelength. Comparing Figure 5.12 and Figure 5.13, and using Equation 5.12, we find that this line of reasoning holds fairly well in terms of the intensity of the focal spot. For example, an incidence angle of 6° corresponds to a wavelength of 1094 nm, at which point we would expect the intensity to have decreased by about 25% in the wavelength plot (Figure 5.12), as it does in the angular plot (Figure 5.13). As the shift of the focal spots in Figure 5.12 originates from optical path length differences after the grating, we would not expect a similar shift of the focal spot position with angle, which is indeed what we observe.

We need to stress that the simulated structures are only example grating structures. For different design wavelengths, thicknesses, polarizations, or materials, different wavelength and angle dependencies will apply. An indication of the spectral bandwidth can be obtained from the RCWA map and the phase path for a grating (see Figure 5.1), since a change in wavelength, and therefore angle, roughly corresponds to a change in period, and therefore a shift of the path up or down along that axis on the RCWA maps. The further the path can be shifted without significantly changing the phase and reflectivity response, the more broadband and angle independent the resulting lens will be. Due to the similarity of the grating-based lens and a blazed diffractive system [Lalanne, 1999] achromatic effects such as the intensity drop in the focal spot for incident wavelengths or angles different from the design could be partially explained by the physics of blazed gratings; however, an in-depth comparison of the two systems is beyond the scope of this work and might be subject of a future investigation.

5.3.3 Beam profile of the diffractive lens

To characterise the focussing properties of the reflective grating lenses, I built the optical setup as shown in Figure 5.14. I used a vertical cavity surface emitting (VCSEL) laser operating at a wavelength of 980 nm. For an injection current of 4 mA the laser generates an optical power of about 1.85 mW. A lens (L3) was used to collect the highly diverging laser radiation. A polariser ensured that the emitted radiation was linearly polarised. Following a beam splitter (BS) cube, I used an

objective (L2) with a magnification of 20x to collimate the light to a beam waist of approximately 1 mm. The sample itself was mounted on a translation stage with the silicon side facing the source and illuminated from the back with a collimated (using lens L1) white light LED. In order to operate in TM polarisation, the sample was mounted such that the grating ridges were aligned perpendicular to the polarisation direction. The imaging arm consisted of a telescope to collect the reflected light and focus it onto a CMOS camera (Thorlabs). By translating the sample along the optical axis, the imaging plane of the camera could be adjusted, which allowed me to take slices of the intensity evolution along the optical axis. I define the front focal plane as the imaging plane of the camera at which the reflected focal spot is detected with the highest intensity; the back focal plane is the plane with a focal spot eventually appearing in transmission.

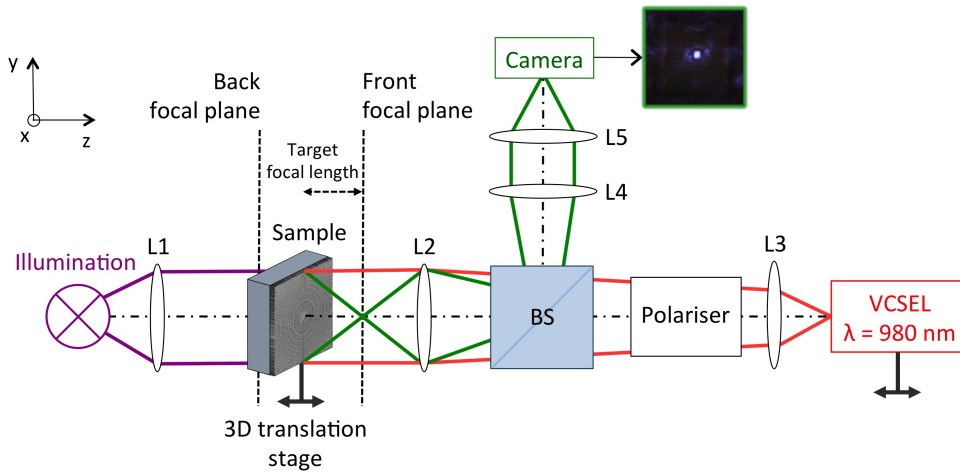


Figure 5.14: Experimental setup for the characterisation of the HCG lenses. BS = beam splitter, L = lens, ray traces in red denote incoming radiation, rays in green mark reflected radiation as detected by the camera, purple rays show ray traces of the illumination light. The dashed black line through the optical components indicates the optical axis.

Figure 5.15 shows the initial measurements of the evolution of the foci of a cylindrical focussing mirror (Figure 5.15a) and a spherical focussing mirror (Figure 5.15b) with a focal length of $100 \mu\text{m}$ each. We note that the focussing properties were relatively poor; the cylindrical lens produced a line focus clearly visible along the lateral dimension in the inset of Figure 5.15a, but there was a lot of noise associated with it. Its spot width was just below $2 \mu\text{m}$, measured as full width at half maximum (*FWHM*). For the circular lens, a spot with a size of approximately $3 \mu\text{m}$ was recorded (Figure 5.15b), although the focal spot is also relatively weak compared to the background noise. The asymmetry in the intensity profiles was mainly attributed

to fabrication imperfections as visible from the inset SEM images. The measured focal length for both samples was close to the expected value of $100\ \mu\text{m}$. In these initial measurements, I noticed by SEM investigation that the actual thickness of amorphous silicon was significantly thinner than expected ($270\ \text{nm}$ instead of $300\ \text{nm}$). as apparent from the change in average reflectivity down to 60% for this thickness instead of 80% for $300\ \text{nm}$, as shown in Figure 5.6.

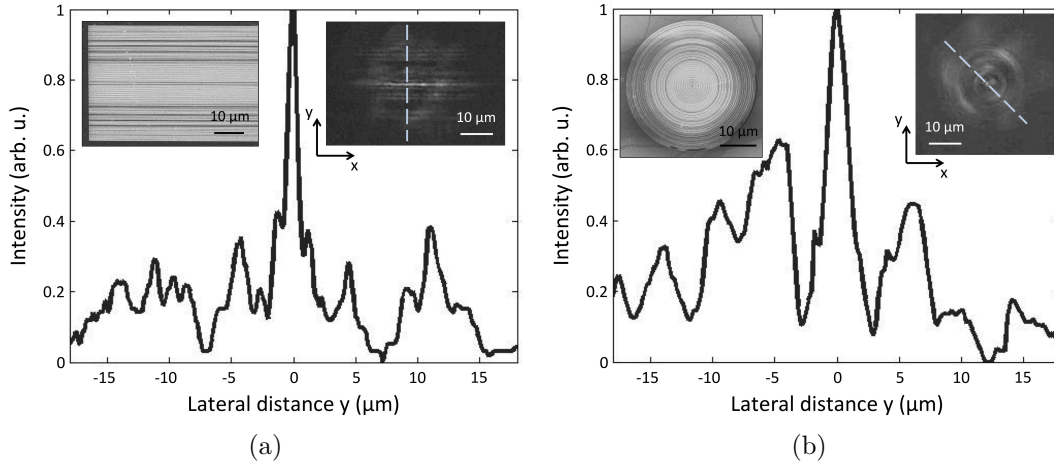


Figure 5.15: (a) Lateral intensity profile of a reflective grating lens with a cylindrical phase profile and a focal length of $100\ \mu\text{m}$. (b) Lateral intensity profile of a fabricated grating lens with a spherical phase profile and a focal length of $100\ \mu\text{m}$. In both graphs, the insets depict scanning electron micrographs and the cross-sectional image taken during the measurement of either lens. The blue dashed line represents the corresponding lateral profile.

To address this issue, prior to the production of new focussing lenses, the structures were redesigned for the actual thickness of about $360\text{-}370\ \text{nm}$. The result of a parabolic focussing lens (Figure 5.16) shows a very clear and pronounced beam profile for a designed high numerical aperture of 0.37 , a target focal length of $100\ \mu\text{m}$ and a diameter of $80\ \mu\text{m}$, optimised for a wavelength of $980\ \text{nm}$. The lower part of the figure shows a montage of slices of normalised intensity at the front and the rear of the lens. The upper part of the figure shows a scanning electron micrograph of the sample itself as well as lateral profiles of the reflected and transmitted spots. The measurement of the beam profiles of the lens reveals two focal spots appearing on either side of the sample, which is in agreement with the property of “double-focussing“ of these gratings caused by the corresponding phase profiles in reflection and in transmission [Lu et al., 2010]. A very bright reflected spot appeared at about $130\ \mu\text{m}$ and a less intense transmitted spot at less than $90\ \mu\text{m}$ away from the lens.

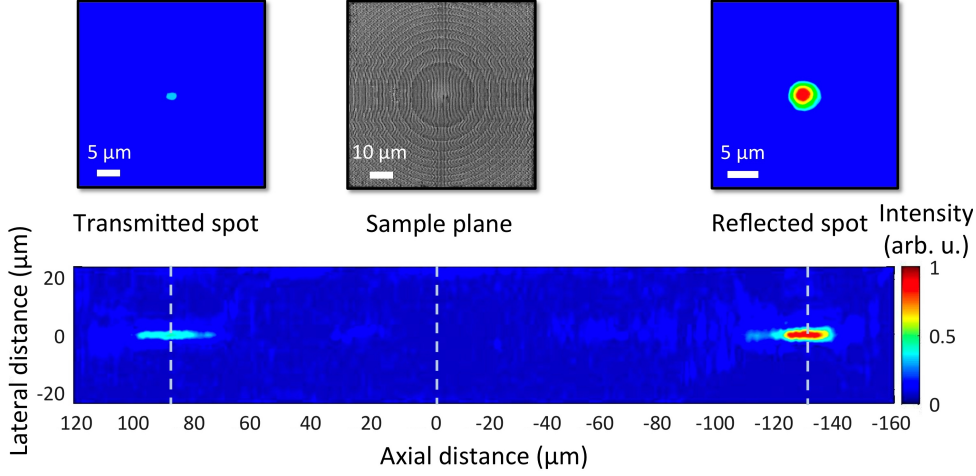


Figure 5.16: Experimental result of an HCG lens with a parabolic phase profile, $f=100 \mu\text{m}$, and $D=80 \mu\text{m}$, measured at a wavelength of 980 nm, normal incidence, and TM polarisation. The top three graphs show the colour-coded cross-sections of the reflected (left) and transmitted spot (right), and the SEM (centre) of the lens. The lower graph shows the intensity evolution at the rear and front of the lens.

Both measured distances deviate from the target focal distance of $100 \mu\text{m}$; however, as the transmitted spot is formed in the substrate, the theoretical focal length should be approximately $70 \mu\text{m}$ while accounting for the refractive index of glass of about 1.44 at 980 nm. Hence, both measured distances are slightly larger than the designed ones, which was the case for the majority of lens samples I measured. Most probably the main reasons for this deviation are fabrication imperfections; as it would be too difficult to measure every grating parameter across the 2D structure, spot checks of some ridge and groove widths as well as periods were performed at the central region and at the phase jumps of the lens by scanning electron microscopy. After checks in the SEM, it turned out that the duty cycle is the most difficult parameter to control during fabrication, which we believe is responsible for the observed performance tolerances. The background noise notable in the montage of intensity slices stems from back reflections from optical components such as imaging lenses and the beam splitter that were lacking dedicated anti-reflection coatings at the particular wavelength used. The beam profile also shows a larger axial extent of both spots than in the lateral directions. In theory, for a lens with $NA = 0.37$ operating at a wavelength of 980 nm, the axial resolution z_{ax} is about $7 \mu\text{m}$ according to Equation 5.2. Measuring the axial distance at the point where the intensity of the reflected spot dropped by $1/e$ results in $15 \mu\text{m}$, which is double the expected value. One reason for this discrepancy might be caused by fabrication imperfections as well as by our definition of the end points of the axial region. For instance, Givens [1982]

defines the depth of focus at the points, where the intensity has dropped to 80% of the maximum value, in which case we arrive at approximately $10 \mu\text{m}$ axial distance.

The lateral cross-sectional plots of Figure 5.16 and Figure 5.17a allow further investigations of the measured spot sizes. From the two figures, an Airy spot diameter d of about $5 \mu\text{m}$ for the main reflected focal spot and about $2\text{-}3 \mu\text{m}$ for the transmitted one can be extracted. For our lens, the Airy disk diameter d_{lim} is $3.2 \mu\text{m}$ in theory (Equation 5.3). This shows that the measured value of approximately $5 \mu\text{m}$ is very close to the diffraction limit and underlines the high quality of the fabricated grating lens. Additionally, Figure 5.17b points out the effect of the polarisation as the reflected spot was measured for both TM- and TE-polarised input light, which resulted in two different intensities. I recorded approximately half of the intensity in the focal spot for a TE-polarised input compared to the TM polarisation that the lens was designed for. As the grating elements are no longer linear in the 2D design, some polarisation mixing does take place, which explains this result.

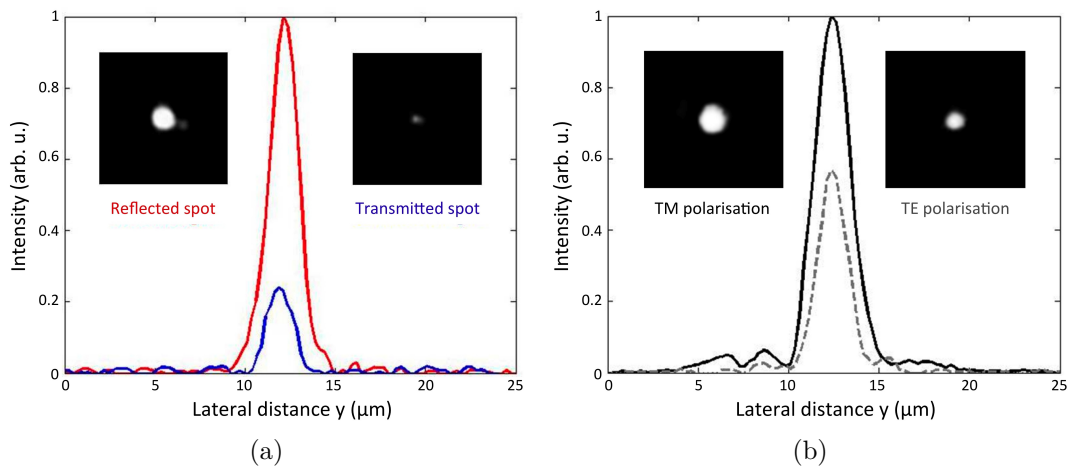


Figure 5.17: (a) Measured intensity profiles of the reflected and transmitted spots for the lens in Figure 5.16, recorded at a wavelength of 980 nm and for TM polarisation. (b) Intensity profiles of the reflected spots for both orthogonal polarisations.

5.3.4 Scan of different numerical apertures

In order to determine the corresponding numerical apertures, the focal lengths were measured for each lens with the setup shown in Figure 5.14. A comparison between the design-value and the measured value is shown in Figure 5.18 for differently sized grating lenses.

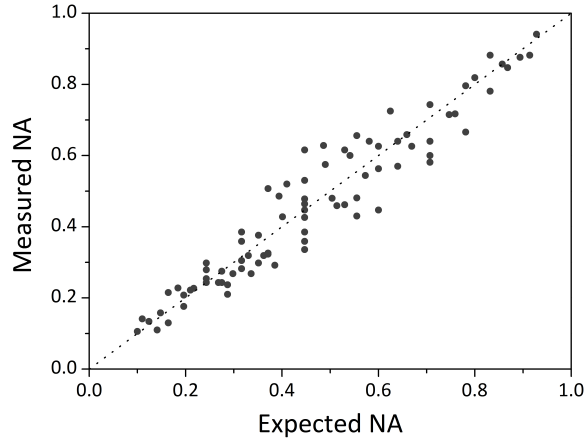


Figure 5.18: Comparison between measured and calculated numerical apertures for different fabricated grating lenses. The linear dashed line shows the ideal trend.

The overall agreement between calculated and measured NAs is very good, which emphasises the high quality of our fabrication processing and focussing performance of the grating lenses. In most cases, I recorded an error of about 10% between designed and measured focal lengths. At central NA values between approximately 0.3 and 0.7, however, the measured focal distances deviated more with about 15% for many samples compared to the design, mainly caused by fabrication imperfections as described before with the most significant tolerance existing in the actual duty cycles. Overall, I was able to achieve a range of numerical apertures between 0.1 and 0.93 with the grating lenses.

5.3.5 Grating lens arrays with high numerical aperture for optical trapping

Compared to microlenses based on polymers [Chen et al., 2004] and microlens arrays written in photosensitive glass by femtosecond laser micromachining [Lin et al., 2009], the silicon-based lenses achieve much higher NA values while being thermally and mechanically more robust. As stated in the beginning of this chapter, the high- NA grating lenses are designed to have a parabolic phase profile - in this way they are not suffering from spherical aberrations, which are an issue with refractive microlenses and hence reduce their NA and lens quality. The investigation of attainable NAs lead to the investigation of large-scale optical trapping performed on arrays of 1×1 mm² in size. I chose grating lenses with a parabolic phase profile and a numerical aperture of 0.7, an empirical value established by the community as being sufficient

to achieve optical trapping [Merenda et al., 2007]. To enable flow of microparticles, I integrated a microfluidic PDMS channel onto the top of the sample as specified in the fabrication chapter (Chapter 3) and illustrated in Figure 5.11b. Our collaborators Dr Mingzhou Chen and Dr Tom Vettenburg from the University of St Andrews have tested the array with their own imaging and trapping setup (Figure 5.19).

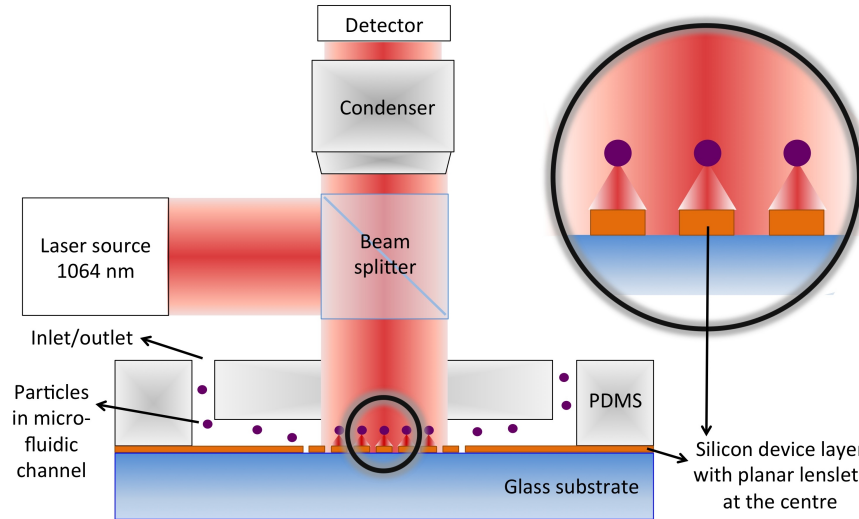


Figure 5.19: Schematic sketch of the optical trapping setup at St Andrews to test the performance of flat reflective HCG lens arrays. Small polymer particles (1 and $3 \mu\text{m}$ in diameter) are introduced by the channel inlet and flow through the microfluidic channel to the outlet. Note that the drawing is not to scale.

Prior to trapping tests, they captured an image of the multiple foci. For the imaging of the multiple foci, a collimated and TM-polarised beam of a fibre laser operating at a wavelength of 1064 nm and an optical power of about 5 W was launched through a beam splitter and illuminated the lens array through the transparent PDMS layer. We used an infrared-sensitive camera to capture the resulting image (Figure 5.20a). Due to imperfect collimation of the incoming laser beam, not all reflected focal spots are illuminated equally in intensity and therefore are not visible throughout the entire image. In addition, spurious reflections in the acquired image originated from collapsing grating ridges (Figures 5.20b,c) as well as residual spaces between adjacent grating lenses in one lateral dimension (vertically in Figure 5.20d). Therefore, we were not able to demonstrate convincingly that optical trapping actually happened; however, we observed that the trajectories of passing microparticles changed while moving through the focus of the lenses. We believe that the structural damage described above has decreased the numerical aperture considerably.

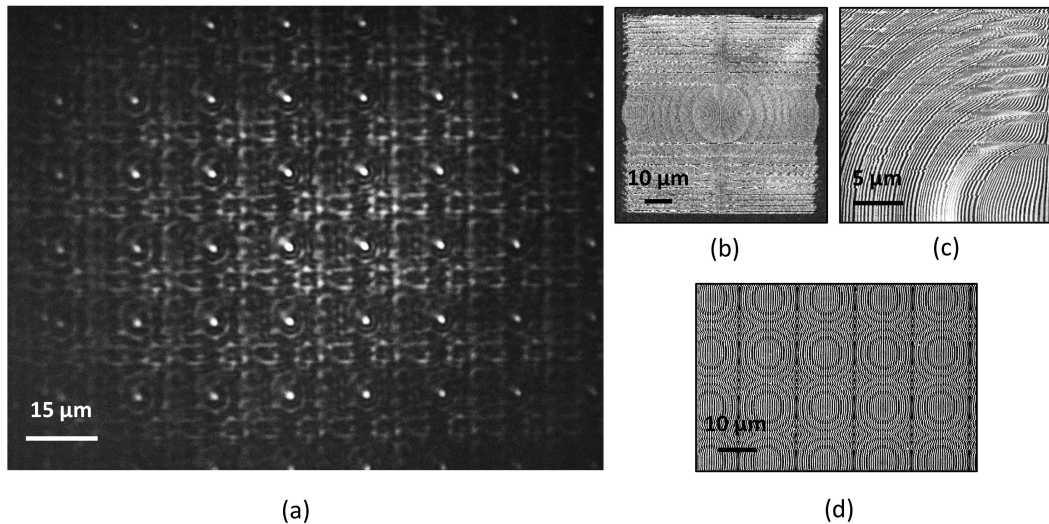


Figure 5.20: (a) Focussing image of the lens array measured with a fibre laser at 1064 nm, TM polarisation and normal incidence. The field of view is reduced due to imperfect collimation of the beam input. (b) SEM image of an individual grating lens. (c) Close-up view of the lens in (b). (d) Section of a $1 \times 1 \text{ mm}^2$ lens array with a designed NA of 0.7.

To rectify the issue of the collapsing grating ridges, we decided to change only one grating parameter (duty cycle). My colleague Daan Stellinga modified the design code accordingly to keep the periodicity constant for the desired structure, while changing the duty cycle only. The modified lens is shown in Figure 5.21.

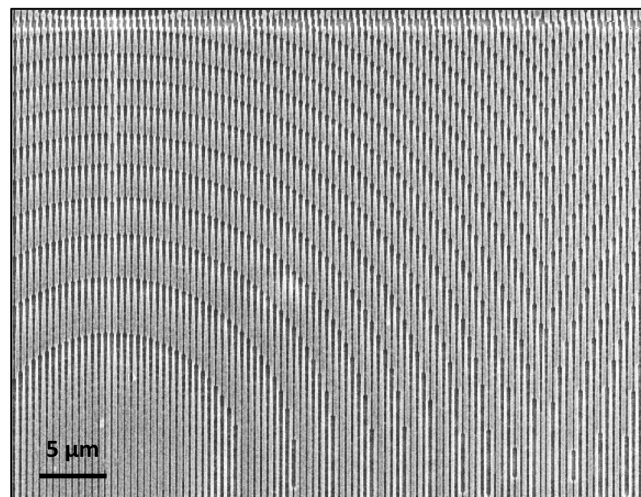


Figure 5.21: Close-up view of a lens with designed NA of 0.7, but keeping the design period equal throughout the structure. No collapsing grating ridges and spaces to the adjacent lenses are visible compared to Figure 5.20b and 5.20c.

As a result, the fabrication issue of ridge damage has improved significantly for the modified reflective lenses, which makes it much easier to create larger gratings with high numerical aperture that necessarily incorporate multiple phase jumps. We now achieve a high uniformity and positioning accuracy of each lens. Additionally, we have made the array from square-shaped rather than round lenses, thereby utilising the array space more effectively. In a further trapping experiment with the improved grating lens, a significant fraction of microparticles adhered randomly to the silicon surface, thereby impeding efficient trapping. Potentially, a functionalisation of the surface is indicated. Considering the time and cost involved in making such an array electron-beam lithography is not an ideal tool for mass production; instead such arrays could be made much more cost-effectively and faster by using parallel exposure techniques such as deep-ultraviolet lithography [Bogaerts et al., 2002]. Alternatively, by producing a “master“ stamp, through EBL, the structures could be replicated with nanoimprint techniques [Chou and Krauss, 1997], which can produce multiple copies of the master at much lower cost.

5.4 Summary

In this chapter, I described the design process, the fabrication, and the characterisation of reflective diffractive lenses based on wavelength-scale high contrast gratings in amorphous silicon. The success of the non-periodic 2D diffractive lens design with parabolic phase profile was that we could experimentally show high numerical apertures ($NA = 0.37$) for the first time by implementing multiple phase jumps [Klemm et al., 2013]. There were also some surprising effects in the experiment. First, the structured lens, even though it should be polarisation-selective, exhibited some polarisation sensitivity (Figure 5.17b) due to the curvature of the grating lines. Secondly, despite the incorporation of many phase jumps, the diffraction efficiency and spot quality remained very high as evident from the near-diffraction-limited spot size and recorded beam profile (Figure 5.16). The near-diffraction limited performance makes these lenses a good candidate for imaging applications. One of the main key criteria for an efficient microlens is the planarity of the device, which is maintained by the binary surface topography. As a consequence, the technological feasibility is rather straightforward with standard silicon processing. The investigation of the numerical apertures attainable with the grating lens revealed a large range from 0.1 up to 0.93 (Figure 5.18), which opens the door to versatile applications within micro-optics making this lens a very practical and highly compact

tool. New applications exploiting the unique properties of our silicon grating lenses have also been identified, one of them being to use an array of high- NA grating lenses for large-scale optical trapping of microparticles in collaboration with colleagues at the University of St Andrews. When considering the fabrication of large arrays of grating lenses, replication techniques like nanoimprint lithography are more appropriate and could pave the way to low-cost manufacturing. Due to limitations of the grating lens to on-axis beams, we have not considered a characterisation of the modulation transfer function, which would be a crucial performance parameter for imaging applications. In future experiments, the relative differences in intensity in the focal spot for lenses with a different NA value could be specified further to obtain an idea about the varying power distributions. The large design flexibility is also attributed to the scalability of the grating lenses to other wavelengths of interest such as the mid-infrared spectral range, in the same way as photonic crystals are. Another prospective project is to use the grating's ability of producing an arbitrary phase response to improve the output beam of a semiconductor optical amplifier, together with the collaborating company Superlum in Cork.

6 Static Fabry-Pérot filter based on high contrast gratings

Following the successful demonstration of broadband reflectors (Chapter 4) and flat silicon focussing mirrors (Chapter 5), this chapter presents the challenges in incorporating the high contrast grating mirrors into Fabry-Pérot cavities as a prerequisite for the tuneable filters that will be described in Chapter 7. Initially, metal mirrors were connected to each other. After successful fabrication of metal-based FP resonators, two grating-based reflectors were bonded to create a static Fabry-Pérot device. This chapter is organised as follows: Section 6.1 states the concept and design of both metal- and grating-based Fabry-Pérot interferometers. The devices were fabricated using conventional surface micromachining processes (Section 6.2) and their optical performance is discussed in Section 6.3 and all results are summarised in Section 6.4.

6.1 Design of static FP filters

In the quest for miniaturised and high performance optical filters in the near-infrared wavelength range, I studied the feasibility of using amorphous high contrast gratings mirrors in a static Fabry-Pérot resonator as an intermediate step towards tuneable cavities following in Chapter 7. We used transparent glass substrates to enable operation in transmission, which is experimentally more convenient than the alternative reflective approach [Kuznetsov et al., 2010]. I started with metal-metal mirrors. Regarding the reflectivity of the most commonly deposited metals such as silver, gold, and aluminium, gold has a high reflectance in the near-infrared range without exhibiting any degradation processes. I chose gold because it can be easily deposited and is chemically very stable. In order to determine the best layer thickness, I used a quick RCWA analysis shown in Figure 6.1 (optical constants taken from Filmetrics [2014]).

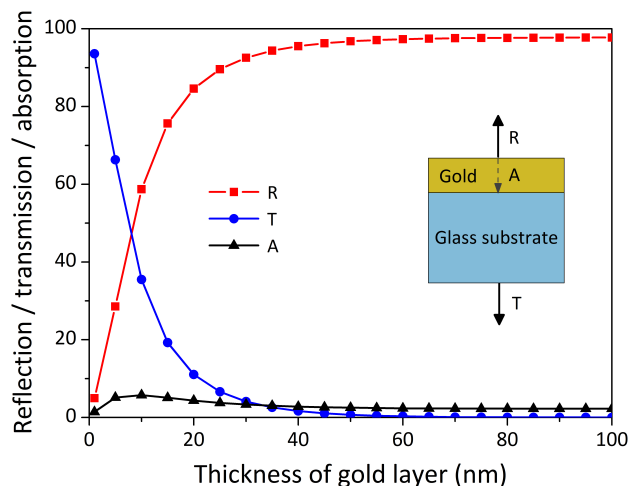


Figure 6.1: Plot of the reflection (R), transmission (T), and absorption (A) as function of the film thickness of gold deposited on a glass substrate.

At very low thicknesses of gold (few nanometers), the absorption is negligible and the layer is mainly transparent. At a film thickness of 10 nm, transmission and reflection are equal and the absorption is maximal. Towards thicknesses of 50 nm, the transmission approaches zero, while the absorption maintains a finite value and the reflectivity increases. The need for a minimum thickness combined with a high transmittance of the FP filter at resonance is a common trade-off for metal-based FP interferometers [Wolffenbuttel, 2004]. To allow sufficient transmission through the layer, film thicknesses >20 nm were considered in the experiments.

I considered static FP filters consisting of either two gold reflectors or two high contrast grating mirrors, all coated on a glass substrate (Figure 6.2). Initially, the cavity space was filled with a polymer (Figure 6.2a), but later on filled with air (Figures 6.2b,c). I used RCWA to obtain the respective filter response (bottom of Figure 6.2). Common simulation parameters were a cavity spacing of $10 \mu\text{m}$ with an index of either 1 (air) or 1.57 (polymer), normal incidence with a TM-polarised wave, and the cover and substrate materials of the entire filter being glass. The dispersion and the absorption of glass were neglected in the simulation, but they were included for the gold (optical constants taken from reference Filmetrics [2014]) and the amorphous silicon (taken from ellipsometry measurements on PECVD a-Si, see Chapter 3). Furthermore, conservation of energy requires that the peak transmission T is equal to $1 - R - A$. The critical parameter for the metal-based FP filter is the thickness of the gold layer; hence Figures 6.2a and 6.2b show different transmittance curves for gold thickness levels between 5 and 50 nm. The larger optical path in

Figure 6.2a reduces the free spectral range (Equation 2.16) of Chapter 2) compared to that of Figure 6.2b, which is clearly apparent. The impact of thicker gold layers is clearly visible from both plots as the actual peak transmittance decreases steadily with increasing thickness as a result of the increasing absorption.

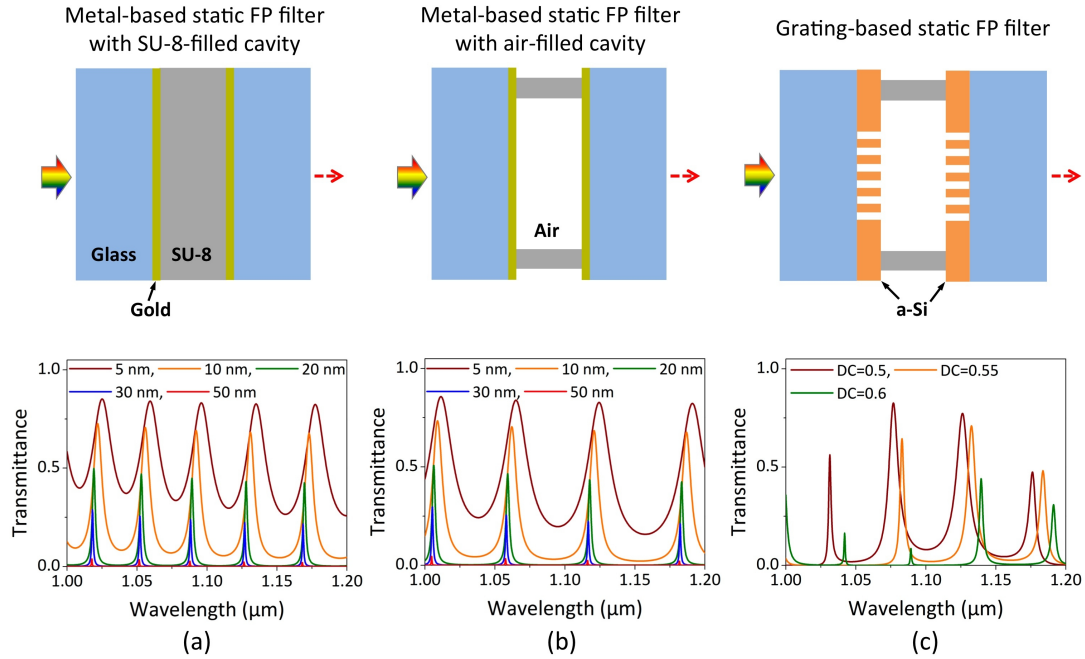


Figure 6.2: Schematics of different FP filter geometries (top) and their responses (bottom, RCWA) for cavity lengths of $10 \mu\text{m}$ and TM-polarised plane-wave incidence. (a) Metal-based static FP filter with polymer-filled cavity. (b) Metal-based static FP filter with air-filled cavity. (c) Grating-based static FP filter. Note that the drawings are not to scale.

A good compromise between moderate transmittance and narrow peak width is found for thicknesses around 20 nm . For the grating-based filters, the duty cycle (DC) is the most sensitive parameter and the most difficult to control during fabrication, hence I studied the FP transmittance for several duty cycles (Figure 6.2c); a duty cycle variation of $\sim 15\%$ results in a resonance peak shift of $\sim 12 \text{ nm}$. The peaks appear much sharper although the overall peak transmittance remains at a similar level as for the metal-based filters. Naturally, the simulations assume plane wave input light; for input light with an angular distribution, the peaks are expected to broaden somewhat as the resonance wavelength shifts with angle. In practice, a very thin (5 nm) layer of chromium is sandwiched between the glass substrate and the gold film to enhance the gold adhesion. The effect of a 5 nm layer of chromium (optical constants taken from reference Johnson and Christy [1974]) on the FP response is shown in Figure 6.3.

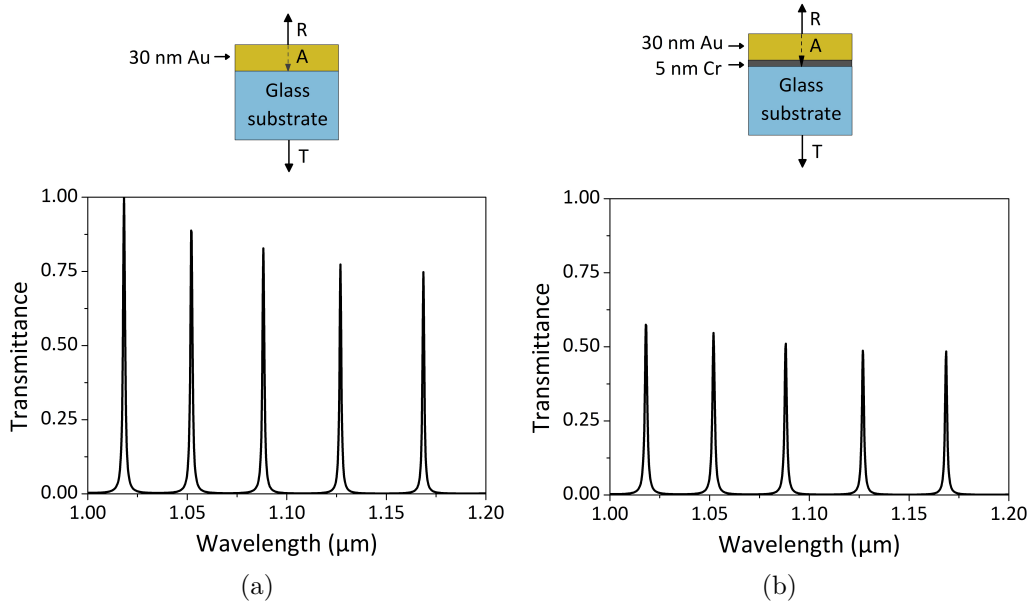


Figure 6.3: Comparison of the FP transmittances between a 30 nm gold film on glass (a) and the same sample including the effect of a 5 nm chromium film sandwiched between the gold and the glass (b). Note that the drawings are not to scale.

We note that the width of the resonance peaks remains unchanged in both configurations. But the amplitudes of the peaks in the chromium-gold sample decrease in a range between 25% and 43% due to the significant absorption in the chromium layer between 1 and 1.2 μm .

6.2 Fabrication of static FP filters

The process flows for building static Fabry-Pérot cavities are in Figure 6.4 for the case of metal-metal (a) and for the case of grating-grating (b) mirrors. The workflow for the metal-based static FP devices (Figure 6.4a) begins with cleaning of the glass substrates followed by the deposition of a 5 nm layer of chromium for adhesion followed by the layer of gold; these metals were deposited in an electron-beam evaporator (step 2). The spacer was fabricated by spin-coating a mixture in the ratio 2:1 of SU-8 2050 and SU-8 2000.5, pre-baking, UV exposure through a mask defining the spacing bars, post-baking, and development, all summarised under step 3 in the figure (further details of the recipe are described in Chapter 3). In case of the FP with a uniformly SU-8 filled cavity (Figure 6.2a), the exposure and development steps were omitted. The height of the bars was measured using a surface profilometer prior to bonding the two pieces together to form the cavity. The processing for the

grating-based FP filter involves a few additional steps (Figure 6.4b). We received the glass substrates coated with amorphous silicon from collaborators at Tyndall National Institute; either electron-beam evaporation or PECVD was used for the deposition. For the definition of the sub-micron gratings, an electron-sensitive resist (ZEP 520A) was spin-coated (step 2), baked, and exposed to the corresponding electron dose (step 3). Since ZEP 520A is a positive resist, the exposed areas become soluble in the developer Xylene (step 4) and the unexposed areas remain and then act as an etch mask during the silicon dry etch (step 5). After the remaining resist has been stripped off (step 6), the SU-8 mixture is spin-coated (step 7) on one of the two grating samples at three spin rates, depending upon the desired thickness. The spun layer was pre-baked, exposed to UV light (step 8), post-baked, and developed (step 9), revealing the spacing bars surrounding the central grating area on sample 1 (see also Figure 6.9a). In the same manner as for the metal-based FP devices, both grating samples were adhesively bonded together in the final step (step 10). Alignment markers on both samples helped to bond the gratings without any angular offset.

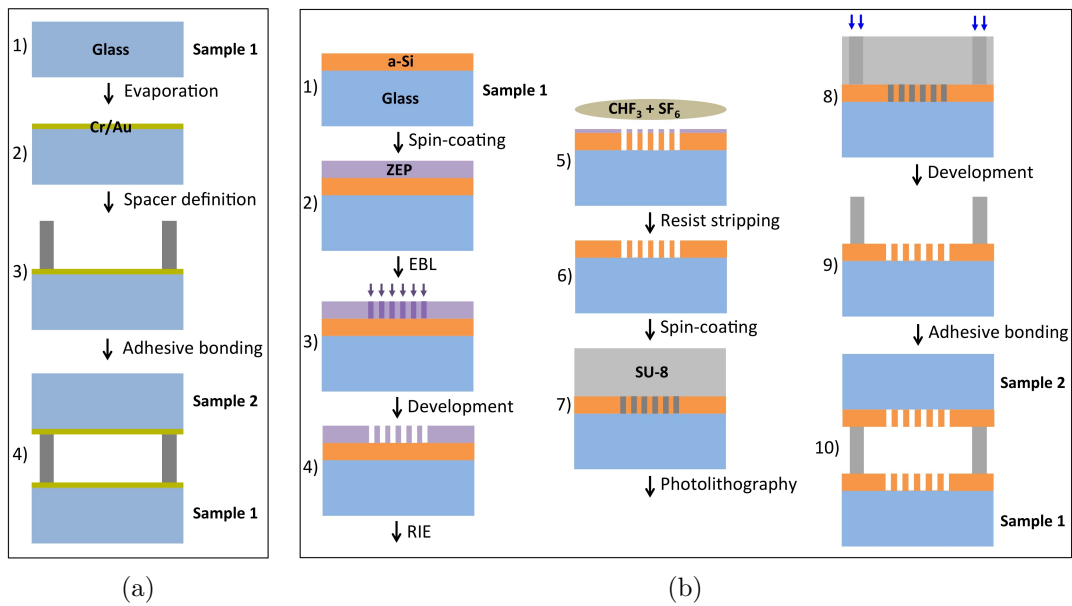


Figure 6.4: Workflow of fabrication of a static FP filter in cross-section based on (a) metal reflectors and (b) a-Si high contrast grating reflectors. Note that the drawings are not to scale.

6.3 Characterisation of static FP filters

For the characterisation of the optical response of Fabry-Pérot filters I modified an existing transmission setup by including the ability to image the sample under study. The setup is shown in detail in Figure 6.5.

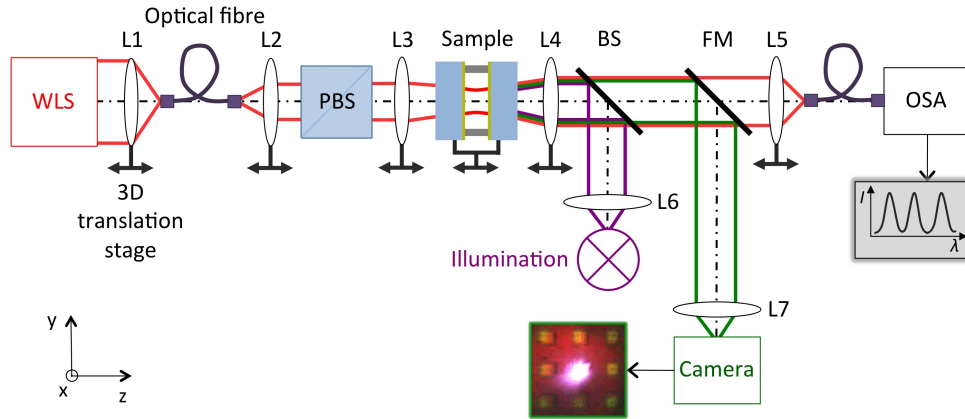


Figure 6.5: Transmission setup for characterising the resonances of a Fabry-Pérot filter. WLS = white light source (supercontinuum), L = lens, PBS = polarisation beam splitter, BS = beam splitter, FM = flip mirror, OSA = optical spectrum analyser, ray traces in red denote incoming radiation, rays in green mark reflected radiation as detected by the camera, purple rays show ray traces of the illumination light. The dashed black line through the optical components indicates the optical axis.

Most of the elements were placed on translation stages to facilitate three-dimensional positioning and to simplify alignment. The beam of the supercontinuum source was coupled into and out of an optical fibre using high- NA microscope objectives (L1, L2) and slightly focussed onto the sample after passing through a polarising beam splitter (PBS) and another lens (L3). The transmitted light was collected by a lens (L4) and coupled into an optical fibre (L5) and an optical spectrum analyser. The alignment was again performed with the auxiliary ASE source. To image the surface of the grating, an imaging setup comprising a CMOS camera with lens L7 and a flip mirror (FM) was added to the setup. I took all transmission measurements with the OSA in a two-step process: one with the sample in place and another without the sample to have a reference and to eliminate any systematic errors. The experimental curves were noise-filtered by using a running mean of ten adjacent wavelengths.

6.3.1 Metal-based Fabry-Pérot filter with polymer-filled cavity

I started with the metal-metal cavity of Figure 6.2a, using a gold thickness of approximately 50 nm and a cavity spacing of $\sim 3.7 \mu\text{m}$ as determined by the thickness of the SU-8 layer. The measured transmittance through this device is shown in Figure 6.6 together with the simulated response. The incident beam was TM-polarised.

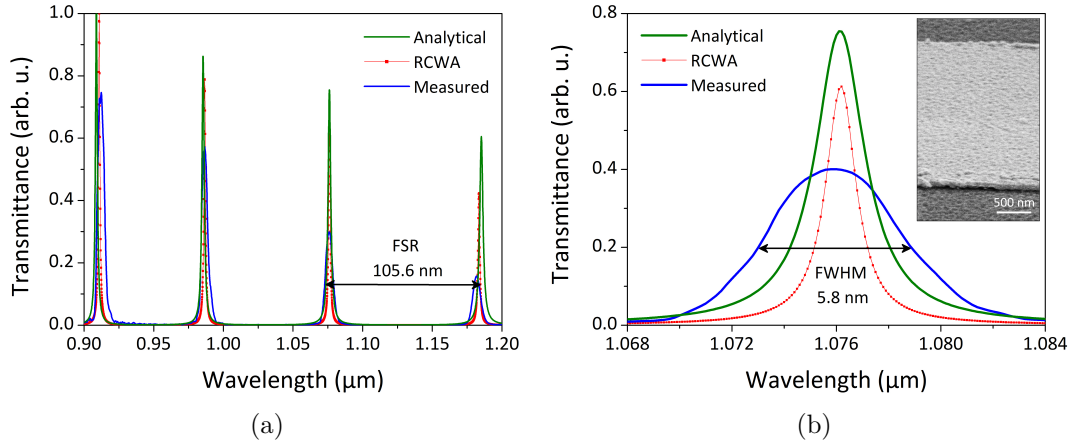


Figure 6.6: (a) Measured transmittance (solid blue) and calculated response by RCWA (red line) and analytical FP theory (green line) of a fabricated FPI consisting of a cavity filled with the polymer SU-8 and two gold reflectors on glass substrates. (b) Close-up view of the main resonance peak around $1.076 \mu\text{m}$. The inset shows an SEM micrograph of a typical gold layer with a significant surface roughness (30° viewing angle).

Figure 6.6 shows four sharp well-separated resonance peaks and the calculated and experimental curves agree excellently across the spectral range. All three curves were normalised to unity due to the lack of a commonly known incident intensity, which is why we cannot infer the absolute height of the peaks. The exact cavity length used in the simulation was adapted to the measured height of the SU-8 spacer of $3.724 \mu\text{m}$. As we are aiming for a resonance wavelength around $1 \mu\text{m}$, (here: $1.076 \mu\text{m}$), the FPI will have to operate in a higher interference order than 1 according to Equation 2.15 in Section 2.3.1 of Chapter 2. In fact, the order m here is 11. Given the estimated reflectivity of gold of approximately 96% of the deposited gold reflectors and taking into account the wavelength-dependent absorption of gold and chromium as well as a phase shift of nearly π adding to the phase term at the output of the FPI, the FP theory predicts the peak separation FSR and the peak linewidth $FWHM$ to be 109 nm and 2.3 nm, respectively, at the resonance wavelength of about $1.07 \mu\text{m}$ yielding a theoretical finesse of 47.4. RCWA calculations gave similar

results. The experimental FSR of 105.6 nm is close to theory, but the measured $FWHM$ of 5.8 nm deviates considerably from the predicted values. Hence, the measured (effective) finesse obtained was 18.2. Given the rather large discrepancy of approximately 60% between the theoretical and experimentally attained finesse, it is instructive to understand the factors impacting on the effective finesse, which are described in the following paragraph.

In practice, the finesse of the FPI is not only described by the reflection finesse, but rather by an effective finesse F_{eff} describing a function of more general validity. The main factors contributing to the effective finesse of the FPI are the mirror reflectivities as given by reflection finesse F_R and the surface quality of the mirrors and the alignment of the incident beam described by the defect finesse F_D (usually an empirical value); as such, they can be added in the following way [Hays et al., 2010, Moon and Shkel, 2001]:

$$\frac{1}{F_{eff}} = \sqrt{\left(\frac{1}{F_R}\right)^2 + \left(\frac{1}{F_D}\right)^2} \quad (6.1)$$

It is important to note that the optical performance of a real FP device is limited by the imperfections of the mirrors as they usually deviate from perfect flatness and perfectly plane parallelism [Hecht, 2002] and/or feature slight aberrations and surface irregularities. In fact, the authors of references [Chabbal and Jacobi, 1958, Roychoudhuri and Hercher, 1977] have explained the broadening of the ideal transmission peak by a convolution of slightly different cavity spacings due to the surface imperfections of the mirrors. In most cases, though, the defect finesse is assumed to be larger than the reflective finesse, thereby diminishing its impact on the effective finesse. On the other hand, if one can afford to compromise on the value of the reflective finesse, the contributions from the defect finesse become less stringent [Wilksch, 1985].

Investigations of the evaporated gold layer via scanning electron microscopy (see inset of Figure 6.6b) revealed a non-negligible surface roughness (on the order of $\sim \lambda/20$), which may be caused by contamination during the evaporation process, which in turn reduces the quality of the mirror. As the reflective finesse cannot be smaller than the effective finesse (according to Equation 6.1), the actual mirror reflectivity is between 92% ($F_R \sim 18.7$) and 96% ($F_R \sim 52.6$). Considering the fringe broadening, which arises partly from the surface roughness of the mirrors, but also

from the angular dispersion and finite size of the illuminating beam [Lee et al., 2002], I conclude that the defect finesse is the dominating quantity in this device. Hence, the reflectivity must be above 92%. In addition to the mirror and beam properties, the dissipative losses present in the metal mirrors contribute to further attenuation of the transmitted amplitudes.

6.3.2 Metal-based Fabry-Pérot filter with air-filled cavity

The transmittance plots for a similarly fabricated FPI are illustrated below (Figure 6.7), again using TM-polarisation. This time, the cavity was filled with air (see Figure 6.2b) whereby the spacing after fabrication was $20.54 \mu\text{m}$ and the thickness of the gold layer was approximately 70 nm . The spacer was defined by two parallel bars photolithographically at the edges of one chip, while the beam was launched through the air-filled region of the cavity.

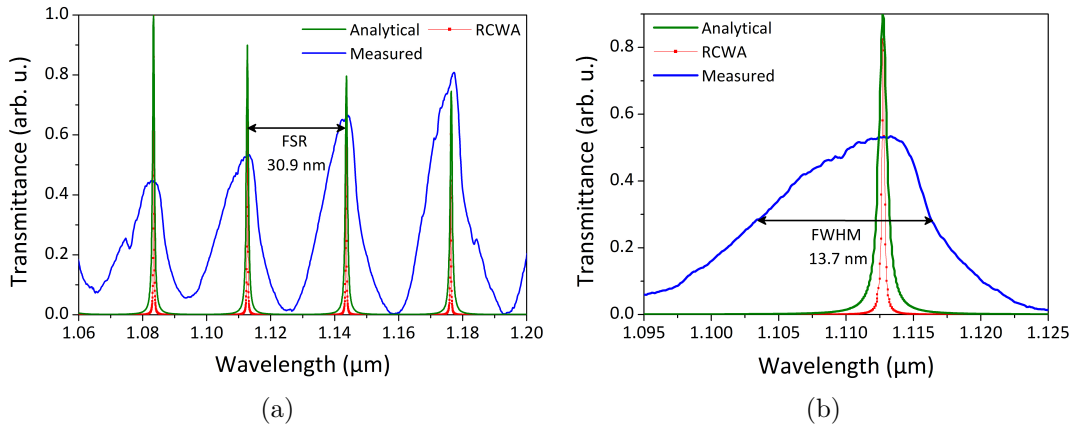


Figure 6.7: (a) Measured transmittance (solid blue) and calculated response by using RCWA (red line) and analytical FP theory (green line) of a fabricated FPI consisting of an air-filled cavity and two gold reflectors on glass substrates. (b) Zoomed view of (a) of the main resonance peak around $1.11 \mu\text{m}$.

Owing to the larger cavity length of $20.54 \mu\text{m}$, a higher number of resonance peaks was observed here, whose central peak positions agree perfectly with the simulated ones. Again, an additional phase shift of about π was included in the analytical treatment and all three curves were normalised to unity. The width of the peaks in the analytical calculation was slightly larger than in the RCWA due to the practically estimated reflectivity of 93% for the gold mirrors, while RCWA took into account the ideal value of 97%. We chose a target resonance wavelength of about $1.11 \mu\text{m}$, which corresponds to an interference order of $m = 37$. The theoretical FSR ,

$FWHM$, and F_{eff} were predicted to be 31 nm, 0.8 nm, and 38.8, respectively. For the fabricated device, the measured FSR of 30.9 nm matches excellently while the $FWHM$ of 13.7 nm and the F_{eff} of 2.3 are strongly deviating from the desired values. The significant broadening (17-fold) is largely attributed to an imperfect parallelism of the two mirrors, verified by a measured height difference of approximately 10% between the two SU-8 bars prior to the bonding, in conjunction with a finite-sized and non-normal beam illumination [Lee et al., 2002]. Since we know that the reflective finesse is between 18.7 and 52.6, and the experimental finesse was 2.3, it follows that the defect finesse F_D dominated the optical performance of this FPI. The asymmetric profile of the resonance peaks with a longer tail on the side of shorter wavelengths also indicates gradual variations in the cavity spacing [Tran et al., 1996].

6.3.3 Grating-based Fabry-Pérot filter with air-filled cavity

In order to study the optical performance of a grating-based FP interferometer, two high contrast gratings based on evaporated amorphous silicon deposited on glass substrates were bonded to each other and tested. The space between both mirrors was filled with air and $5.1 \mu\text{m}$ in distance, which was defined by two parallel SU-8 bars at the edges of one chip. The incident polarisation was TM. The measured and simulated transmittances through this FPI are shown in Figure 6.8.

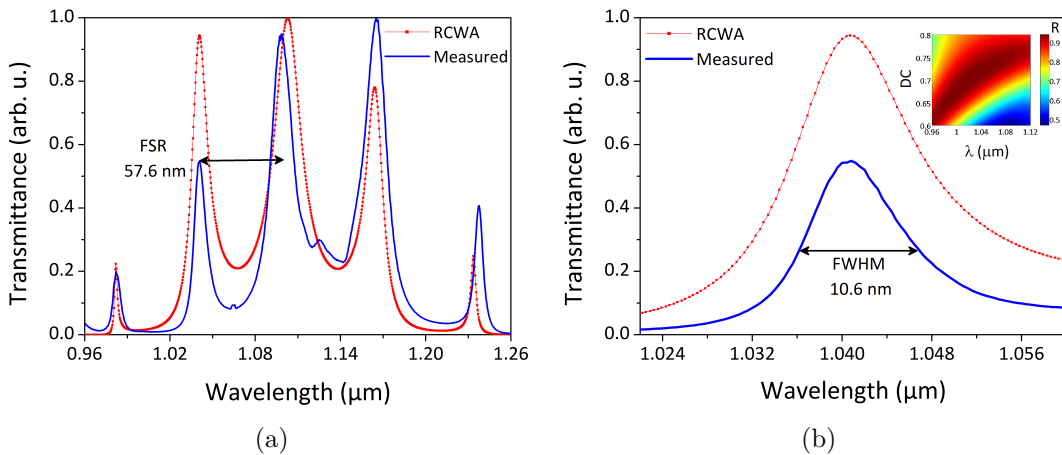


Figure 6.8: (a) Measured (solid blue) and calculated (red line) transmittances of a FP filter consisting of an air-filled cavity and two periodic grating mirrors based on evaporated amorphous silicon on glass substrate. (b) Zoomed view of (a) of the main resonance peak around $1.04 \mu\text{m}$. The inset shows the limited tolerance of the duty cycle in the high-reflectivity region of one grating sample.

Due to its excellent suitability for characterising wavelength-scale gratings, RCWA was used to compare the theoretical filter performance with the experiment. To match the peak wavelengths between both curves, the values used in the simulation were adjusted to the fabricated device parameters and both graphs were normalised to unity. Both fabricated gratings had a periodicity of 514 nm, a duty cycle of 0.7, and a thickness of 360 nm. Given these parameters and including the dielectric function of a-Si, RCWA simulations estimated the reflectivity to be around 90%. The inset of Figure 6.8b highlights the limited tolerance of the duty cycle; already a deviation of 5% in the duty cycle may result in more than 10% decrease in reflectivity. The interference order for a spectral resonance around 1.04 μm was 13. Overall, the signal and the RCWA calculation are in very good agreement with each other; the theoretical FSR , $FWHM$, F_{eff} were 62.4 nm, 4.8 nm, and 13, respectively, compared to the measured values of 57.6 nm, 10.4 nm, and 5.5. The reflective finesse was approximately 12.6 ($R = 0.9$), indicating again the significance of F_D . As the refractive index of evaporated a-Si had not been characterised by spectroscopic ellipsometry, the experimental index data of PECVD a-Si were taken as an approximation. One reason for the wider simulated transmission peak at 1.04 μm is this deviation of the dielectric function of evaporated a-Si from the expected values (data of PECVD a-Si). Additionally, the observed broadening in the measured spectra is related to non-uniformities in the thickness and surface roughness of the a-Si (as verified in SEM images) as well as a slight non-parallelism between both reflectors.

Compared to the static Fabry-Pérot interferometer based on evaporated amorphous silicon high contrast gratings, a similarly fabricated device based on PECVD a-Si gratings showed the following response (Figures 6.9c,d). This time the SU-8 spacer was defined by a pattern of four bars connected to a frame and leaving an air-space at the centre. In this way, a possible leakage of SU-8 into the cavity space could be avoided during bonding and a better uniformity of the spacing was expected. In addition, alignment markers on both samples aided in matching both gratings above each other during adhesive bonding (Figures 6.9a,b), thereby avoiding any angular misalignment. In the transmission setup used (see Figure 6.5), the incoming beam onto the FP chip could not be launched perfectly collimated, as this resulted in very noisy spectra while approaching the detection limit of the OSA. However, to diminish the angular dispersion of the incoming beam, the high- NA focussing lens ($f = 1$ mm) in front of the sample was replaced with a smaller- NA lens ($f = 75$ mm). A difference to the previous grating-based FP sample was the significantly increased spacing (26.9 μm) despite the approximately comparable recipe

to define the SU-8 spacer. This device, however, was made in the cleanroom facilities of the University of York, which operates at different humidity and temperature conditions than the cleanroom at St Andrews.

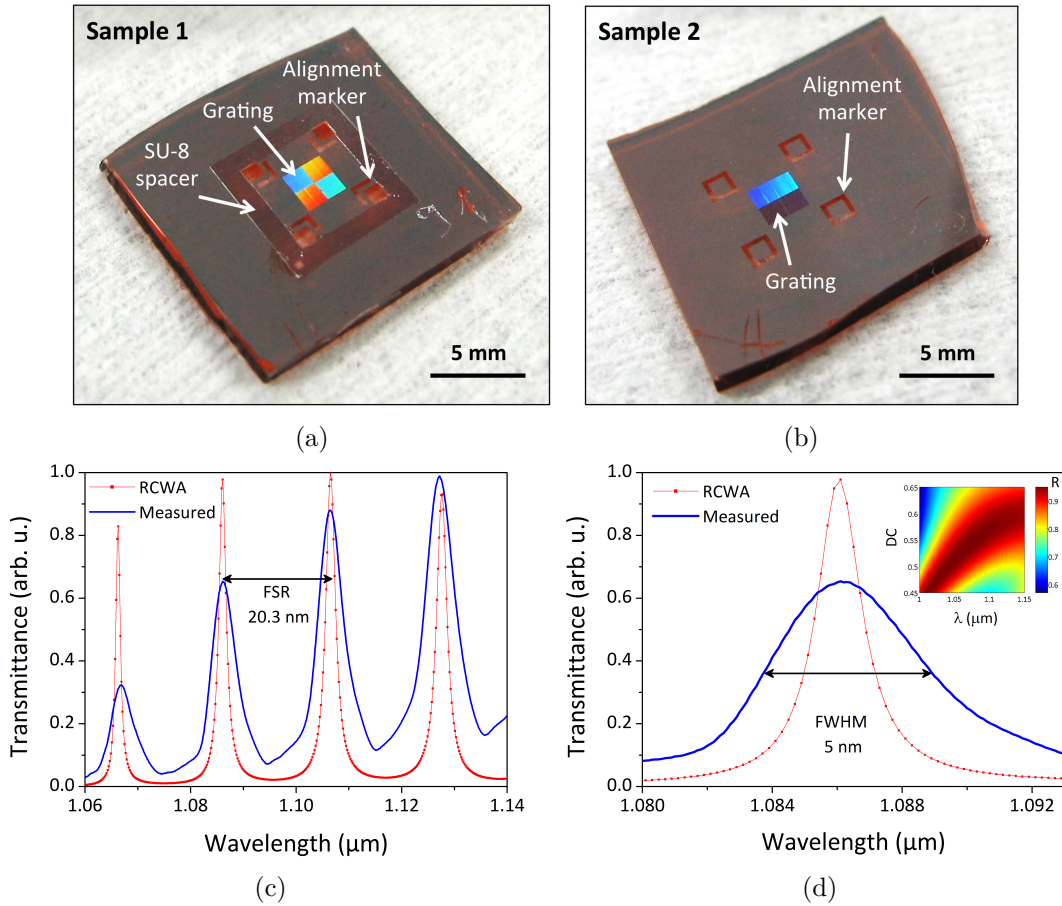


Figure 6.9: Two fabricated samples containing grating reflectors at their centres prior adhesive bonding: (a) Sample 1; (b) Sample 2. (c) Measured (solid blue) and calculated (red line) transmittances of a FP filter consisting of an air-filled cavity and two periodic grating reflectors based on PECVD amorphous silicon on glass substrates. (d) Close-up view of the main resonance peak around $1.127 \mu\text{m}$. The inset shows the limited tolerance of the duty cycle in the high-reflectivity region of one grating sample.

The fabricated grating values used in the RCWA simulation were a period of 680 nm , duty cycle of 0.55 , and an a-Si thickness of 360 nm . From theory, the FSR , $FWHM$, F_{eff} were 20.4 nm , 1.7 nm , and 12 , respectively, compared to the measured values of 20.3 nm , 5 nm , and 4.1 , respectively. For an estimated reflectivity of 90% of each grating sample (considering the quality issues of the deposited material as described in Chapter 3) and an interference order of $m = 50$ around the resonance

peak at $1.086 \mu\text{m}$, the reflective finesse results in 13.3, which is again considerably deviating from the effective finesse. Despite the smaller angular dispersion of the incoming beam, the finesse ($F_{eff} = 4.1$) could not be improved compared to the previous grating-based FP filter ($F_{eff} = 5.5$). Although the index variations of a-Si between simulation and experiment should be much smaller in this sample, mainly the beam divergence and possibly a slight non-parallelism between the reflectors controlled the overall attainable finesse. Also here, slight deviations in the real duty cycle had a large impact on the practical reflectivity of the grating mirror (see inset of Figure 6.9d). Generally, it is found from literature [Wolffenbuttel, 2004] that the effective finesse of micromachined silicon devices is typically limited to 50 due to predominance of the defect finesse; hence there is room for improvement of the a-Si grating-based filters presented here.

6.4 Summary

I built several types of low-finesse Fabry-Pérot devices, starting from a metal-based filter over to embedding grating mirrors within the cavity. The compact dimensions make them suitable for tuning applications as follows in the next chapter. Table 6.1 summarises the attained optical performances of the aforementioned static Fabry-Pérot filters in comparison with the expected values of FSR , $FWHM$, F_{eff} , central wavelength λ_c , and interference order m .

Table 6.1: Summary of all fabricated static Fabry-Pérot filter types. Values in curly brackets denote values calculated by RCWA.

Type of FP filter	FSR (nm)	$FWHM$ (nm)	F_{eff}	λ_c (μm)	m
Metal-based FPI with polymer-filled cavity	105.6 {108}	5.8 {2.3}	18.2 {47.4}	1.076	11
Metal-based FPI with air-filled cavity	30.9 {31}	13.7 {0.8}	2.3 {38.8}	1.11	37
Grating-based FPI with air-filled cavity (evaporated a-Si)	57.6 {62.4}	10.4 {4.8}	5.5 {13}	1.04	13
Grating-based FPI with air-filled cavity (PECVD a-Si)	20.3 {20.4}	5 {1.7}	4.1 {12}	1.086	50

Generally, it was difficult to exceed an effective finesse of 20 in the experiments. Many loss-inducing factors contributed to the experimental results and lowered the actual reflectivity of the mirrors. It was easier to control the spacing between the two mirrors when using a complete layer of SU-8 rather than displaced spacer bars, which is the reason for the superior finesse for the metal-based FPI without air in the cavity and the highly symmetric shape of the resonance peaks (Figure 6.6). Whenever the spacers were fabricated as displaced bars or frame, their heights were deviating up to 10% leading to a significant non-parallelism between both reflectors after bonding, which in turn degraded the attainable finesse of the filter device. However, the highly dispersive incident beam degraded the peak width more severely leading to predominant defect finesse values and thus limited the optical performance of the fabricated filters.

Assuming that issues such as beam alignment, contamination within the functional layers, and mirror quality could be resolved and improved by ultra-clean microprocessing, at least an order of magnitude increase in the attainable finesse is expected. The Fresnel reflection loss at the air-silicon interface is substantial and could be improved by applying anti-reflective coatings.

7 Tuneable MEMS Fabry-Pérot filter based on high contrast gratings

The goal of this chapter is to develop a tuneable Fabry-Pérot filter based on high contrast gratings embedded in an optical microelectromechanical system (optical MEMS or MOEMS) using the fabrication capabilities available. Following up on the expertise obtained from designing and making static Fabry-Pérot filters (Chapter 6), the displacement of a flexible membrane is utilised to change the cavity spacing, which in turn shifts the transmitted filter wavelength. For ease of implementation and testing of the actuating system, both reflectors were initially coated with metal of which one was a flexible silicon nitride membrane. Upon successful realisation, one metal mirror was replaced with a reflector based on a-Si high contrast gratings to form a hybrid metal-grating MEMS FP filter. Section 7.1 explains the design issues and the prerequisites for making the filter device including a finite element analysis of different spring-like suspensions of a membrane, followed by a detailed description of all the fabrication issues I was facing, given in Section 7.2. The optical and the electromechanical characterisation of a working metal-based tuneable MEMS filter along with the description of silicon grating-based filters are shown in Section 7.3. The results of this chapter are then summarised in Section 7.4. Based on the preliminary work on silicon-based MEMS filters shown in this thesis, we have also published a paper on a tuneable MEMS filter, which employs grating mirrors made from silicon nitride for operation at visible wavelengths [Wang et al., 2014].

7.1 Concept and simulation of tuneable MEMS FP filters

Upgrading a static Fabry-Pérot filter to a microelectromechanical system requires one mirror to be moveable. At the beginning of my project, the expertise in the area of MEMS within our research group was non-existent, so I developed the process and learned the terms, constraints, and design guidelines for MEMS devices. I used the

design rules put forward by a group in Berkeley [Mateus et al., 2005] highlighting the parameters and scaling of wavelength-tuneable optical filters, the detailed review paper of Mroziewicz [2008] about external cavity wavelength-tuneable semiconductor lasers, as well as the essential input and requirements of our project collaborators at Tyndall in Cork, Ireland, and at Nicolaus Copernicus University of Torun, Poland. The ultimate target was to prove the feasibility of incorporating high contrast gratings as the functional component into the filter device, thereby eventually enhancing the performance of existing tuneable MEMS filters, which are usually based on multilayer Bragg stacks [Domash et al., 2004, Flanders et al., 2003, Irmer et al., 2003, Mateus et al., 2002].

7.1.1 Design considerations

Prior to the development of a tuneable optical filter, there were several factors to consider: the operational principle of the actuator and the driving power, the tuning range and speed, the materials choices, the size, the desired optical performance in terms of the finesse or quality factor, but also qualitative issues such as the long-term stability, flatness of the membrane layer, reliability, and parallelism between the high-reflectivity mirrors.

First, we decided on the type of actuation and the different materials at hand. As the wavelength of the transmitted radiation of the filter depends on the gap size between the two Fabry-Pérot mirrors, we chose to tune the gap with the electrostatic-type actuation by metallising both mirrors of which one is deposited on a flexible membrane. When a voltage is applied across the filter, electrostatic forces serve to attract or repel the two mirrors and change the cavity length. It is well known in MEMS technology that the amplitude of deflection is limited to less than 1/3 of the initial gap size between both capacitive plates [Madou, 2012]. An electrostatic deflection beyond this value will collapse the suspended area towards the counter electrode and cause a snap down (stiction); the corresponding voltage in this case is called the pull-in voltage and is defined as:

$$V_{pull-in} = \sqrt{\frac{8k_s d^3}{27\epsilon_0 A}} \quad (7.1)$$

Here, k_s is the spring constant of the deflectable material, d the gap size or cavity spacing, ε_0 the permittivity of free space, and A the overlap area of the conductive plates within the central optical cavity.

In order to be moveable, one mirror needs to be flexible, so it is usually made out of a thin film of silicon, polymers, or silicon nitride [Madou, 2012]. Owing to their robustness and compatibility with our fabrication facilities, we decided to use commercially available square membranes of 100 nm silicon nitride thin films (Norcada Inc.) to serve as the moveable part of the FP filter (Figure 7.1).

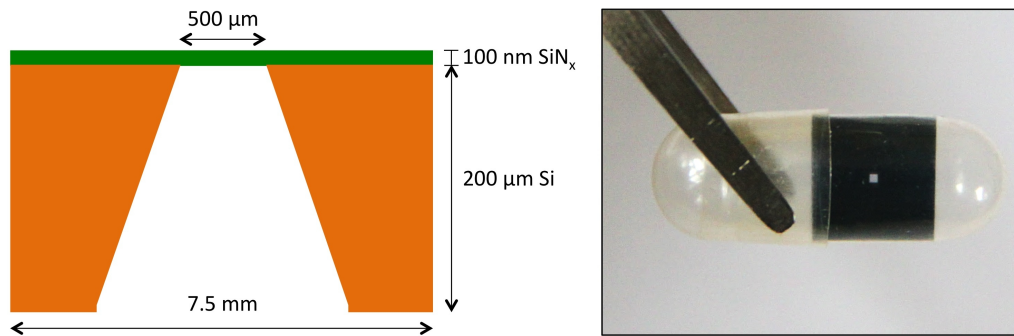


Figure 7.1: Left: Layout of the silicon nitride membrane samples purchased from Norcada Inc. (not to scale). Right: Photograph of a membrane sample.

The central square of the silicon nitride membrane window had a size of $500 \times 500 \mu\text{m}^2$, whereby the suspended layer was carried by a $200 \mu\text{m}$ thick silicon frame with a total chip size of $7.5 \times 7.5 \text{ mm}^2$. The silicon-rich silicon nitride membranes (SiN_x) have very low stress with $<250 \text{ MPa}$, which makes them relatively robust and suitable for MEMS applications; in comparison, conventional stoichiometric silicon nitride films (Si_3N_4) exhibit an intrinsic tensile stress around 1 GPa [Temple-Boyer et al., 1998, Van Zeijl and Nanver, 2005].

The filter should be of transmission-type, which implies the use of a transparent substrate at the near-infrared wavelength, and its fabrication should be compatible with the tools available in our facilities. As the final FP filter is a rather complex device, I started by making tuneable MEMS FP filters that consist of two metal-based mirrors (Figure 7.2). One of the metal layers was coated on a solid glass substrate, whereas the other one was deposited on the flexible membrane, thereby getting experience in handling the fragile silicon nitride membrane. As already mentioned in the previous chapter, I used gold due to its high reflectance at near-infrared wavelengths. Based on the RCWA calculation (Figure 6.1 of Chapter 6) assessing the gold thickness and its absorption loss and on the fact that minimum stresses for

MEMS micromirrors occur beyond a gold thickness of approximately 30 nm [Ilic and Goossen, 2004], I chose 30 nm as the mirror thickness. The fabrication-specific details for this filter follow in Section 7.2.

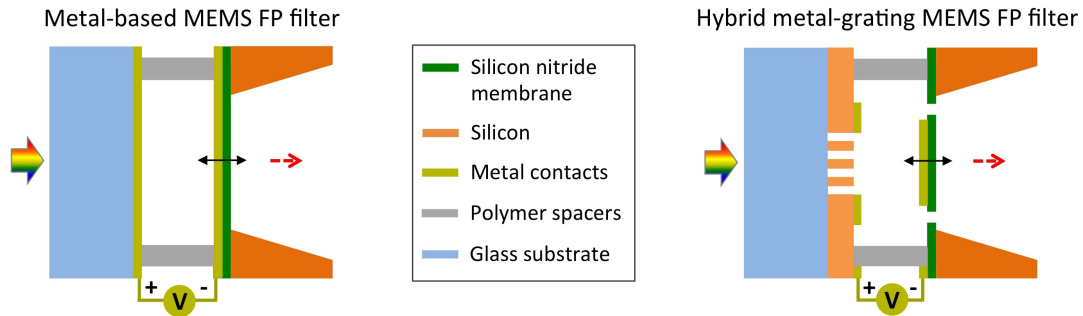


Figure 7.2: Schematics of the tuneable MEMS FP filters produced in this work (not to scale). Left: Metal-based filter. Right: Hybrid metal-grating filter.

The next step was to incorporate the high contrast gratings: our initial concept envisaged to use grating mirrors on both sides. On the membrane side, we assumed that the silicon nitride would act as a robust carrier for a thin film of a-Si into which we planned to etch the grating. This plan was abandoned, however, as we were not able to obtain low-stress amorphous silicon. As discussed in Section 3.1.2 of Chapter 3, the deposition of amorphous silicon by electron-beam evaporation or by plasma-enhanced chemical vapour deposition always resulted in wrinkling and buckling of the membrane. We therefore decided to coat the membrane with a metal layer and placed the silicon grating on the rigid glass substrate (Figure 7.2b). In the long run, we envisage the application of a grating-based tuneable MEMS filter in swept-source optical coherence tomography, for which stringent performance parameters exist. At the start of my project, our desired values for a useful filter were defined by existing devices [Chang-Hasnain, 2000, Flanders et al., 2003, Hays et al., 2010, Irmer et al., 2003]; these included the operation in the spectral window between 1-1.3 μm , a resonance peak linewidth of less than 1 nm, tuning speeds in the upper kHz regime, and tuning ranges above 50 nm, while keeping actuation voltages low.

7.1.2 Membrane suspension designs and stress modelling

The silicon nitride membranes are square diaphragms that are suspended on a silicon substrate. To increase the flexibility of the membrane and to facilitate actuation, I analysed different types of membrane suspension patterns that are found

in the literature [Flanders et al., 2002, Hays et al., 2010, Kronast et al., 2014]. In doing so, it is important to obtain estimates of the displacement, uniformity, and stability of the membrane upon actuation. A very common approach for studying microelectromechanical structures is the finite element method (FEM). With this method, the object under study is divided into small mesh elements, for which mechanical equations and constraints at each boundary are calculated and then combined across all mesh elements to find the final solution. In general, the finer the mesh, the more accurate the solution will be, with the calculation computationally more intense.

As it was readily available, I used the MEMS module of the commercial software COMSOL Multiphysics to calculate the deformation of a low-stress silicon nitride membrane with a thickness of 100 nm for different suspension designs. The aim of the simulations is to find a design that achieves very low residual stress of the suspended membrane layer while enabling highly uniform and high deflections. The main goal of this modelling exercise is to provide an indication of the mechanical behaviour of the membrane rather than specifying all of the MEMS-relevant terms. As such, I simplified the simulations by studying the displacement solely by taking into account pre-stress levels and leaving out any electrostatic parts. All designs considered had the same central width or diameter of $300\ \mu\text{m}$ and the same outer dimensions of $500 \times 500\ \mu\text{m}^2$ for ease of comparison. The width of the anchoring arms was $50\ \mu\text{m}$ (except for the meander-like structure with $20\ \mu\text{m}$) and they were stretching out to $100\ \mu\text{m}$. Given that the silicon nitride membranes feature an intrinsic stress below 250 MPa (Norcada Inc.), the initial normal stress was set to 150 MPa in all designs to allow for a small margin. The mechanical data for the silicon nitride were taken from the COMSOL material library, i.e., a Young's modulus of 250 GPa, a Poisson ratio of 0.23, and a density of $3100\ \text{kg}/\text{m}^3$. In the simulation, the 100 nm thick silicon nitride layer, which is tensile stressed, is divided into two layers, whereby an equal and opposite initial stress level is applied. A large deformation analysis (including non-linear material models) was applied. To illustrate the modelling procedure, I use a $3 \times 3\ \mu\text{m}^2$ suspended membrane, which is anchored by four arms at its edges (Figure 7.3). Once the two-dimensional mesh geometry is set up (here: using 297 elements), a mapped mesh is applied, which is extruded into the third dimension to generate hexahedral mesh elements arranged in two layers (resulting in 594 elements). Pre-stressed areas such as the anchoring arms are then assigned an equal and opposite stress level of 150 MPa within the two layers and the arms are fixed at their ends. In such a static analysis without an externally applied force, the solution is calculated with a direct linear solver and plotted accordingly.

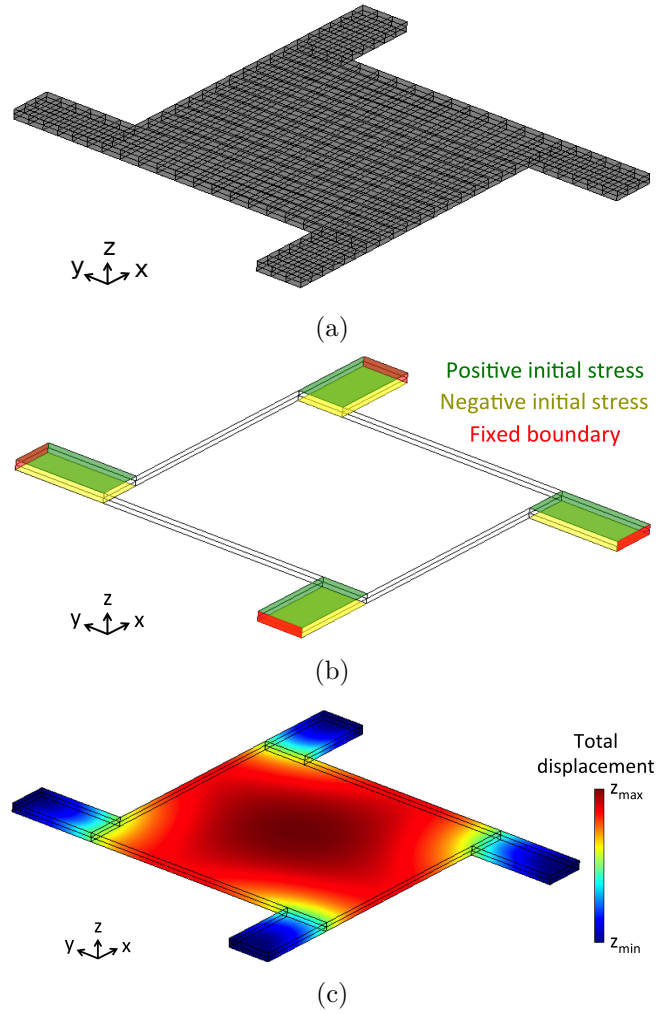


Figure 7.3: FEM simulation procedure of a silicon nitride membrane with four anchoring arms. (a) Three-dimensional view after extruding the mapped mesh. (b) 3D view highlighting the regions of opposite equal stress in yellow (negative initial stress) and green (positive initial stress) and the fixed boundary constraints in red. (c) 3D view of the colour-coded total displacement as solution of the calculation.

Following a literature research on stable and common anchor structures, I studied the following designs: multiple straight legs [Müller et al., 2005], H-shape [Hays et al., 2010], meander-like beams [Kanamori et al., 2007, Martin et al., 2007], and spiral shape [Flanders et al., 2002, Winchester and Dell, 2001]. The results of the simulation are shown in Figure 7.4. The corresponding membrane deformations across the central region of each structure along the x axis (Figure 7.5a) and the y axis (Figure 7.5b) are shown below to highlight any potential differences in each of the directions.

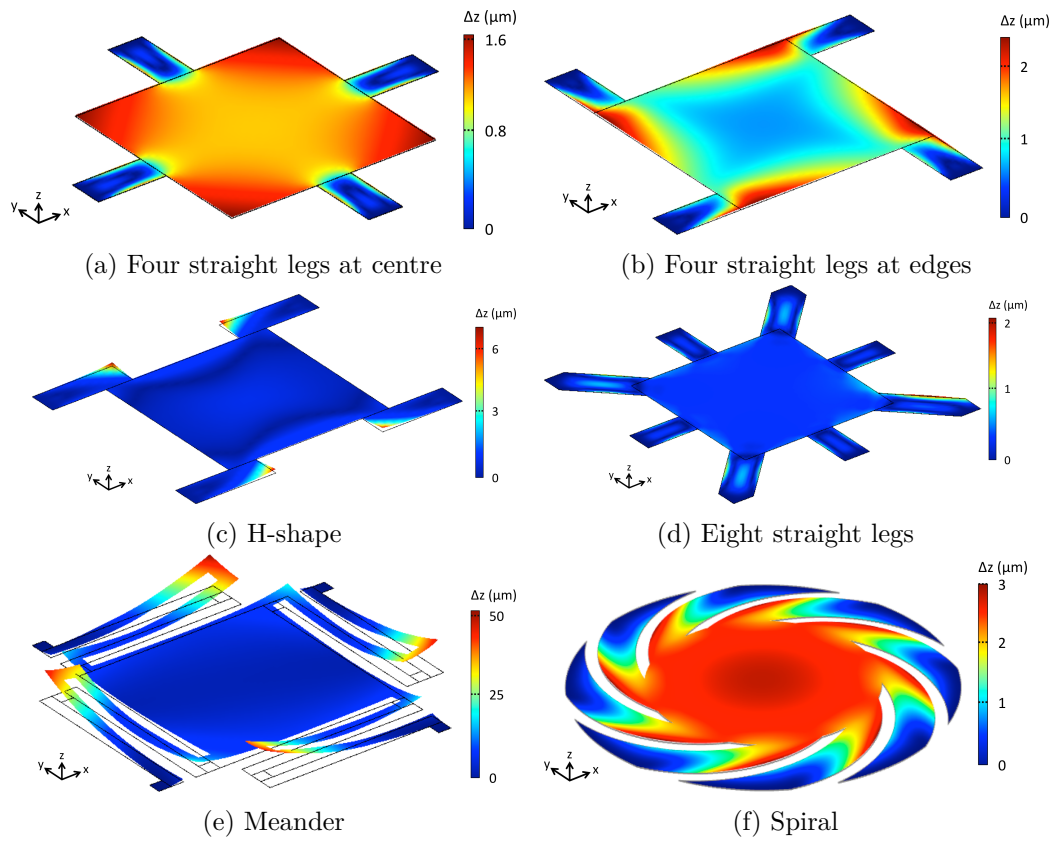


Figure 7.4: Simulation results of six different membrane suspension designs for a silicon nitride membrane with a thickness of 100 nm using the MEMS tool of COMSOL Multiphysics. No external force is applied. The colour bar visualises the total membrane displacement due to releasing the internal stress with the displacement magnitudes indicated for each design.

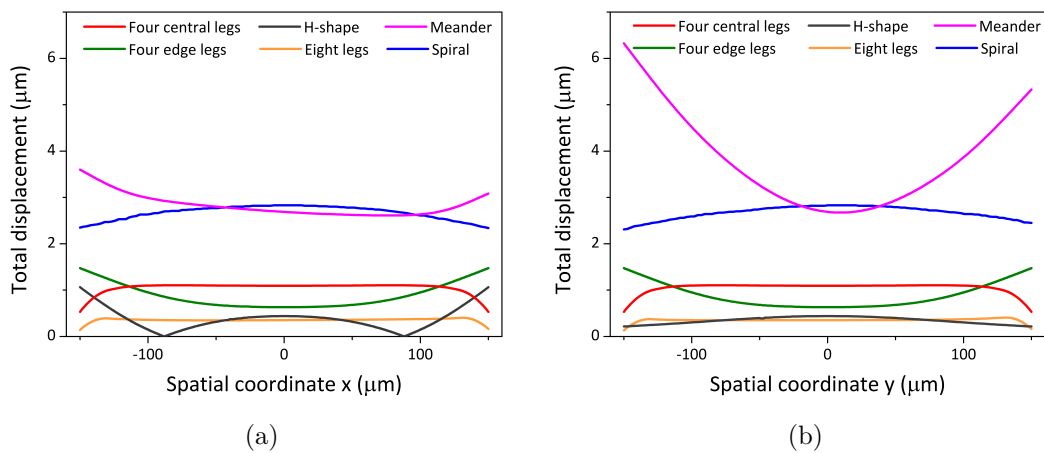


Figure 7.5: Membrane deflection across the central area of all six simulated designs (a) along the x axis and (b) along the y axis.

The MEMS simulations showed that the best combination of displacement and uniformity was achieved with the spiral design (Figure 7.4f), which was then further investigated by my colleague Dr Yue Wang [Wang et al., 2014]. However, the best flatness resulted from patterns with multiple straight suspensions such as the four-central-legs ($\sim 1 \mu\text{m}$ displacement across $230 \mu\text{m}$ along x and y axis) and the eight-legs design ($\sim 500 \text{ nm}$ displacement across $260 \mu\text{m}$ along x and y axis). The maximum stress in the four-central-leg pattern was located at the edges of the central square, whereas it was significantly reduced in the eight-leg design, which in turn made it slightly stiffer. Mounting four suspensions equally at the edges of the central square gave a reasonable deflection of $\sim 700 \text{ nm}$ across $100 \mu\text{m}$ in both lateral directions. In contrast, despite its known stability and stable response to shock [Hays et al., 2010], the deflection in the H-shaped design (Figure 7.4c) was differently distributed across the central region due to its asymmetry. Although the meander-like suspension is very flexible with a maximal deflection of more than $50 \mu\text{m}$ at the suspension arms, the deflection at the region of interest resulted in an uneven distribution along x and y . The good compromise between high flatness and moderate deflection together with expected robustness during processing made me decide in favour of the eight straight leg design.

7.2 Fabrication details for tuneable MEMS FP filters

When I started my PhD project, the fabrication and handling of MEMS devices were not established in our research group. In particular, the membrane samples have to be treated with greater care than the usual silicon chips due to their fragility, vulnerability to contamination, and rapid wear after a few processing steps. For making the FP filter, both mirror samples were processed separately and connected to each other in the final step. The main processing steps were multiple exposures with electron-beam lithography, metal deposition and lift-off, dry etching of the silicon grating and silicon nitride membrane, spacer definition via photolithography on one of the mirror samples, and finally the alignment of both mirrors during the adhesive bonding step. The whole fabrication sequence is relatively time-consuming so that the completion of one filter device took up to a week given the available time slots on machines such as the electron-beam lithography system, which tends to be booked 24/7. The following paragraphs describe the handling of the silicon nitride membranes along with the problems encountered during processing and the fabrication challenges when making the metal- and hybrid metal-grating-based MEMS FP filters.

7.2.1 Silicon nitride membrane

The membranes are very delicate. Simple faults such as flipping the sample upside down, the sample falling onto the front side, or accidentally touching the membrane window with the tip of a tweezer caused immediate damage. Even small cracks in the membrane, which eventually developed during fabrication processing, made a specific sample useless. Furthermore, after having etched the types of anchor patterns shown in Figure 7.4 into the membrane, it could not be loaded by any further processing step (except resist stripping, which was very risky), without causing damage. Hence, I introduced several precautions into the processing sequence.

- For spin coating, I introduced a custom-made carrier plate for the vacuum chuck to hold the membrane in a safe position without the membrane getting sucked in by the vacuum. The centre of the carrier plate was the same size as the membrane chip to maintaining a uniform spinning result while eliminating edge beads.
- Immediately after spin coating, the sample was removed from the carrier plate and cleaned on the backside to avoid sticking to an intermediate glass slide, which was then, together with the sample, put on the hotplate for soft-baking the resist.
- Whenever the sample was immersed in liquid, e.g., for development or cleaning, I only lifted it out in vertical orientation; horizontal removal often caused the membrane to break due to the surface tension of the liquid.

Following patterning and development, the structure was dry-etched in a 1:4 mixture of O_2 and CHF_3 at a -590 V DC bias for 5 min. Figure 7.6 shows the scanning electron micrographs of the fabricated membranes with various anchor patterns as described in the design Section 7.1.2. As predicted by the COMSOL simulations, the corners of the central-four-leg (Figure 7.6a), the H-shaped (Figure 7.6c), and the meander-shaped membrane design (Figure 7.6f) showed high internal stress levels after release with a risk of fracture, while some legs in the edge-four-leg pattern broke off regularly during fabrication (Figure 7.6b).

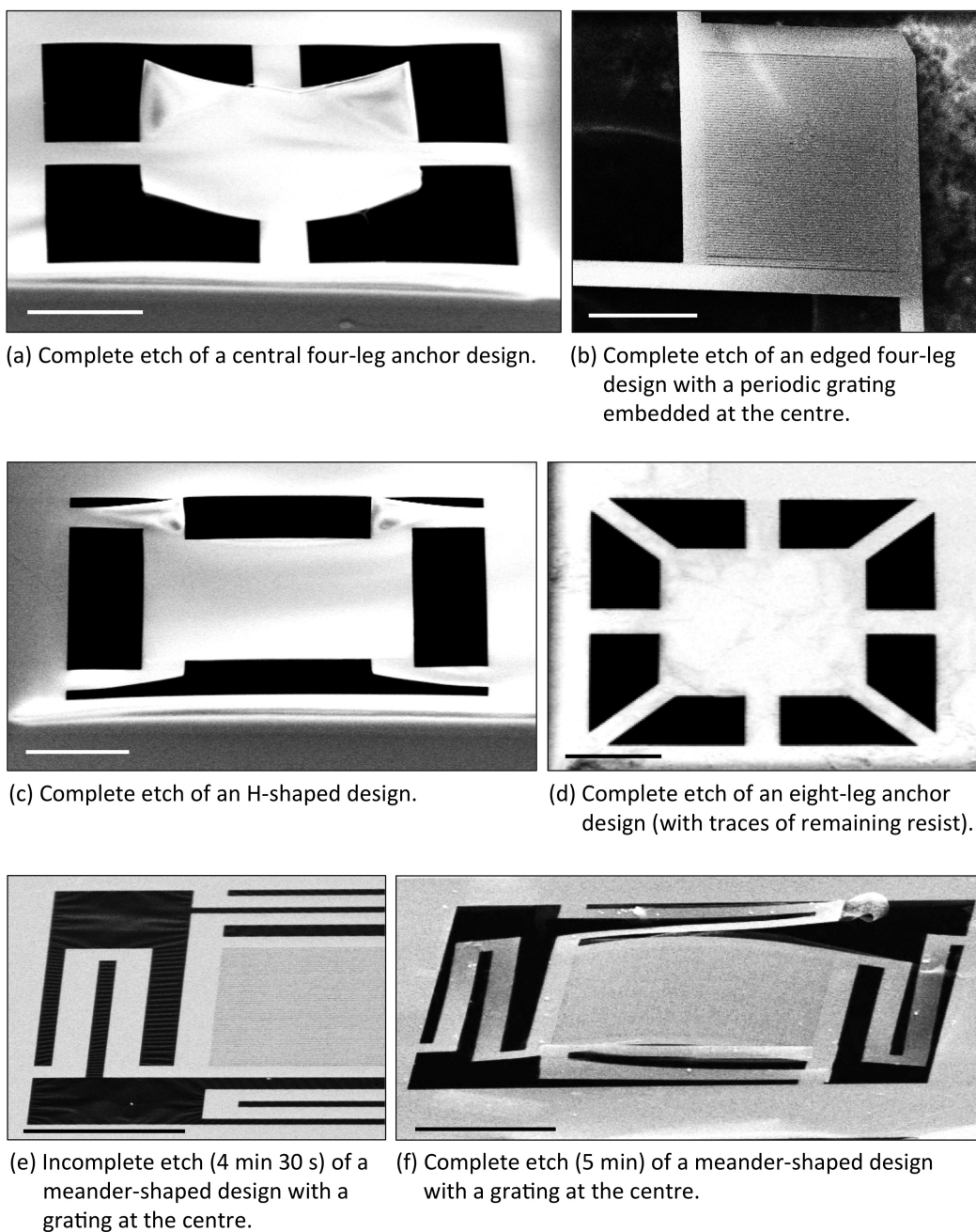


Figure 7.6: Scanning electron micrographs of differently etched anchor designs of the membrane. The scale bar in each image is 50 μm long.

After multiple etch tests, it turned out that anchor patterns with sharp edges caused cracks due to stress concentration (Figure 7.7a), which is in agreement with relevant literature [Ekkels et al., 2003, Wang et al., 2003]; hence sharp corners must

be avoided in order to maintain a high success rate upon release of the anchor designs (Figure 7.7b). It is known that silicon nitride membranes with thicknesses of 100-200 nm are very vulnerable to stress caused by fabrication processing and handling [Ekkels et al., 2003], which was indeed the case here. As the eight-leg design (Figure 7.6d) proved to be the most stable one during processing, it was the obvious choice for the flexible part of the tuneable MEMS filter.

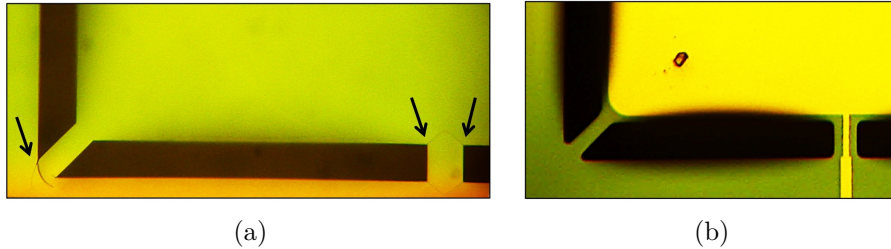


Figure 7.7: (a) Released membrane suspension exhibiting cracks at the corners of the design, highlighted by the black arrows. (b) Improved design with rounded corners featuring no cracks. In both images the length of the etched area was approximately 200 μm .

7.2.2 Process flow for a tuneable MEMS FP filter

The first step in the fabrication of the tuneable MEMS filter was the gold mirror deposition. The membrane sample was glued to a cover slip with a drop of PMMA resist and soft-baked for two minutes, then placed in the evaporation chamber. A 5 nm thin layer of chromium was first deposited to act as an adhesion layer [Aouani et al., 2009], followed by the 30 nm of gold mirror. For actuation, wires to both reflectors allowed me to apply a voltage, thereby actuating the membrane. The complete process flow of the fabrication of the hybrid metal-grating-based MEMS filter is illustrated in Figure 7.8 involving multiple lithographic exposures and careful alignment to each other. After sample cleaning (step 1), the first fabrication step was the deposition of gold via a lithographically defined pattern (steps 2+3+4), electron-beam evaporation (step 5), and a lift-off process on both cavity reflectors (step 6). Gold was evaporated in the central area of the membrane, on the actuating arms, and connected to larger pads located at the edge of the sample, which could later be accessed and contacted by wires. The gold surrounding the central grating mirror on the glass substrate with paths towards the edge of the sample provided the electrical counterpart of the capacitive system. In both cases, the metal was coated in a lift-off process using the electron-sensitive resist PMMA 950K to define the exact position on each chip (Figure 7.9a) coupled with alignment markers to which the

following lithographic steps relate to. During the first e-beam exposure, the corners of the membrane acted as first alignment points. Sometimes, the membrane was stressed following deposition of the resist, which resulted in an uncontrolled bowing making it impossible to expose a defined pattern (Figure 7.9b); in that case, the spin-coating step had to be repeated or a new membrane sample had to be used.

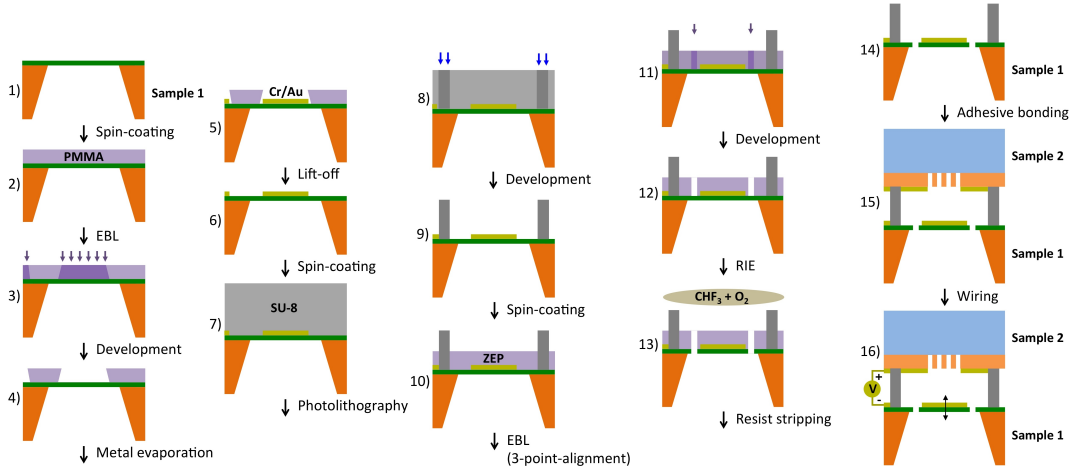


Figure 7.8: Workflow for fabrication of a tuneable MEMS FP filter based on a-Si high contrast gratings and metal reflector on a silicon nitride membrane (not to scale).

A common thickness ratio of resist-to-gold of 3:1 established a successful lift-off process (Figure 7.9c), although some agitation was usually necessary to remove the gold from all undesired areas. The lift-off process and related agitation was challenging for the fragile membrane, which broke relatively often or led to surface contamination. Due to the constant size of the membrane chips compared to the cleaved a-Si/glass samples and as a way to protect the fragile central area, the SU-8 spacer was lithographically applied (steps 7+8+9) in a symmetrical manner on the membrane sample by using an optical mask defining either two opposing polymer bars or a polymer frame. In a next iteration, the electron-sensitive resist ZEP 520A was spin-coated onto the membrane sample (step 10) and the suspension design was patterned via electron-beam lithography and matched to the previously defined alignment markers (step 11) (Figure 7.9d). After development in Xylene (step 12), the pattern was transferred to the central membrane area by reactive-ion etching using a 4:1 mixture of CHF_3 and O_2 (step 13) (Figure 7.9e). If any cracks had developed until the dry etching step, the membrane did usually not survive upon release. But even without any emerging fractures, the survival rate of the etched structures was very low due to I) mechanical shocks while removing the sample from the etching machine, II) rapid agitation in the resist stripping solution (such as beaker

shaking or too high temperatures), and III) non-vertical removal of the sample from the stripping solution (step 14).

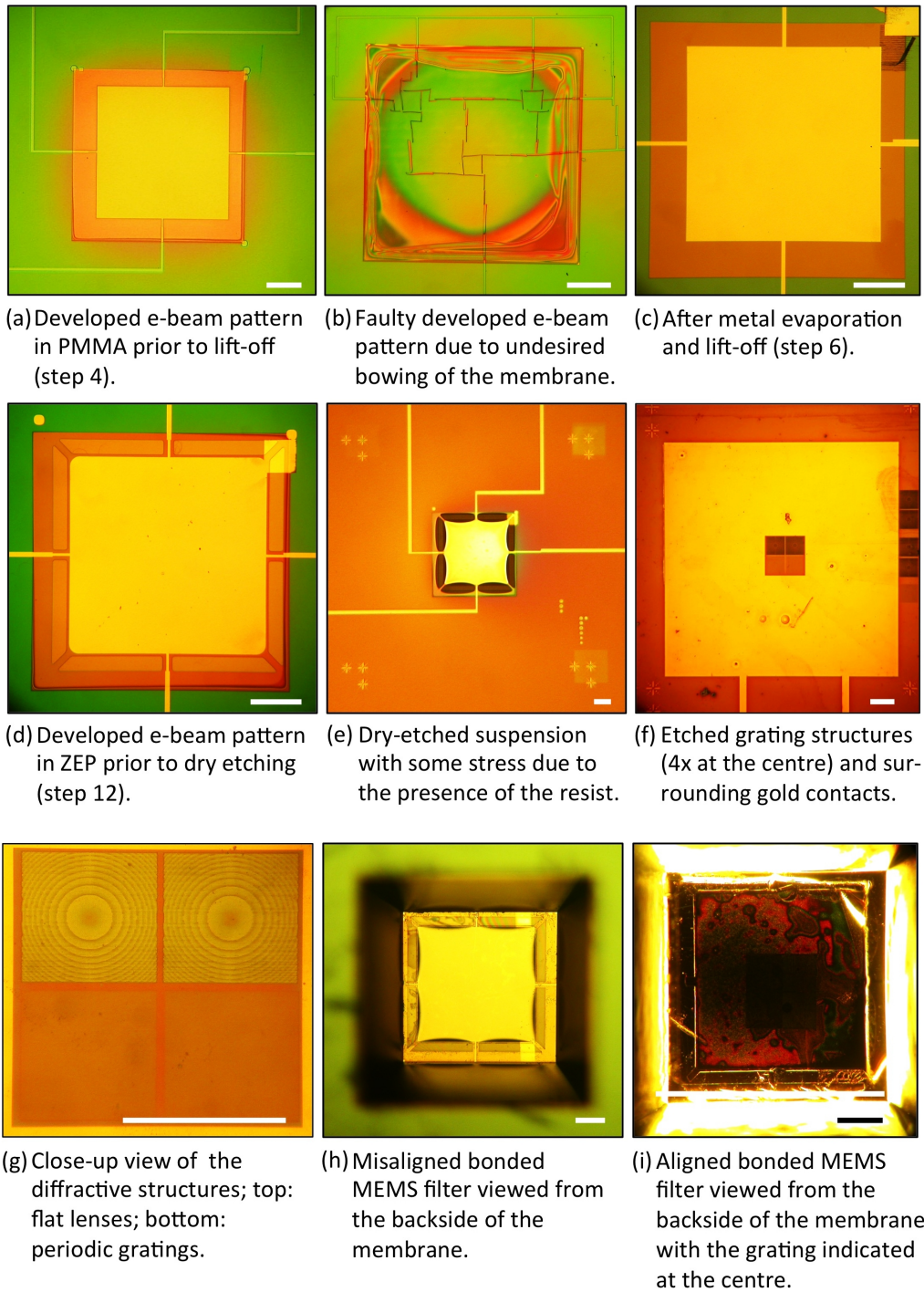


Figure 7.9: Optical micrographs during fabrication of the tuneable hybrid metal-grating-based MEMS filter. The scale bar in each image is 100 μm long.

Indeed, during these final processing steps, many membrane samples broke. Another critical step was the adhesive bonding between the metallised, released membrane sample and the rigid grating chip (step 15), because the optical cavity areas of around $400 \times 400 \mu\text{m}^2$ had to be precisely aligned to each other. After unsatisfactory trials of matching two test samples manually (Figure 7.9h), the initial bonding step was carried out under the microscope of the optical mask aligner with the rigid sample located at the bottom and holding the membrane sample from the top by the vacuum (using an intermediate microscope slide). The bottom sample could be located and aligned by looking through the released parts of the membrane. Note that the edged bonding pads of both samples had to be located on opposite sides to avoid short-circuiting during the wiring. Having identified the optimal bonding position, the samples were shortly separated to apply some liquid SU-8 2000.5 onto the spacer surface and then gently pressed together for 1 min before putting the compound chip on the hotplate for bonding. In the final stage (step 16) (Figure 7.9i), the compound sample was glued onto a printed circuit board and wired up for the application of a bias voltage (see final result in Figure 7.10a). Given all the difficulties I encountered in developing the process, which severely limited the repeatability, I was very pleased to achieve some working devices in the end. Overall, I estimate the fabrication yield to be only around 10% (>7 broken membranes per one working device), which I would hope to improve with more practise and further refinements.

7.3 Characterisation of tuneable MEMS FP filters

After optimisation of the fabrication process, I did obtain an intact tuneable metal-based MEMS Fabry-Pérot filter device. The silicon nitride membrane in this chip was uniform and not dry etched. I also successfully fabricated a hybrid metal-grating MEMS device with an etched eight-leg anchor pattern; however, due to the highly challenging fabrication, tuning was not feasible, so that only the static results are shown in this section. For characterisation, the same setup as shown in Figure 6.5 of Chapter 6 was used. For electrostatic actuation, the sample could easily be connected to a voltage source. Again, all experimental curves were smoothed by a running mean of ten adjacent wavelengths in order to filter out the noise.

7.3.1 Metal-based MEMS FP filter

Both mirrors were deposited with 5 nm of chromium and 30 nm of gold spaced about $8.26 \mu\text{m}$ apart from each other using two parallel arranged SU-8 bars fabricated using photolithography on one of the samples. Upon successful bonding of the metallised membrane and glass sample, the chip was fixed to a printed circuit board and wired up for easier handling. The final assembly is shown in Figure 7.10a (schematic shown in Figure 7.2). The characterisation of the tuneable metal-based Fabry-Pérot filter is shown in Figures 7.10b-d for a TM-polarised incident beam.

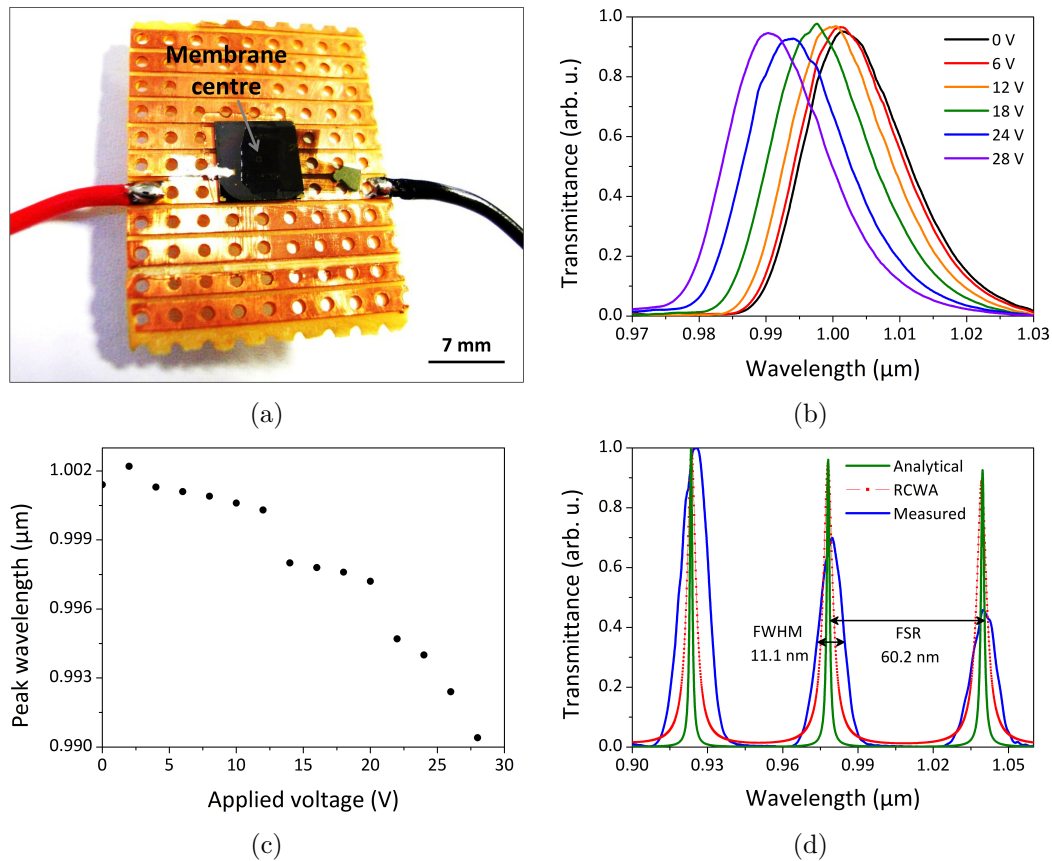


Figure 7.10: (a) Final assembly of a fabricated metal-based tuneable MEMS FP filter. (b) Electrostatic tuning of the transmission peak of the filter shown in (a) for voltages ranging from 0 to 28 V. (c) Dependence of the peak wavelength on the applied voltage. (d) FP transmission peaks for a metal-based MEMS filter different than that shown in (b) at 0 V bias; the resonance peaks are slightly shifted compared to the one shown in (b).

Without applying a voltage bias, I obtained an *FWHM* of the transmission peak around $0.98 \mu\text{m}$ of approximately 11.1 nm, an *FSR* of 60.2 nm (Figure 7.10d),

and hence an F_{eff} of about 5.4. In contrast, the theoretical values, obtained by FP theory, were 61 nm, 1.4 nm, and 43.6, respectively, while RCWA resulted in 61 nm, 4.4 nm, and 13.9, respectively. Upon driving the filter from 0 to 28 V, the wavelength shift was approximately 12 nm (Figure 7.10b). Given the fabricated cavity spacing of around 8 μm , a spring constant of the silicon nitride membrane of approximately 50 N/m [Cole et al., 2005], and an overlap area of the conducting plates of $500 \times 500 \mu\text{m}^2$, the pull-in voltage is estimated to be approximately 60 V according to Equation 7.1. Due to the lack of a suitable power supply at this stage, the filter could not be biased at voltages higher than 28 V. The $FWHM$ of the tuned Airy peaks is well maintained throughout the tuning range. From the aforementioned explanations about the effective finesse (Section 6.3.1 of Chapter 6), we note that the real finesse not only contains the reflectances of the mirrors, but also contributions from mirror irregularities, deviations from parallelism, and beam alignment issues. The reasons for the peak broadening are manifold: Firstly, a static analysis, performed by our collaborators at Tyndall National Institute, revealed a slight tension of the membrane after processing; the membrane exhibited a non-uniformity (Figure 7.11a) and bent downwards by around 75 nm across the central area of the membrane (Figure 7.11b).

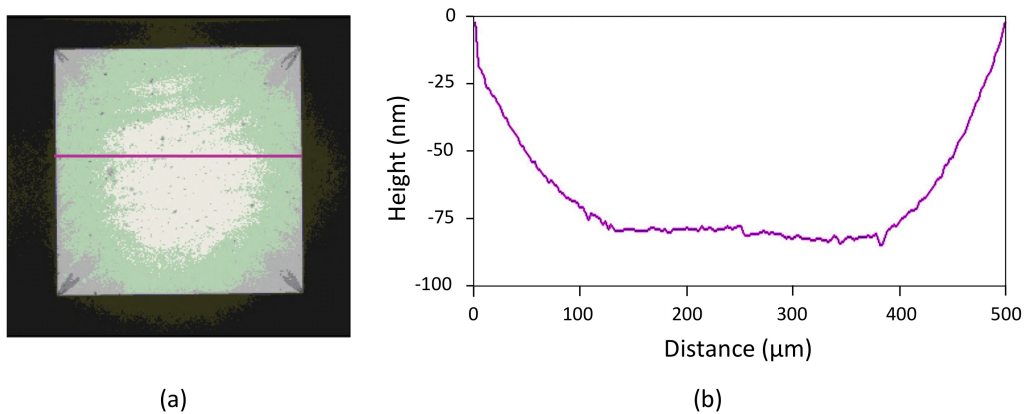


Figure 7.11: (a) Optical image of the gold-coated silicon nitride membrane. (b) Static analysis of the flatness of the processed membrane; the central area bends downwards by approximately 75 nm. Images adapted from measurements taken by Tyndall National Institute (Dr Zbigniew Olszewski).

Secondly, the surface roughness of the deposited gold reflector was increased by defects and voids after evaporation (as verified by SEM and optical images) and by the multiple fabrication steps, indicating that the optical quality of the mirror had deteriorated after final processing. In principle, assuming 95% reflectivity of the gold mirrors, the finesse of metal-based MEMS filters can reach up to 61 [Moon and Shkel, 2001]. In comparison, other work [Correia et al., 1999] has demonstrated a

tunable FP filter based on silver-coated silicon nitride membranes for the visible range with a finesse of approximately 30 and a peak width smaller than 3 nm with a voltage <20 V. Another MEMS device operating in the visible using two bonded quartz substrates, which were each coated with silver and indium tin oxide, achieved a finesse of 8.8 with a tuning range of approximately 50 nm for a voltage of 60 V [Gupta et al., 2012]. Furthermore, the performance of an angle-tuned solid etalon based on gold-coated polysilicon showed a finesse of 4.1 in the near-infrared range [Lin et al., 1996], which is comparable to our results. To obtain an idea of the tuning speed, our collaborators at Tyndall National Institute performed a dynamic analysis of the FP filter and attained the resonance frequencies of 712 Hz, 1.4 kHz, and 2.1 kHz corresponding to the 1st, 2nd, and 3rd mode, respectively (Figure 7.12). The resonant out-of-plane mode at 712 Hz corresponds to the mode, which is relevant for applying a bias voltage across the membrane and the counter electrode, so it represents the speed with which the filter can be driven.

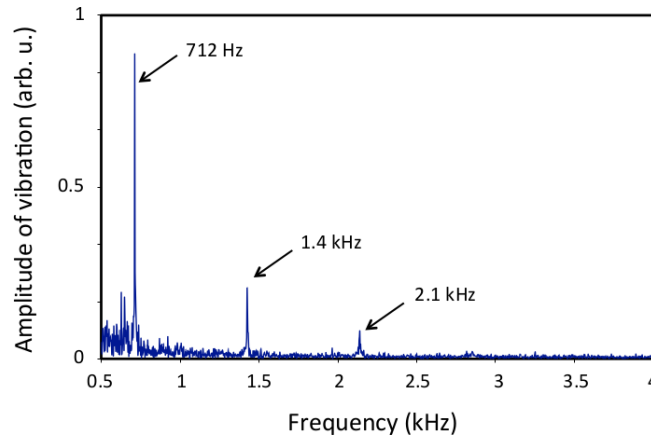


Figure 7.12: Dynamic analysis of the FP filter containing the gold-coated silicon nitride membrane performed by Tyndall National Institute (Dr Zbigniew Olszewski). Three modes of the resonance frequency are indicated in the figure.

7.3.2 Hybrid metal-grating-based MEMS FP filter

The fabricated device as shown schematically in Figure 7.2b showed the following response in transmission (Figure 7.13). The cavity spacing was increased to approximately 24 μm due to the different cleanroom conditions at the University of York compared to the one at the University of St Andrews, where the metal-based MEMS filter had been built. Hence the measured FSR , $FWHM$, and F_{eff} were 23 nm, 8.3 nm, 2.77 in contrast to the theoretical values of 23 nm, 1.5 nm, and 15.3,

respectively. The interference order was 75. As was observed in optical micrographs (such as Figure 7.9i), the gold-coated membrane was not very uniform after all processing routines and the release of the suspension arms. A continuous wavelength tuning could not be performed due to undesired short-circuits preventing the device from being actuated electrostatically. Many such devices have been built and were not functioning at the final stage due to multiple reasons: challenging fabrication with high risk of contamination during multiple lithographic steps; fragile membrane samples, which were prone to break during the process; apparent contamination of the cavity after the bonding step (Figure 7.9i).

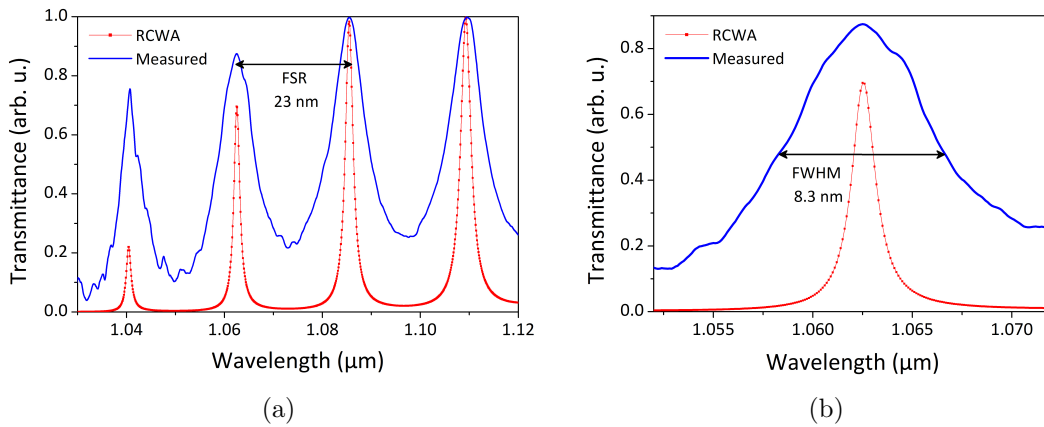


Figure 7.13: (a) Measured (solid blue) and calculated (red line) transmittances of a MEMS filter incorporating a gold-coated silicon nitride membrane and a periodic HCG on a glass substrate optimised for broadband reflection around 1 μm . (b) Close-up view of the resonance peak around 1.063 μm .

For comparison, while it is exciting to see the successful operation of working FP cavities, I note that previous work using a hybrid device incorporating high contrast gratings and Bragg stacks [Liu et al., 2014] has shown near-IR tuning with a peak width at least one order of magnitude narrower than the width I was able to achieve. Researchers have also demonstrated FP cavities, incorporated into VCSELs, with both reflectors containing 1D [Sciancalepore et al., 2012] or 2D silicon photonic crystal structures [Yang et al., 2012a] that achieved reflectivities close to 100%. Therefore, I believe that following a comprehensive optimisation of the processing and handling procedures, high contrast grating-based filters may complement the current state-of-the-art of tuneable MEMS FP filters for near-IR imaging or sensing applications. But so far, HCG reflectivities in excess of 99.99% have not been observed in practical devices [Liu et al., 2014], hence it will remain a challenge to outperform MEMS filters based on Bragg mirrors. In parallel, my colleague Dr Yue Wang successfully investigated a tuneable MEMS FP filter based on silicon nitride gratings

for operation in the visible spectral range [Wang et al., 2014], thereby targeting spectroscopic applications using organic light emitters. The silicon nitride grating was 500 nm thick with a period of 560 nm and a duty cycle of 0.5 and was bonded together with a silver-coated glass substrate. The obtained performance was an FSR of about 18 nm and an $FWHM$ of 5 nm resulting in a practical finesse of 3. A spiral-shaped release pattern proved to be superior in terms of uniform deflection compared to designs using straight or folded membrane legs (see Section 7.1.2). In turn, the applied voltage could be substantially decreased by a factor of three (9 V), while showing a similar wavelength shift (13 nm) around a wavelength of 630 nm like the metal-based FP filter around 980 nm presented in Section 7.3.1 (28 V for 12 nm shift).

7.4 Summary

To conclude, the following criteria have been discussed:

- Highly reflective mirrors ($R > 90\%$) based on thin film of gold and/or a-Si high contrast gratings
- Transmissive FP filter type requiring transparent substrates in the near-IR range
- Uniform displacement during electrostatic actuation

The electrostatic actuation of the metal-based MEMS FP filter was demonstrated successfully (Figure 7.10), whereas for the grating-based tuneable filters actuation was hindered by short-circuits resulting from the challenging fabrication. The measured characteristics of the fabricated MEMS FP filters are summarised in Table 7.1. Optically, the MEMS filters featured relatively sharp and symmetric transmission peaks. The discrepancy between the simulated and experimental data, i.e., the broadening of the Airy peaks compared to the simulation, is mostly attributed to the diverging incident beam, which could not be resolved in the transmission setup used. The challenging goal of demonstrating an improved filter design using silicon high contrast gratings for the application of swept-source optical coherence tomography (OCT) was not attained within the timeline of this thesis, mainly due to the low yield and difficulties encountered during the fabrication process. At this stage, the metal-based MEMS filter offers more advantages than its grating-based counterpart

due to the straightforward deposition of gold on both cavity sides while offering high reflectivity, good uniformity of the membrane, and ease of alignment during bonding. Therefore, we cannot recommend following up the route in going to the higher complexity of metal-grating or grating-grating filters unless critical issues like the proper a-Si deposition, membrane fragility, and flawless bonding of both mirrors are resolved.

Table 7.1: Summary of the results of the tuneable MEMS filters attained in this project. The values in curly brackets denote the computed values using RCWA.

Parameter	Metal-based	Grating-based	Grating-based
	FP filter	FP filter (a-Si)	FP filter (500 nm SiN _x)
$FWHM$ (nm)	11.1 {4.7}	8.3 {1.5}	5
FSR (nm)	60.2 {61.1}	23 {23}	18
F_{eff}	5.4 {13.1}	2.77 {15.3}	3
λ_c (μm)	0.98	1.063	0.63
m	17	75	75
Tuning range (nm)	12	-	13
V_{max} (V)	28	-	9

8 Conclusions and application perspectives

8.1 Overview of results

The main body of the work was the investigation of wavelength-scale high contrast gratings (HCGs) in amorphous silicon (a-Si). The unique properties of these microstructures were utilised to demonstrate broadband mirrors, flat reflective lenses with a high numerical aperture, and static and tuneable Fabry-Pérot (FP) filters, all operating in the near-infrared spectral range around 1 μm wavelength (Figure 8.1). I addressed a number of challenges to achieve these results:

- The characterisation of the amorphous silicon material obtained by collaborators by demonstrating that reflective mirrors could be realised in this material at a wavelength of around 1 μm .
- The realisation of a high numerical aperture of a microstructured grating lens by incorporating multiple phase jumps into the design.
- Regarding fabrication, the handling of thin flexible silicon nitride membranes and their practical implementation into a functional tuneable MEMS device.

In all related design processes, rigorous coupled-wave analysis (RCWA) was used because of its suitability for grating structures with feature sizes on the wavelength scale and its relatively simple implementation and fast convergence.

In Chapter 4, I showed the design, fabrication, and characterisation of grating mirrors in amorphous silicon with the aim to evaluate the practically achievable reflectivity and spectral bandwidth. Given the amorphous silicon material at hand, which was deposited either by sputtering, electron-beam evaporation, or plasma-enhanced chemical vapour deposition (PECVD), we found that the most

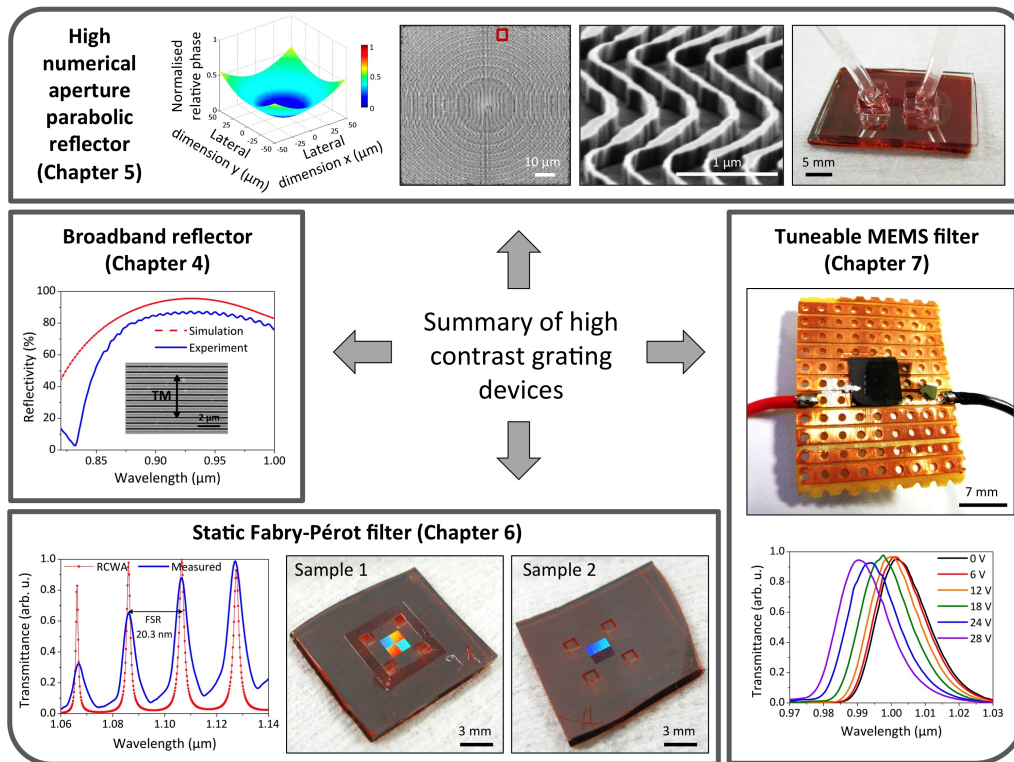


Figure 8.1: Summary of the results with reference to the corresponding thesis chapters.

reliable results were obtained with PECVD a-Si material deposited on a glass substrate; the best results were moderately high reflectivities of 85% across a bandwidth of 80 nm for TM polarisation centred around a wavelength of 950 nm. Due to an unusual absorption existing in the material in that range, however, which most probably originated from contamination and fluctuations during the deposition process, the theoretical reflectivity in the grating-on-glass sample was limited to 95%. The main reason for the difference between the simulated and measured values was the deviation in grating thickness between the 330 nm considered in the RCWA, and the thickness of 315 nm available experimentally, reaching at best a reflectivity of approximately 85%. We also considered the deposition of a-Si on a thin membrane by sputtering for use as a cavity grating mirror in a tuneable MEMS filter. Although we managed to demonstrate an experimental reflectivity above 97% across 170 nm around 1 μm wavelength for a sputtered a-Si device, we were not able to reproduce this result. Therefore, other deposition methods such as e-beam evaporation and PECVD were also investigated, but these caused unacceptable stress and buckling of the membrane as was shown in Chapter 3. For these reasons, we stopped investigating grating systems on a membrane further. We conclude that, while our material suffered from a significant contamination, for future developments, amorphous silicon remains

a highly suitable material for mirror applications around $1\ \mu\text{m}$ and could be used to push device performance close to reflectivities of 100% across bandwidths in excess of 100 nm.

In collaboration with my colleague Daan Stellinga, I designed, fabricated, and characterised a new type of flat diffractive and reflective lens with a high numerical aperture (NA) using two-dimensional high contrast gratings as presented in Chapter 5. The key challenges we overcame were the implementation of multiple phase jumps in the lens to enhance the numerical aperture while keeping the efficiency as high as possible. On the whole, we designed and fabricated cylindrical, spherical, and parabolic mirrors, with the latter showing the best optical performance. The most important result obtained was a new type of parabolic mirror with experimental NA of 0.37 and an estimated diffraction efficiency of approximately 80% at a wavelength of 980 nm, which was verified by finite element simulations. In accordance with other research [Fattal et al., 2010], we found out that the path-finding algorithm results in a conflict between reflectivity and phase, i.e., for a full 2π phase path one cannot maintain a reflectivity near unity, which presents the major trade-off for the design of such high- NA diffractive lenses: achieving a full 2π phase path *and* 100% reflectivity throughout is not possible, at least not in our geometry. Another conclusion we drew was that the grating thickness forces a compromise between fabrication viability, design tolerance, and the number of modes present within the grating structure. The thicker the grating, the more modes exist, but the sharper the transition between modes, which is more difficult to control. We chose a silicon thickness of approximately 300 nm, which only supports two modes and makes the design relatively simple and robust. Using this thickness, we were able to show high performing parabolic mirrors with high fabrication tolerances and quality.

Application-wise, we have reported the first results with flat lenses for large-area optical tweezing, which represents an important step towards higher levels of miniaturisation in lab-on-chip systems without the necessity for bulky or curved beam-shaping elements. To this end, we fabricated $1\times 1\ \text{mm}^2$ microlens arrays with an NA above 0.7, which were immersed in water and integrated with a microfluidic channel. We obtained initial results with a few functional traps, yet the experiment was limited by the fact that microparticles occasionally adhered to the silicon surface during the flow process. In future experiments, an adequate treatment by functionalising the silicon surface should help against the adherence of particles on the lens. Another application we considered was imaging, e.g., for using an array of lenses in a “fly’s eye” configuration. We realised that the lenses, due to their intrinsic

mode of operation, are limited to on-axis beams and therefore do not offer an angular acceptance angle that would make them suitable for imaging applications.

In Chapter 6, the feasibility of incorporating high contrast gratings in a Fabry-Pérot interferometer was introduced and tested as an intermediate stage on the way to making tuneable filters. Such grating-based FP cavities may improve the finesse of existing cavities. Their performance was compared to FP cavities based on metal mirrors as a simple reference. One of the main results was the development of a fabrication process utilising adhesive bonding to realise a FP filter. Moreover, we found that metal-based FP filters with a uniform polymer spacer within the cavity offered the best optical performance with an effective finesse close to 20. In contrast, the finesse of a metal-based FP filter with an air-filled cavity was only 2.3, which was probably caused by up to 10% height deviations of the spacer bars applied on one of the cavity mirrors prior to the bonding. Furthermore, measurements with FP filters based on a-Si gratings showed no further improvement; instead, only moderate finesse values of 5.5 were attained. One of the reasons for this large difference in performance between metal-based filters with polymer-filled cavity and grating-based filters with air-filled cavity was the larger and wider reflectivity of gold (>95%) across the spectral range considered. In addition, the higher uniformity in the even spacing layer provided a good parallelism between the two gold mirrors. In all experiments, the finesse was considerably limited by the angular spread of the incident beam in the optical setup, which could not be resolved due to the high noise floor in case of a collimated beam. Further improvements in the setup are indicated here. Overall, these first attempts demonstrated that the practical implementation of grating-based FP filters is not as straightforward and it remains questionable if they can outperform conventional Bragg mirrors, in particular in terms of optical bandwidth.

Chapter 7 explores an electrostatically tuneable MEMS filter based on HCGs at near-infrared wavelengths around 1 μm . Although the design concept of a fully grating-based MEMS filter appears to be relatively straightforward, its practical implementation proved much more difficult than expected; I was able to demonstrate a fully functional wavelength-tuneable MEMS filter based on metal mirrors with an effective finesse of 13, a tuning speed of 712 Hz, and a tuning range of 12 nm for a bias voltage of 28 V, but found it difficult to repeat this result. The main obstacles were the fragility of the silicon nitride membrane upon release of a suspension pattern and its vulnerability to contamination and damage during the complex fabrication process. Another problem was the deposition of amorphous silicon on the silicon nitride membrane due to strain and buckling, as already discussed above, which

forced us to drop the idea of a fully grating-based MEMS filter. Ultimately, the best results were achieved with static Fabry-Pérot filters consisting of a flexible metal mirror on one side and a silicon grating on the other. While a fully functional grating-based MEMS filter remains a challenge, we believe that some improvements in the fabrication process could result in a higher success rate. Firstly, the fragility problem may be addressed by using thicker silicon nitride membranes, i.e., with a thickness $>200\text{-}300\text{ nm}$ [Ekkels et al., 2003]. Secondly, in comparison to the reactive ion etching method we applied for the release of the suspension pattern, it would be worth investigating an alternative method using critical point drying, which has been shown to improve device yields and reproducibility [Zhou et al., 2008]. Thirdly, one could ask Norcada Inc. to perform a customised and high-quality deposition of amorphous silicon on the membrane. This solution would incur additional cost (US\$ 2-3k), but it may well save a lot of effort. The overall conclusion, however, is that HCGs are interesting components for MEMS-based Fabry-Pérot tuneable filters, but we were not able to achieve the performance of linewidths of smaller than 1 nm over a bandwidth of more than 100 nm and high-speed tuning in the MHz range, as already demonstrated for Bragg-mirror based filters of this kind [Flanders et al., 2002, Irmer et al., 2003]. Given the difficulties summarised above, we also do not think that such performance will be easily achieved in the near future.

8.2 Application perspectives

There are a number of new applications for the silicon diffractive grating lenses that we believe are very promising for future exploration. These include the collimation of a beam with arbitrary phase profile and the inclusion of a curved mirror into a Fabry-Pérot cavity for optical loss management (Figure 8.2). With regard to the FP resonators shown so far, the theoretical treatment assumed perfectly collimated, parallel beams, and cavities with plane parallel mirrors (Chapters 6+7). In reality, beams are divergent, so we need to consider introducing a focussing element into the cavity and invoking the concept of resonator stability and mode matching. This is also the reason why many MEMS-based Fabry-Pérot devices employ concave mirrors [Debernardi et al., 2008, Kanbara et al., 2009] instead of plane mirrors. For optimal optical performance and for stable operation to be achieved, the reflector's radius of curvature has to be matched to the wave front propagating within the cavity. As was described in Chapter 5, non-periodic high contrast gratings can serve as a focussing element in such a resonator. A possible resonator configuration using periodic and

non-periodic gratings is shown in Figure 8.2a. An intrinsic problem on this path, however, might be the angular acceptance limitation of the grating lens.

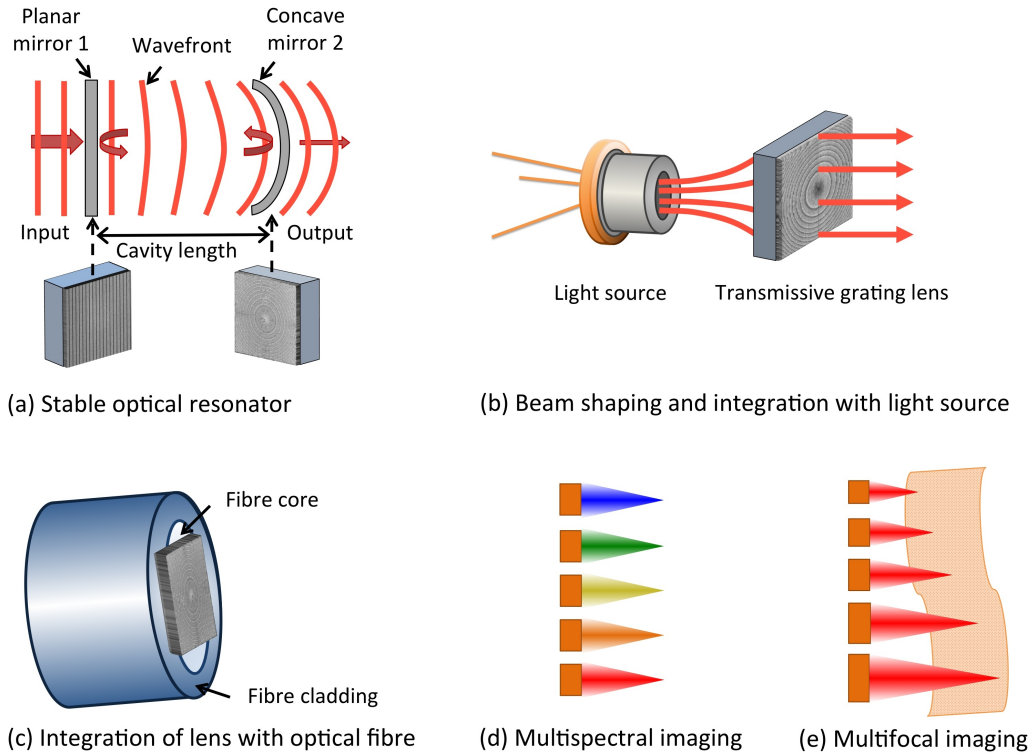


Figure 8.2: Possible applications for high contrast grating lenses. (a) Use in a stable optical resonator combining periodic and non-periodic HCGs. (b) Integration of a mode-shaping HCG lens with a light source for beam collimation. (c) Direct integration of the HCG lens with an optical fibre for collimation of the output beam. (d) Array of different HCG lenses designed for multispectral imaging. (e) Array of HCG lenses generating multiply focussed beams.

Many applications involve light sources with a micron-sized output facet and a correspondingly large divergence. Such sources require efficient coupling elements in order to establish a well-collimated output beam while keeping coupling losses to a minimum. A common approach is to use an optical fibre as a spatial filter, which implies that only the part of the output field that couples to the fundamental mode of the fibre is transmitted, and a lot of power is lost (typical coupling efficiencies are between 25% and 60% depending on the type of collimating lens). We propose a new approach based on the direct integration of a transmission-type grating lens with a semiconductor light source (Figure 8.2b) with the goal to achieve near-unity coupling efficiency between the optical fibre and the structured lens. Knowing the spectral properties of the light source, the design code for the grating lens can then

be customised to account for the intensity and for the exact phase profile. A suitably designed transmissive grating lens could be combined with the source to improve the performance in reducing the coupling loss into a fibre.

Alternatively, one could think of transferring a grating lens onto the tip of an optical fibre (Figure 8.2c), thereby enabling light to be controlled directly at the output facet of the fibre as has been shown, for instance, for functionalised fibre tips with photonic crystal cavities [Shambat et al., 2011] or with plasmonic structures [Ricciardi et al., 2013]. Furthermore, one could envisage arrays of such microlenses as multispectral imaging devices (Figure 8.2d). Another possibility is the generation of multiple beams at different focal lengths within a target (Figure 8.2e), which can be beneficial in clinical imaging of tissues using backscattered light.

List of abbreviations

1D	one dimensional
2D	two dimensional
3D	three dimensional
ASCII	American standard code for information exchange
ASE	amplified spontaneous emission
a-Si	amorphous silicon
BS	beam splitter
CAD	computer aided design
CCD	charged-coupled device
CMOS	complementary metal-oxide-semiconductor
c-Si	crystalline silicon
DC	direct current
DMD	digital micromirror device
DMF	dimethylformaldehyd
EBL	electron-beam lithography
FEM	finite element method
FM	flip mirror
FP	Fabry-Pérot
FPI	Fabry-Pérot interferometer
FSR	free spectral range
FWHM	full width at half maximum
FZP	Fresnel zone plate
GMR	guided-mode resonance
HCG	high contrast grating
IPA	isopropanol alcohol
IR	infrared
LED	light emitting diode
MEMS	microelectromechanical system
MOEMS	microoptoelectromechanical system

MTF	modulation transfer function
NA	numerical aperture
ND	neutral density
OCT	optical coherence tomography
OSA	optical spectrum analyser
PBS	polarisation beam splitter
PDMS	polydimethylsiloxane
PECVD	plasma-enhanced chemical vapour deposition
PhC	photonic crystal
PMMA	polymethylmethacrylat
PROPHET	Postgraduate Research On PHotonics as an Enabling Technology
PZT	lead zirconium titanate
RF	radio frequency
SEM	scanning electron microscope
TCE	trichlorethylen
TE	transverse electric
TM	transverse magnetic
TMA	thin-film micromirror array
USA	United States of America
UV	ultraviolet
VCSEL	vertical-cavity surface-emitting laser
WLS	white light source

Bibliography

- Aieta, F., Genevet, P., Kats, M. A., Yu, N., Blanchard, R., Gaburro, Z., and Capasso, F. (2012). Aberration-free ultrathin flat lenses and axicons at telecom wavelengths based on plasmonic metasurfaces. *Nano Letters*, 12(9):4932–4936.
- Almuneau, G., Condé, M., Gauthier-Lafaye, O., Bardinal, V., and Fontaine, C. (2011). High reflectivity monolithic sub-wavelength diffraction grating with GaAs/AlOx stack. *Journal of Optics*, 13(1):015505.
- Antoszewski, J., Dell, J., Shivakumar, T., Martyniuk, M., Winchester, K., Wehner, J., Musca, C., and Faraone, L. (2002). Towards MEMS based infrared tuneable micro-spectrometers. *Proceedings of SPIE*, 4935:148–155.
- Antoszewski, J., Nguyen, T., Martyniuk, M., Dell, J. M., and Faraone, L. (2011). Recent advances in SWIR MEMS-based tunable Fabry-Pérot microspectrometers. *Proceedings of SPIE*, 8012:80121X.
- Aouani, H., Wenger, J., Gérard, D., Rigneault, H., Devaux, E., Ebbesen, T. W., Mahdavi, F., Xu, T., and Blair, S. (2009). Crucial role of the adhesion layer on the plasmonic fluorescence. *ACS Nano*, 3(7):2043–2048.
- Apte, R. B., Sandejas, F. S. A., Banyai, W. C., and Bloom, D. M. (1993). Deformable grating light valves for high-resolution displays. *Society for Information Display International Symposium Digest of Technical Papers*, 24:807–808.
- Ashkin, A., Dziedzic, J. M., and Yamane, T. (1987). Optical trapping and manipulation of single cells using infrared laser beams. *Nature*, 330(6150):769–771.
- Ashok, P. C. (2012). *Integration methods for enhanced trapping and spectroscopy in optofluidics*. PhD thesis, University of St Andrews.
- Bakr, N. A., Funde, A. M., Waman, V. S., Kamble, M. M., Hawaldar, R. R., Amalnerkar, D. P., Gosavi, S. W., and Jadkar, S. R. (2011). Determination of the optical parameters of a-Si:H thin films deposited by hot wire-chemical vapour

- deposition technique using transmission spectrum only. *Pramana - Journal of Physics*, 76(3):519–531.
- Bass, M., Enoch, J. M., Van Stryland, E. W., and Wolfe, W. L. (2000). *Handbook of optics, Volume III*. McGraw-Hill.
- Bendickson, J. M., Glytsis, E. N., Gaylord, T. K., and Brundrett, D. L. (2001). Guided-mode resonant subwavelength gratings: effects of finite beams and finite gratings. *Journal of the Optical Society of America A*, 18(8):1912–1928.
- Benisty, H., De Neve, H., and Weisbuch, C. (1998). Impact of planar microcavity effects on light extraction-Part I: basic concepts and analytical trends. *IEEE Journal of Quantum Electronics*, 34(9):1612–1631.
- Beynon, T. D. and Strange, R. M. R. (2000). Computational study of diffraction patterns for near-field Fresnel and Gabor zone plates. *Journal of the Optical Society of America A*, 17(1):101–106.
- Bisaillon, E., Tan, D., Faraji, B., Kirk, A. G., Chrowstowski, L., and Plant, D. V. (2006). High reflectivity air-bridge subwavelength grating reflector and Fabry-Perot cavity in AlGaAs/GaAs. *Optics Express*, 14(7):2573–2582.
- Blomberg, M., Kattelus, H., and Miranto, A. (2009). Electrically tunable surface micromachined Fabry-Perot interferometer for visible light. *Procedia Chemistry*, 1(1):552–555.
- Bogaerts, W., Wiaux, V., Taillaert, D., Beckx, S., Luyssaert, B., Bienstman, P., and Baets, R. (2002). Fabrication of photonic crystals in silicon-on-insulator using 248-nm deep UV lithography. *IEEE Journal of Selected Topics in Quantum Electronics*, 8(4):928–934.
- Born, M. and Wolf, E. (1999). *Principles of optics*. Cambridge University Press, Cambridge, 7th edition.
- Boutami, S., Ben Bakir, B., Leclercq, J.-L., Letartre, X., Rojo-Romeo, P., Garrigues, M., Viktorovitch, P., Sagnes, I., Legratiet, L., and Strassner, M. (2006). Highly selective and compact tunable MOEMS photonic crystal Fabry-Perot filter. *Optics Express*, 14(8):3129–3137.
- Boye, R. R. and Kostuk, R. K. (2000). Investigation of the effect of finite grating size on the performance of guided-mode resonance filters. *Applied Optics*, 39(21):3649–3653.

- Breer, S. and Buse, K. (1998). Wavelength demultiplexing with volume phase holograms in photorefractive lithium niobate. *Applied Physics B*, 66:339–345.
- Brongersma, M. L., Cui, Y., and Fan, S. (2014). Light management for photovoltaics using high-index nanostructures. *Nature Materials*, 13(5):451–460.
- Brundrett, D. L., Glytsis, E. N., and Gaylord, T. K. (1998). Normal-incidence guided-mode resonant grating filters: design and experimental demonstration. *Optics Letters*, 23(9):700–702.
- Brundrett, D. L., Glytsis, E. N., Gaylord, T. K., and Bendickson, J. M. (2000). Effects of modulation strength in guided-mode resonant subwavelength gratings at normal incidence. *Journal of the Optical Society of America A*, 17(7):1221–1230.
- Chabbal, R. and Jacobi, R. B. (1958). Research on the best conditions for using a Fabry-Perot photo-electric spectrometer. *Atomic Energy Research Establishment*.
- Chang-Hasnain, C. J. (2000). Tunable VCSEL. *IEEE Journal of Selected Topics in Quantum Electronics*, 6(6):978–987.
- Chang-Hasnain, C. J. (2011). High-contrast gratings as a new platform for integrated optoelectronics. *Semiconductor Science and Technology*, 26(1):014043.
- Chang-Hasnain, C. J. and Yang, W. (2012). High-contrast gratings for integrated optoelectronics. *Advances in Optics and Photonics*, 4(3):379–440.
- Chen, J., Wang, W., Fang, J., and Varahramyan, K. (2004). Variable-focusing microlens with microfluidic chip. *Journal of Micromechanics and Microengineering*, 14(5):675–680.
- Chen, T., Cox, W. R., Lenhard, D., and Hayes, D. J. (2002). Microjet printing of high precision microlens array for packaging of fiber-optic components. *Proceedings of SPIE*, 4652:136–141.
- Chen, Y., Zhou, C., Luo, X., and Du, C. (2008). Structured lens formed by a 2D square hole array in a metallic film. *Optics Letters*, 33(7):753–755.
- Chou, S. Y. and Krauss, P. R. (1997). Imprint lithography with sub-10 nm feature size and high throughput. *Microelectronic Engineering*, 35:237–240.
- Chu, R.-S. and Kong, J. A. (1977). Modal theory of spatially periodic media. *IEEE Transactions on Microwave Theory and Techniques*, 25(1):18–24.

- Chung, I.-S., Iakovlev, V., Sirbu, A., Mereuta, A., Caliman, A., Kapon, E., and Mørk, J. (2010). Broadband MEMS-tunable high-index-contrast subwavelength grating long-wavelength VCSEL. *IEEE Journal of Quantum Electronics*, 46(9):1245–1253.
- Cižmár, T., Romero, L. C. D., Dholakia, K., and Andrews, D. L. (2010). Multiple optical trapping and binding: new routes to self-assembly. *Journal of Physics B*, 43(10):102001.
- Cole, G. D., Björlin, E. S., Chen, Q., Chan, C.-Y., Wu, S., Wang, C. S., MacDonald, N. C., and Bowers, J. E. (2005). MEMS-tunable vertical-cavity SOAs. *IEEE Journal of Quantum Electronics*, 41(3):390–407.
- Collin, R. E. (1960). *Field theory of guided waves*. McGraw-Hill, New York.
- Correia, J. H., Bartek, M., and Wolffenbuttel, R. F. (1999). Bulk-micromachined tunable Fabry-Perot microinterferometer for the visible spectral range. *Sensors and Actuators A*, 76(1):191–196.
- Dangel, R. and Lukosz, W. (1998). Electro-nanomechanically actuated integrated-optical interferometric intensity modulators and 2x2 space switches. *Optics Communications*, 156(1-3):63–76.
- Debernardi, P., Kogel, B., Zogal, K., Meissner, P., Maute, M., Ortsiefer, M., Bohm, G., and Amann, M. C. (2008). Modal properties of long-wavelength tunable MEMS-VCSELs with curved mirrors: comparison of experiment and modeling. *IEEE Journal of Quantum Electronics*, 44(4):391–399.
- Dijkstra, E. W. (1959). A note on two problems in connexion with graphs. *Numerische Mathematik*, 1(1):269–271.
- Ding, Y. and Magnusson, R. (2007). Band gaps and leaky-wave effects in resonant photonic-crystal waveguides. *Optics Express*, 15(2):680–694.
- Domash, L., Wu, M., Nemchuk, N., and Ma, E. (2004). Tunable and switchable multiple-cavity thin film filters. *Journal of Lightwave Technology*, 22(1):126–135.
- Duffy, D. C., McDonald, J. C., Schueller, O. J. A., and Whitesides, G. M. (1998). Rapid prototyping of microfluidic systems in poly(dimethylsiloxane). *Analytical Chemistry*, 70(23):4974–4984.
- Ebermann, M., Neumann, N., Hiller, K., Gittler, E., Meinig, M., and Kurth, S. (2010). Recent advances in expanding the spectral range of MEMS Fabry-Pérot filters. *Proceedings of SPIE*, 7594:75940V.

- Ekkels, P., Tjerkstra, R. W., Krijnen, G. J. M., Berenschot, J. W., Brugger, J., and Elwenspoek, M. C. (2003). Fabrication of functional structures on thin silicon nitride membranes. *Microelectronic Engineering*, 67-68:422–429.
- Fan, S. and Joannopoulos, J. D. (2002). Analysis of guided resonances in photonic crystal slabs. *Physical Review B*, 65(23):235112.
- Faraji, B., Bisailon, E., Tan, D. T. H., Plant, D., and Chrostowski, L. (2006). Finite-size resonant sub-wavelength grating high reflectivity mirror. *Lasers and Electro-Optics Society, IEEE*, pages 845–846.
- Farn, M. W. (1992). Binary gratings with increased efficiency. *Applied Optics*, 31(22):4453–4458.
- Fattal, D., Li, J., Peng, Z., Fiorentino, M., and Beausoleil, R. G. (2010). Flat dielectric grating reflectors with focusing abilities. *Nature Photonics*, 4(7):466–470.
- Filmetrics (2014). Refractive index database, <http://www.filmetrics.com>.
- Flanders, D. C., Whitney, P. S., and Miller, M. F. (2002). Flexible membrane for tunable Fabry-Perot filter. *US Patent 6,341,039 B1*.
- Flanders, D. C., Whitney, P. S., and Miller, M. F. (2003). Silicon on insulator optical membrane structure for Fabry-Perot MOEMS filter. *US Patent 6,608,711 B2*.
- Gale, M. T. (1997). Direct writing of continuous-relief micro-optics. In Herzig, H. P., editor, *Micro-Optics*, pages 87–126. Taylor & Francis, London.
- Gaylord, T. K. and Moharam, M. G. (1985). Analysis and applications of optical diffraction by gratings. *Proceedings of the IEEE*, 73(5):894–937.
- Genevet, P., Yu, N., Aieta, F., Lin, J., Kats, M. A., Blanchard, R., Scully, M. O., Gaburro, Z., and Capasso, F. (2012). Ultra-thin plasmonic optical vortex plate based on phase discontinuities. *Applied Physics Letters*, 100(1):013101.
- Givens, M. P. (1982). Focal shifts in diffracted converging spherical waves. *Optics Communications*, 41(3):145–148.
- Gupta, N., Tan, S., and Zander, D. R. (2012). Microelectromechanical systems-based visible-near infrared Fabry-Perot tunable filters using quartz substrate. *Optical Engineering*, 51(7):074007.
- Hale, G. M. and Query, M. R. (1973). Optical constants of water in the 200 nm to 200- μ m wavelength region. *Applied Optics*, 12(3):555–563.

- Harper, K. R. (2003). *Theory, design and fabrication of diffractive grating coupler for slab waveguide*. PhD thesis, Brigham Young University.
- Harris, J. H., Winn, R. K., and Dalgoutte, D. G. (1972). Theory and design of periodic couplers. *Applied Optics*, 11(10):2234–2241.
- Hays, D., Zribi, A., Chandrasekaran, S., Goravar, S., Maity, S., Douglas, L. R., Hsu, K., and Banerjee, A. (2010). A hybrid MEMS fiber optic tunable Fabry-Perot filter. *Journal of Microelectromechanical Systems*, 19(2):419–429.
- Hecht, E. (2002). *Optics*. Addison Wesley, San Francisco, 4th edition.
- Hernandez, S., Bouchard, O., Scheid, E., Daran, E., Jalabert, L., Arguel, P., Bonnefont, S., Gauthier-Lafaye, O., and Lozes-Dupuy, F. (2007). 850 nm wavelength range nanoscale resonant optical filter fabrication using standard microelectronics techniques. *Microelectronic Engineering*, 84(4):673–677.
- Hessel, A. and Oliner, A. A. (1965). A new theory of Wood’s anomalies on optical gratings. *Applied Optics*, 4(10):1275–1299.
- Hopkinson, F. and Rittenhouse, D. (1786). An optical problem proposed by Mr Hopkinson and solved by Mr Rittenhouse. *Transactions of the American Philosophical Society*, 2:201–206.
- Hung, E. S. and Senturia, S. D. (1999). Generating efficient dynamical models for microelectromechanical systems from a few finite-element simulation runs. *Journal of Microelectromechanical Systems*, 8(3):280–289.
- Ilic, A. and Goossen, K. W. (2004). Phase transition vs. thickness in stress-induced curvature on Cr/Au MEMS mirror layers. *Proceedings of SPIE*, 5342:19–25.
- Irmer, S., Daleiden, J., Rangelov, V., Prott, C., Römer, F., Strassner, M., Tarraf, A., and Hillmer, H. (2003). Ultralow biased widely continuously tunable Fabry-Pérot filter. *IEEE Photonics Technology Letters*, 15(3):434–436.
- Jacquinot, P. and Dufour, C. (1950). Utilisation des combinaisons de lames minces en interférométrie. *Journal de Physique et le Radium*, 11(7):427–431.
- Joannopoulos, J. D., Johnson, S. G., Winn, J. N., and Meade, R. D. (2008). *Photonic crystals*. Princeton University Press, Princeton and Oxford, 2nd edition.
- Johnson, P. B. and Christy, R. W. (1974). Optical constants of transition metals: Ti, V, Cr, Mn, Fe, Co, Ni, and Pd. *Physical Review B*, 9(12):5056.

- Johnson, S. G., Bienstman, P., Skorobogatiy, M. A., Ibanescu, M., Lidorikis, E., and Joannopoulos, J. D. (2002). Adiabatic theorem and continuous coupled-mode theory for efficient taper transitions in photonic crystals. *Physical Review E*, 66(6):066608.
- Kanamori, Y. and Hane, K. (2002). Broadband antireflection subwavelength gratings for polymethyl methacrylate fabricated with molding technique. *Optical Review*, 9(5):183–185.
- Kanamori, Y., Kitani, T., and Hane, K. (2007). Out-of-plane motion of 260-nm thick guided-mode resonant grating filter controlled by four micro-thermal actuators. *Microsystem Technologies*, 13(8-10):867–872.
- Kanbara, N., Noda, R., Yano, T., Saito, H., Fujimura, N., and Nishiyama, N. (2009). High speed micromechanically tunable surface emitting laser with Si-MEMS technology. *Yokogawa Technical Report English Edition*, 47:45–48.
- Karagodsky, V. and Chang-Hasnain, C. J. (2012). Physics of near-wavelength high contrast gratings. *Optics Express*, 20(10):10888–10895.
- Karagodsky, V., Pesala, B., Chase, C., Hofmann, W., Koyama, F., and Chang-Hasnain, C. J. (2010a). Monolithically integrated multi-wavelength VCSEL arrays using high-contrast gratings. *Optics Express*, 18(2):694–699.
- Karagodsky, V., Sedgwick, F. G., and Chang-Hasnain, C. J. (2010b). Theoretical analysis of subwavelength high contrast grating reflectors. *Optics Express*, 18(16):16973–16988.
- Katzir, A., Livanos, A. C., Shellan, J. B., and Yariv, A. (1977). Chirped gratings in integrated optics. *IEEE Journal of Quantum Electronics*, 13(4):296–304.
- Kikuta, H., Toyota, H., and Yu, W. (2003). Optical elements with subwavelength structured surfaces. *Optical Review*, 10(2):63–73.
- Kim, S., Barbastathis, G., and Tuller, H. L. (2004). MEMS for optical functionality. *Journal of Electroceramics*, 12(1/2):133–144.
- Kim, S.-G. and Hwang, K.-H. (2000). Thin-film micromirror array (TMA) for large information-display systems. *Journal of the Society of Information Display*, 8(2):177–181.
- Klemm, A. B., Stellinga, D., Martins, E. R., Lewis, L., Huyet, G., O’Faolain, L., and Krauss, T. F. (2013). Experimental high numerical aperture focusing with high contrast gratings. *Optics Letters*, 38(17):3410–3413.

- Klemm, A. B., Stellinga, D., Martins, E. R., Lewis, L., O’Faolain, L., and Krauss, T. F. (2014). Focusing with planar microlenses made of two-dimensionally varying high contrast gratings. *Optical Engineering*, 53(9):095104–1–095104–6.
- Kogelnik, H. (1975). Theory of dielectric waveguides. In *Integrated optics*, chapter 2, pages 13–81. Springer, Berlin Heidelberg.
- Kronast, W., Mescheder, U., Müller, B., and Huster, R. (2014). Development of a focusing micromirror device with an in-plane stress relief structure in silicon-on-insulator technology. *Journal of Micro/Nanolithography, MEMS and MOEMS*, 13(1):011112.
- Kurth, S., Hiller, K., Neumann, N., Seifert, M., Ebermann, M., Zajadacz, J., and Gessner, T. (2010). Sub-wavelength structures for infrared filtering. *Proceedings of SPIE*, 7713:77131S.
- Kuznetsov, M., Atia, W., Johnson, B., and Flanders, D. (2010). Compact ultrafast reflective Fabry-Perot tunable lasers for OCT imaging applications. *Proceedings of SPIE*, 7554:75541F.
- Lackner, M., Schwarzott, M., Winter, F., Kögel, B., Jatta, S., Halbritter, H., and Meissner, P. (2006). CO and CO₂ spectroscopy using a 60 nm broadband tunable MEMS-VCSEL at $\sim 1.55 \mu\text{m}$. *Optics Letters*, 31(21):3170–3172.
- Lalanne, P. (1997). Improved formulation of the coupled-wave method for two-dimensional gratings. *Journal of the Optical Society of America A*, 14(7):1592–1598.
- Lalanne, P. (1999). Waveguiding in blazed-binary diffractive elements. *Journal of the Optical Society of America A*, 16(10):2517–2520.
- Lalanne, P. and Hugonin, J.-P. (1998). High-order effective-medium theory of subwavelength gratings in classical mounting: application to volume holograms. *Journal of the Optical Society of America A*, 15(7):1843–1851.
- Lalanne, P., Hugonin, J.-P., and Chavel, P. (2006). Optical properties of deep lamellar gratings: a coupled Bloch-mode insight. *Journal of Lightwave Technology*, 24(6):2442–2449.
- Lalanne, P. and Lemercier-Lalanne, D. (1996). On the effective medium theory of subwavelength periodic structures. *Journal of Modern Optics*, 43(10):2063–2085.

- Lalanne, P. and Lemercier-Lalanne, D. (1997). Depth dependence of the effective properties of subwavelength gratings. *Journal of the Optical Society of America A*, 14(2):450–458.
- Larson, M. C., Pezeshki, B., and Harris, J. S. (1995). Vertical coupled-cavity microinterferometer on GaAs with deformable-membrane top mirror. *IEEE Photonics Technology Letters*, 7(4):382–384.
- Lee, H.-K., Yoon, J.-B., Yoon, E., Ju, S.-B., Yong, Y.-J., Lee, W., and Kim, S.-G. (1999). A high fill-factor infrared bolometer using micromachined multilevel electrothermal structures. *IEEE Transactions on Electron Devices*, 46(7):1489–1491.
- Lee, J. Y., Hahn, J. W., and Lee, H.-W. (2002). Spatiospectral transmission of a plane-mirror Fabry-Perot interferometer with nonuniform finite-size diffraction beam illuminations. *Journal of the Optical Society of America A*, 19(5):973–984.
- Levy, U., Nezhad, M., Kim, H.-C., Tsai, C.-H., Pang, L., and Fainman, Y. (2005). Implementation of a graded-index medium by use of subwavelength structures with graded fill factor. *Journal of the Optical Society of America A*, 22(4):724–733.
- Li, L. (1993). A modal analysis of lamellar diffraction gratings in conical mountings. *Journal of Modern Optics*, 40(4):553–573.
- Li, L. and Haggans, C. W. (1993). Convergence of the coupled-wave method for metallic lamellar diffraction gratings. *Journal of the Optical Society of America A*, 10(6):1184–1189.
- Li, Y. and Platzner, H. (1983). An experimental investigation of diffraction patterns in low-Fresnel-number focusing systems. *Optica Acta*, 30(11):1621–1643.
- Lin, C. H., Jiang, L., Chai, Y. H., Xiao, H., Chen, S. J., and Tsai, H. L. (2009). Fabrication of microlens arrays in photosensitive glass by femtosecond laser direct writing. *Applied Physics A*, 97(4):751–757.
- Lin, L. Y., Shen, J. L., Lee, S. S., Wu, M. C., and Sergent, A. M. (1996). Tunable three-dimensional solid Fabry-Perot etalons fabricated by surface-micromachining. *IEEE Photonics Technology Letters*, 8(1):101–103.
- Lin, S. H., Chan, Y. C., Webb, D. P., and Lam, Y. W. (1999). Optical characterization of hydrogenated amorphous silicon thin films deposited at high rate. *Journal of Electronic Materials*, 28(12):1452–1456.

- Lipson, A. and Yeatman, E. M. (2007). A 1-D photonic band gap tunable optical filter in (110) silicon. *Journal of Microelectromechanical Systems*, 16(3):521–527.
- Liscidini, M., Gerace, D., Andreani, L. C., and Sipe, J. E. (2008). Scattering-matrix analysis of periodically patterned multilayers with asymmetric unit cells and birefringent media. *Physical Review B*, 77(3):035324.
- Liu, A., Hofmann, W., and Bimberg, D. (2014). Two dimensional analysis of finite size high-contrast gratings for applications in VCSELs. *Optics Express*, 22(10):11804–11811.
- Lu, F., Sedgwick, F. G., Karagodsky, V., Chase, C., and Chang-Hasnain, C. J. (2010). Planar high-numerical-aperture low-loss focusing reflectors and lenses using subwavelength high contrast gratings. *Optics Express*, 18(12):12606–12614.
- Madou, M. J. (2012). *Fundamentals of microfabrication and nanotechnology, Vol. 2*. CRC Press, 3rd edition.
- Magnusson, R. and Gaylord, T. K. (1977). Analysis of multiwave diffraction of thick gratings. *Journal of the Optical Society of America*, 67(9):1165–1170.
- Magnusson, R. and Shokooh-Saremi, M. (2008). Physical basis for wideband resonant reflectors. *Optics Express*, 16(5):3456–3462.
- Magnusson, R. and Wang, S. S. (1995). Transmission bandpass guided-mode resonance filters. *Applied Optics*, 34(35):8106–8109.
- Manfrinato, V. R., Zhang, L., Su, D., Duan, H., Hobbs, R. G., Stach, E. A., and Berggren, K. K. (2013). Resolution limits of electron-beam lithography toward the atomic scale. *Nano Letters*, 13(4):1555–1558.
- Masson, J., St-Gelais, R., Poulin, A., and Peter, Y.-A. (2010). Tunable fiber laser using a MEMS-based in plane Fabry-Pérot filter. *IEEE Journal of Quantum Electronics*, 46(9):1313–1319.
- Mateus, C. F. R., Chang, C.-H., Chrostowski, L., Yang, S., Sun, D., Pathak, R., and Chang-Hasnain, C. J. (2002). Widely tunable torsional optical filter. *IEEE Photonics Technology Letters*, 14(6):819–821.
- Mateus, C. F. R., Huang, M. C. Y., and Chang-Hasnain, C. J. (2005). Micromechanical tunable optical filters: general design rules for wavelengths from near-IR up to 10 μm . *Sensors And Actuators A*, 119(1):57–62.

- Mateus, C. F. R., Huang, M. C. Y., Deng, Y., Neureuther, A. R., and Chang-Hasnain, C. J. (2004). Ultrabroadband mirror using low-index cladded subwavelength grating. *IEEE Photonics Technology Letters*, 16(2):518–520.
- Matin, M. A., Yi, Y.-B., and Gogte, V. (2007). Modeling and analysis of a low-actuation-voltage MEM mirror with spring structure for tunable optical filter. *Journal of Micro/Nanolithography, MEMS and MOEMS*, 6(2):023011.
- Meinig, M., Kurth, S., Hiller, K., Neumann, N., Ebermann, M., Gittler, E., and Gessner, T. (2011). Tunable mid-infrared filter based on Fabry-Pérot interferometer with two movable reflectors. *Proceedings of SPIE*, 7930:79300K.
- Meltz, G., Morey, W. W., and Glenn, W. H. (1989). Formation of Bragg gratings in optical fibers by a transverse holographic method. *Optics Letters*, 14(15):823–825.
- Merenda, F., Rohner, J., Fournier, J.-M., and Salathé, R.-P. (2007). Miniaturized high-NA focusing-mirror multiple optical tweezers. *Optics Express*, 15(10):6075–6086.
- Mielke, S. L., Ryan, R. E., Hilgeman, T., Lesyna, L., Madonna, R. G., and Van Nostrand, W. C. (1997). Measurements of the phase shift on reflection for low-order infrared Fabry-Perot interferometer dielectric stack mirrors. *Applied Optics*, 36(31):8139–8144.
- Milne, J. S., Dell, J. M., Keating, A. J., and Faraone, L. (2009). Widely tunable MEMS-based Fabry-Perot filter. *Journal of Microelectromechanical Systems*, 18(4):905–913.
- Moharam, M. G. and Gaylord, T. K. (1981). Rigorous coupled-wave analysis of planar-grating diffraction. *Journal of the Optical Society of America*, 71(7):811–818.
- Moharam, M. G. and Gaylord, T. K. (1986). Rigorous coupled-wave analysis of metallic surface-relief gratings. *Journal of the Optical Society of America A*, 3(11):1780–1787.
- Moon, J. and Shkel, A. M. (2001). Performance limits of a micromachined tunable-cavity filter. In *Proceedings of the International Conference on Modeling and Simulation of Microsystems*, pages 278–281.
- Motamedi, M. E., Southwell, W. H., and Gunning, W. J. (1992). Antireflection surfaces in silicon using binary optics technology. *Applied Optics*, 31(22):4371–4376.

- Mroziewicz, B. (2008). External cavity wavelength tunable semiconductor lasers - a review. *Opto-Electronics Review*, 16(4):347–366.
- Müller, R., Cristea, D., Tibeica, C., Arguel, P., Pons, P., Rossel, F., Syvridis, D., and Kusko, M. (2005). Tunable Fabry-Perot surface micromachined interferometer-experiments and modeling. *Microsystem Technologies*, 12(1-2):91–97.
- Mutlu, M., Akosman, A. E., Kurt, G., Gokkavas, M., and Ozbay, E. (2012a). Experimental realization of a high-contrast grating based broadband quarter-wave plate. *Optics Express*, 20(25):27966–27973.
- Mutlu, M., Akosman, A. E., and Ozbay, E. (2012b). Broadband circular polarizer based on high-contrast gratings. *Optics Letters*, 37(11):2094–2096.
- Niklaus, F., Stemme, G., Lu, J.-Q., and Gutmann, R. J. (2006). Adhesive wafer bonding - Focused review. *Journal of Applied Physics*, 99(3):031101.
- Norton, S. M., Erdogan, T., and Morris, G. M. (1997). Coupled-mode theory of resonant-grating filters. *Journal of the Optical Society of America A*, 14(3):629–639.
- Notomi, M. (2010). Manipulating light with strongly modulated photonic crystals. *Reports on Progress in Physics*, 73(9):096501.
- Osinski, M. and Buus, J. (1987). Linewidth broadening factor in semiconductor lasers - An overview. *IEEE Journal of Quantum Electronics*, 23(1):9–29.
- Ottevaere, H., Cox, R., Herzig, H. P., Miyashita, T., Naessens, K., Taghizadeh, M., Völkel, R., Woo, H. J., and Thienpont, H. (2006). Comparing glass and plastic refractive microlenses fabricated with different technologies. *Journal of Optics A*, 8(7):407–429.
- Peatross, J. and Ware, M. (2013). *Physics of light and optics*. Brigham Young University.
- Peng, S. and Morris, G. M. (1995). Efficient implementation of rigorous coupled-wave analysis for surface-relief gratings. *Journal of the Optical Society of America A*, 12(5):1087–1096.
- Peng, S. T., Tamir, T., and Bertoni, H. L. (1975). Theory of periodic dielectric waveguides. *IEEE Transactions on Microwave Theory and Techniques*, 23(1):123–133.

- Popovic, Z. D., Sprague, R. A., and Connell, G. A. N. (1988). Technique for monolithic fabrication of microlens arrays. *Applied Optics*, 27(7):1281–1284.
- Poutous, M. K., Pung, A. J., Srinivasan, P., Roth, Z. A., and Johnson, E. G. (2010). Polarization selective, graded-reflectivity resonance filter, using a space-varying guided-mode resonance structure. *Optics Express*, 18(26):27764–27776.
- Prahl, S. (2002). Optical absorption of hemoglobin, <http://omlc.ogi.edu/spectra/hemoglobin>.
- Qiaoqiang, G., Fu, Z., Ding, Y. J., and Bartoli, F. J. (2008). Ultrawide-bandwidth slow-light system based on THz plasmonic graded metallic grating structures. *Physical Review Letters*, 100(25):256803.
- Raguin, D. H. and Morris, G. M. (1993). Antireflection structured surfaces for the infrared spectral region. *Applied Optics*, 32(7):1154–1167.
- Rakuljic, G. A. and Leyva, V. (1993). Volume holographic narrow-band optical filter. *Optics Letters*, 18(6):459–461.
- Rayleigh, L. (1887). On the maintenance of vibrations by forces of double frequency, and on the propagation of waves through a medium endowed with a periodic structure. *The London, Edinburgh, and Dublin Philosophical Magazine and Journal of Science*, 24(147):145–159.
- Reader-Harris, P., Ricciardi, A., Krauss, T. F., and Di Falco, A. (2013). Optical guided mode resonance filter on a flexible substrate. *Optics Express*, 21(1):1002–1007.
- Ricciardi, A., Campopiano, S., Cusano, A., Krauss, T. F., and O’Faolain, L. (2010). Broadband mirrors in the near-infrared based on subwavelength gratings in SOI. *IEEE Photonics Journal*, 2(5):696–702.
- Ricciardi, A., Consales, M., Quero, G., Crescitelli, A., Esposito, E., and Cusano, A. (2013). Lab-on-fiber devices as an all around platform for sensing. *Optical Fiber Technology*, 19(6):772–784.
- Rosenblatt, D., Sharon, A., and Friesem, A. A. (1997). Resonant grating waveguide structures. *IEEE Journal of Quantum Electronics*, 33(11):2038–2059.
- Roychoudhuri, C. and Hercher, M. (1977). Stable multipass Fabry-Perot interferometer: design and analysis. *Applied Optics*, 16(9):2514–2520.

- Ruffieux, P., Scharf, T., Herzig, H. P., Völkel, R., and Weible, K. J. (2006). On the chromatic aberration of microlenses. *Optics Express*, 14(11):4687–4694.
- Sakai, K., Miyai, E., and Noda, S. (2007). Two-dimensional coupled wave theory for square-lattice photonic-crystal lasers with TM-polarization. *Optics Express*, 15(7):3981–3990.
- Sciancalepore, C., Bakir, B. B., Letartre, X., Harduin, J., Olivier, N., Seassal, C., Fedeli, J., and Viktorovitch, P. (2012). CMOS-compatible ultra-compact 1.55- μm emitting VCSELs using double photonic crystal mirrors. *IEEE Photonics Technology Letters*, 24(6):455–457.
- Scullion, M. G. (2013). *Slotted photonic crystal biosensors*. PhD thesis, University of St Andrews.
- Shambat, G., Provine, J., Rivoire, K., Sarmiento, T., Harris, J., and Vučković, J. (2011). Optical fiber tips functionalized with semiconductor photonic crystal cavities. *Applied Physics Letters*, 99(19):191102.
- Shao, H., Kumar, D., Feld, S. A., and Lear, K. L. (2005). Fabrication of a Fabry-Pérot cavity in a microfluidic channel using thermocompressive gold bonding of glass substrates. *Journal of Microelectromechanical Systems*, 14(4):756–762.
- Shokooh-Saremi, M. and Magnusson, R. (2008a). Design and analysis of resonant leaky-mode broadband reflectors. In *Progress In Electromagnetics Research Symposium*, pages 846–851.
- Shokooh-Saremi, M. and Magnusson, R. (2008b). Wideband leaky-mode resonance reflectors: influence of grating profile and sublayers. *Optics Express*, 16(22):18249–18263.
- Srinivasan, P., Poutous, M. K., Roth, Z. A., Yilmaz, Y. O., Rumpf, R. C., and Johnson, E. G. (2009). Spatial and spectral beam shaping with space-variant guided mode resonance filters. *Optics Express*, 17(22):20365–20375.
- Stone, H. A., Stroock, A. D., and Ajdari, A. (2004). Engineering flows in small devices: microfluidics toward a lab-on-a-chip. *Annual Review of Fluid Mechanics*, 36:381–411.
- Stork, W., Streibl, N., Haidner, H., and Kipfer, P. (1991). Artificial distributed-index media fabricated by zero-order gratings. *Optics Letters*, 16(24):1921–1923.

- Suhara, T., Taniguchi, T., Uemukai, M., Nishihara, H., Hirata, T., Iio, S., and Suehiro, M. (1995). Monolithic integrated-optic position/displacement sensor using waveguide gratings and QW-DFB laser. *IEEE Photonics Technology Letters*, 7(10):1195–1197.
- Sun, T., Wang, J., Ma, J., Jin, Y., He, H., Shao, J., and Fan, Z. (2009). Ultra-narrow bandwidth resonant reflection grating filters using the second diffracted orders. *Optics Communications*, 282(4):451–454.
- Tamir, T. (1975). Leaky waves in planar optical waveguides. *Nouvelle Revue d'Optique*, 6(5):273–284.
- Tayebati, P., Wang, P. D., Vakhshoori, D., Azimi, M., Kanskar, M., and Sacks, R. N. (1998). Widely tunable Fabry-Perot filters using high-index-contrast DBRs. *Proceedings of SPIE*, 3234:206–218.
- Temple-Boyer, P., Rossi, C., Saint-Etienne, E., and Scheid, E. (1998). Residual stress in low pressure chemical vapor deposition SiN_x films deposited from silane and ammonia. *Journal of Vacuum Science and Technology A*, 16(4):2003–2007.
- Tibuleac, S. and Magnusson, R. (1997). Reflection and transmission guided-mode resonance filters. *Journal of the Optical Society of America A*, 14(7):1617–1626.
- Tiedje, T., Yablonovitch, E., Cody, G. D., and Brooks, B. G. (1984). Limiting efficiency of silicon solar cells. *IEEE Transactions on Electron Devices*, 31(5):711–716.
- Tran, A. T. T. D., Lo, Y. H., Zhu, Z. H., Haronian, D., and Mozdy, E. (1996). Surface micromachined Fabry-Perot tunable filter. *IEEE Photonics Technology Letters*, 8(3):393–395.
- Ura, S., Shinohara, M., Suhara, T., and Nishihara, H. (1994). Integrated-optic grating-scale-displacement sensor using linearly focusing grating couplers. *IEEE Photonics Technology Letters*, 6(2):239–241.
- Van Kessel, P., Hornbeck, L. J., Meier, R. E., and Douglass, M. R. (1998). A MEMS-based projection display. *Proceedings of the IEEE*, 86(8):1687–1704.
- Van Zeijl, H. W. and Nanver, L. K. (2005). LPCVD silicon nitride-on-silicon spacer technology. In *Proceedings 20th International Symposium on Microelectronics Technology and Devices*, pages 153–162.
- Verslegers, L., Catrysse, P. B., Yu, Z., and Fan, S. (2009). Planar metallic nanoscale slit lenses for angle compensation. *Applied Physics Letters*, 95(7):071112.

- Vo, S., Fattal, D., Sorin, W. V., Peng, Z., Tran, T., Fiorentino, M., and Beausoleil, R. G. (2014). Sub-wavelength grating lenses with a twist. *IEEE Photonics Technology Letters*, 26(13):1375–1378.
- Vokinger, U., Dändliker, R., Blattner, P., and Herzig, H. P. (1998). Unconventional treatment of focal shift. *Optics Communications*, 157(1):218–224.
- Wang, S. S. and Magnusson, R. (1993). Theory and applications of guided-mode resonance filters. *Applied Optics*, 32(14):2606–2613.
- Wang, S. S. and Magnusson, R. (1995). Multilayer waveguide-grating filters. *Applied Optics*, 34(14):2414–2420.
- Wang, S. S., Magnusson, R., Bagby, J. S., and Moharam, M. G. (1990). Guided-mode resonances in planar dielectric-layer diffraction gratings. *Journal of the Optical Society of America A*, 7(8):1470–1474.
- Wang, W. J., Lin, R. M., Ren, Y., Sun, T. T., and Guo, D. G. (2003). Fabry-Perot microcavity pressure sensor with a novel single deeply corrugated diaphragm. *Microwave and Optical Technology Letters*, 39(3):240–243.
- Wang, Y., Stellinga, D., Klemm, A. B., Reardon, C. P., and Krauss, T. F. (2014). Tunable optical filters based on silicon nitride high contrast gratings. *Journal of Selected Topics in Quantum Electronics*, 21(4):2700706.
- Wilksch, P. A. (1985). Instrument function of the Fabry-Perot spectrometer. *Applied Optics*, 24(10):1502–1511.
- Wilson, S. J. and Hutley, M. C. (1982). The optical properties of "moth eye" antireflection surfaces. *Optica Acta*, 29(7):993–1009.
- Winchester, K. J. and Dell, J. M. (2001). Tunable Fabry-Pérot cavities fabricated from PECVD silicon nitride employing zinc sulphide as the sacrificial layer. *Journal of Micromechanics and Microengineering*, 11(5):589–594.
- Wolffenbuttel, R. F. (2004). State-of-the-art in integrated optical microspectrometers. *IEEE Transactions on Instrumentation and Measurement*, 53(1):197–202.
- Wood, R. W. (1902). On a remarkable case of uneven distribution of light in a diffraction grating spectrum. *Proceedings of the Physical Society of London*, 18(1):269–275.

- Wu, H., Mo, W., Hou, J., Gao, D., Hao, R., Guo, R., Wu, W., and Zhou, Z. (2009). Polarizing beam splitter based on a subwavelength asymmetric profile grating. *Journal of Optics*, 12(1):015703.
- Wu, H., Mo, W., Hou, J., Gao, D., Hao, R., Jiang, H., Guo, R., Wu, W., and Zhou, Z. (2010). A high performance polarization independent reflector based on a multilayered configuration grating structure. *Journal of Optics*, 12(4):045703.
- Wu, M. S., Vail, E. C., Li, G. S., Yuen, W., and Chang-Hasnain, C. J. (1995). Tunable micromachined vertical cavity surface emitting laser. *Electronics Letters*, 31(19):1671–1672.
- Xia, Y. and Whitesides, G. M. (1998). Soft lithography. *Angewandte Chemie International Edition*, 37(5):550–575.
- Xu, W., Chen, S., Bao, S., Zhou, Y., Zhao, S., Meng, Q., and Luo, H. (2011). 3-5 μm F-P tunable filter array based on MEMS technology. *Journal of Physics: Conference Series*, 276:012052.
- Yablonovitch, E. (1987). Inhibited spontaneous emission in solid-state physics and electronics. *Physical Review Letters*, 58(20):2059–2062.
- Yablonovitch, E. (1993). Photonic band-gap structures. *Journal of the Optical Society of America B*, 10(2):283–295.
- Yang, H., Zhao, D., Chuwongin, S., Seo, J.-H., Yang, W., Shuai, Y., Berggren, J., Hammar, M., Ma, Z., and Zhou, W. (2012a). Transfer-printed stacked nanomembrane lasers on silicon. *Nature Photonics*, 6(9):615–620.
- Yang, H., Zhao, D., Seo, J.-H., Chuwongin, S., Kim, S., Rogers, J. A., Ma, Z., and Zhou, W. (2012b). Broadband membrane reflectors on glass. *IEEE Photonics Technology Letters*, 24(6):476–478.
- Yariv, A. and Yeh, P. (2007). *Photonics: Optical electronics in modern communications*. Oxford University Press, New York, Oxford, 6th edition.
- Ye, J.-S., Kanamori, Y., Hu, F.-R., and Hane, K. (2006). Self-supported subwavelength gratings with a broad band of high reflectance analysed by the rigorous coupled-wave method. *Journal of Modern Optics*, 53(14):1995–2004.
- Yeh, P. (1988). *Optical waves in layered media*. Wiley, New York.
- Yu, K. and Park, N. (2005). Characterization of MEMS optical bandpass filters with narrow transition bands. *Proceedings of SPIE*, 6021:60212R.

- Yu, N. and Capasso, F. (2014). Flat optics with designer metasurfaces. *Nature Materials*, 13(2):139–150.
- Yu, N., Genevet, P., Kats, M. A., Aieta, F., Tetienne, J.-P., Capasso, F., and Gaburro, Z. (2011). Light propagation with phase discontinuities: generalized laws of reflection and refraction. *Science*, 334(6054):333–337.
- Zhou, Y., Huang, M. C., and Chang-Hasnain, C. J. (2008). Tunable VCSEL with ultra-thin high contrast grating for high-speed tuning. *Optics Express*, 16(18):14221–14226.
- Ziebart, V., Paul, O., and Baltes, H. (1999). Strongly buckled square micromachined membranes. *Journal of Microelectromechanical Systems*, 8(4):423–432.